Cascades of heterodimensional cycles via period doubling

Nelson Wong, Bernd Krauskopf and Hinke M. Osinga
Department of Mathematics, The University of Auckland,
Private Bag 92019, Auckland 1142, New Zealand

July 2024

Abstract

A heterodimensional cycle is formed by the intersection of stable and unstable manifolds of two saddle periodic orbits that have unstable manifolds of different dimensions: connecting orbits exist from one periodic orbit to the other, and vice versa. The difference in dimensions of the invariant manifolds can only be achieved in vector fields of dimension at least four. At least one of the connecting orbits of the heterodimensional cycle will necessarily be structurally unstable, meaning that is does not persist under small pertubations. Nevertheless, the theory states that the existence of a heterodimensional cycle is generally a "robust" phenomenon: any sufficiently close vector field (in the C^1-topology) also has a heterodimensional cycle.

We investigate a particular four-dimensional vector field that is known to have a heterodimensional cycle. We continue this cycle as a codimension-one invariant set in a two-parameter plane. Our investigations make extensive use of advanced numerical methods that prove to be an important tool for uncovering the dynamics and providing insight into the underlying geometric structure. We study changes in the family of connecting orbits as two parameters vary and Floquet multipliers of the periodic orbits in the heterodimensional cycle change. In particular the Floquet multipliers of one of the periodic orbits change from real positive to real negative and a period-doubling bifurcation occurs. We then focus on the transitions that occur near this period-doubling bifurcation and find that it generates new families of heterodimensional cycles with different geometric properties. Our careful numerical study suggests that further two-parameter continuation of the 'period-doubled heterodimensional cycles' gives rise to an abundant presence of heterodimensional cycles of different types in the limit of a period-doubling cascade.

Our results for this particular example vector field make a contribution to the emerging bifurcation theory of heterodimensional cycles. In particular, the bifurcation scenario we present can be viewed as a specific mechanism behind so-called stabilisation of a heterodimensional cycle via the embedding of one of its constituent periodic orbits into a more complex invariant set.

1 Introduction

From a pragmatic standpoint, mathematical models are 'well behaved' when small variations (for example, in system parameters) do not qualitatively alter the dynamics. This idea is formally captured by the notion of *structural stability*, which applies to both continuous-time and discrete-time systems, given by smooth vector fields and diffeomorphisms (smooth maps with smooth inverses), respectively. A system (vector field or diffeomorphism) is structurally stable if every system in a C^1-neighbourhood has topologically equivalent dynamics. Throughout this paper, we consider the C^1-topology for vector fields and diffeomorphisms, meaning that nearby systems must be close also in their first (partial) derivatives [20]. In the 1960s and 70s, various contributors led by Smale [28, 29, 30] determined equivalent properties for a system of any dimension to be structurally stable: a diffomorphism is structurally stable if, and only if

(1) its nonwandering set is hyperbolic and equal to the closure of the set of periodic orbits; and

(2) the unstable manifold of any nonwandering point transversely intersects the stable manifold of the same and any other nonwandering point.

Properties (1) and (2) are known as *Axiom A* and *Strong Transversality*, respectively; they can be extended to vector fields, which are related to diffeomorphisms by way of considering a Poincaré map. Systems (vector fields or diffeomorphisms) satisfying these two properties are also called *hyperbolic systems* since they exhibit hyperbolic recurrent dynamics in the following sense: every periodic orbit is hyperbolic, and there is a hyperbolic connecting orbit from any one periodic orbit to itself or to any other periodic orbit. In particular, hyperbolic systems do not have nontransverse intersections of stable and unstable manifolds and, therefore, their dynamics is considered relatively simple. A famous example is Smale's horseshoe construction in the plane [30]. For example, the existence of a *homoclinic tangency*, which is a tangential intersection of the stable and unstable manifolds of a saddle periodic fixed or periodic point (for a diffeomorphism) or a periodic orbit (for a vector field), implies that the system is nonhyperbolic since Strong Transversality is not satisfied. However, a generic perturbation creates two nearby transverse homoclinic points or destroys the intersection altogether. In either case, the homoclinic tangency violating Strong Transversality no longer exists. It turned out that hyperbolicity is only typical for diffeomorphisms of dimension at most two and, equivalently, vector fields of dimension at most three. While Newhouse [26] showed that a planar diffeomorphism can have robust homoclinic tangencies, meaning that all nearby planar diffeomorphisms also have a homoclinic tangency of the same type, his proof requires the C^2-topology (nearby systems are also close in their second derivatives). Moreira [25] later showed that planar diffeomorphisms cannot have C^1-robust homoclinic tangencies.

Robustness (in the C^1-topology) of nonhyperbolicity for systems of higher dimensions was shown via the existence of a so-called *heterodimensional cycle* between two saddle periodic orbits of different *index*, defined as the number of unstable eigenvalues or Floquet multipliers. The requirement that the unstable dimensions (and, therefore, the stable ones) of the two periodic orbits are different implies that the phase space must have dimension at least three for diffeomorphisms and at least four for flows. A heterodimensional cycle involves one intersection set between the repsective lower-dimensional invariant manifolds of the two periodic orbits, which is necessarily non-transverse and, therefore, violates Strong Transversality. Typically, this intersection is *quasi-transverse*, meaning that the tangent spaces of the invariant manifolds at their intersection share only the flow direction (for vector fields), or do not share any direction in the case of diffeomorphisms [5]. Similar to a homoclinic tangency, a quasi-transverse heteroclinic connection breaks under a generic perturbation. However, Abraham and Smale [1] constructed a four-dimensional diffeomorphism with a *robust* heterodimensional cycle. An important part of the theory is the result by Bonatti and Díaz [6] that a heterodimensional cycle between two saddle periodic orbits can be *stabilised* into a robust heterodimensional cycle. More precisely, this is achieved by constructing an arbitrarily C^1-close system that embeds one of the two periodic orbits into a more complicated hyperbolic set known as a *blender*, which has an invariant manifold whose dimension exceeds that given by the index of the periodic orbit [6]. For a three-dimensional diffeomorphism, such a manifold is technically one dimensional, but functionally it behaves as a two-dimensional manifold in the sense that it cannot be 'avoided' by the one-dimensional invariant manifold of the other saddle; this property allows a quasi-transverse intersection with this manifold of the blender to 'persist' even after a generic perturbation. Li and Turaev [24] proved this result in the C^r-topology for any $r \in \mathbb{N}$. Bonatti conjectured that, in the C^1-topology, robust heterodimensional cycles are more prevalent than robust homoclinic tangencies, suggesting that heterodimensional cycles are especially useful in understanding robust nonhyperbolicity.

In this paper, we investigate the prevalence of heterodimensional cycles in an example vector field, called the Atri model; see already Sec. 2 for details and particularly the explicit equations (1) of this four-dimensional model for intracellular calcium oscillations. The Atri model is one of the very few vector fields for which an explicit heterodimensional cycle has been identified and numerically approximated. Zhang et al. [32] employed the advanced computational technique known as *Lin's method* (see Appendix A) to find a heterodimensional cycle, and further computational

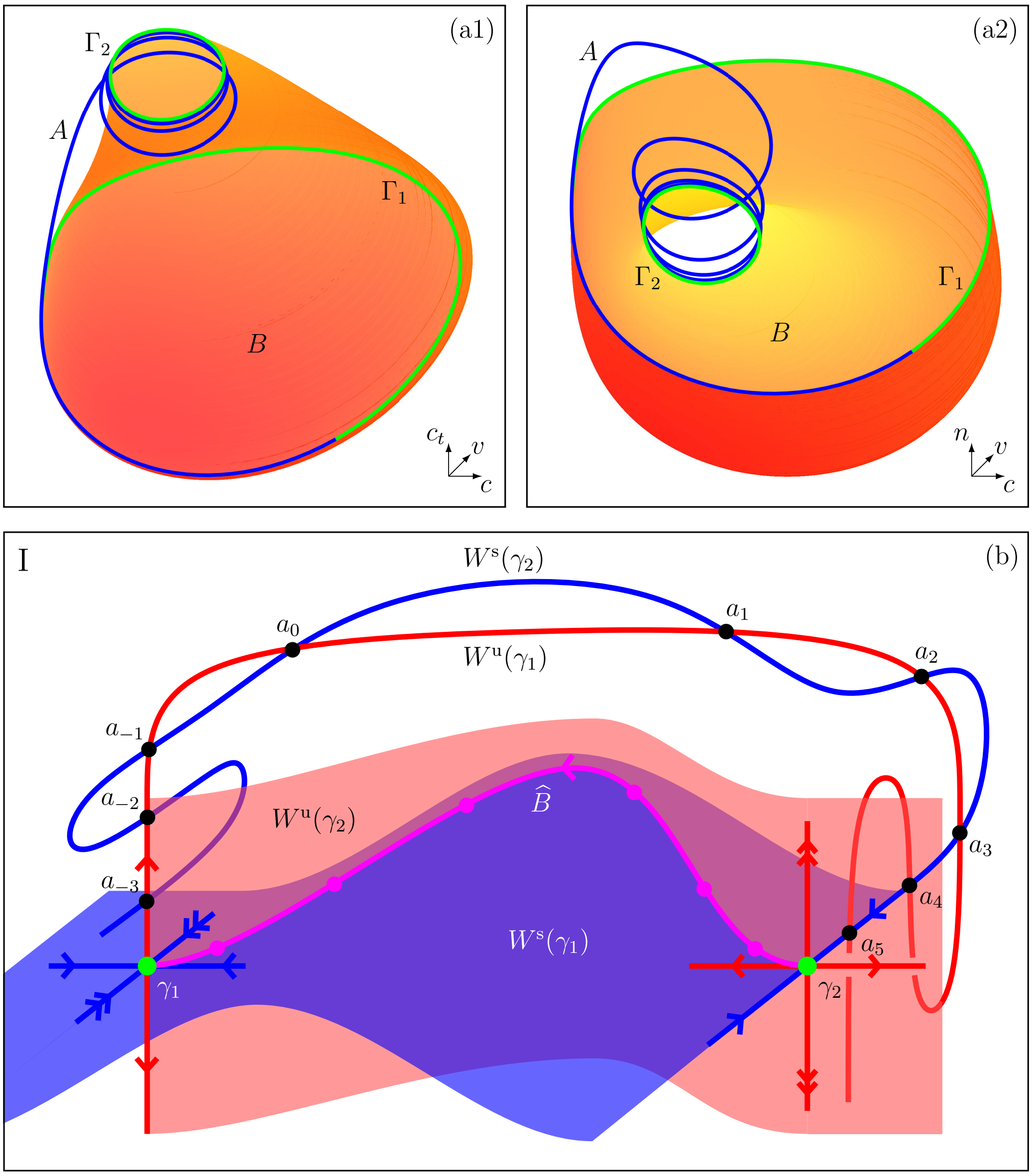

Figure 1: The primary heterodimensional cycle of system (1) at the parameter point $(J, s) \approx (3.061, 8.55)$ in region I (introduced in Fig. 3). Panels (a1) and (a2) show, in projection onto (c, v, c_t)-space and (c, v, n)-space, respectively, the saddle periodic orbits Γ_1 and Γ_2 (green curves), the codimension-one orbit A (blue), and the surface B (orange) of return connections. Panel (b) is a sketch of this type of heterodimensional cycle at the level of a three-dimensional diffeomorphism. The fixed points γ_1 and γ_2 (green) correspond to Γ_1 and Γ_2, respectively, the orbit $(a_k)_{k\in\mathbb{Z}}$ (black dots) is the quasi-transverse intersection of the curves $W^{\mathrm{u}}(\gamma_1)$ (red) and $W^{\mathrm{s}}(\gamma_2)$ (blue), and the curve $\widehat{B}$ (magenta) is the transverse intersection of the surfaces $W^{\mathrm{u}}(\gamma_2)$ (red) and $W^{\mathrm{s}}(\gamma_1)$ (blue); also shown is a sample orbit (magenta dots) in $\widehat{B}$.

work by Mason et al. [19] showed, in phase space and in a three-dimensional Poincaré section, how the invariant manifolds of the associated periodic orbits intersect to form the heterodimensional cycle. As in these earlier studies, we focus our attention on the two-parameter plane given by the parameters J and s of system (1). Figure 1 illustrates a heterodimensional cycle for the choice $(J, s) \approx (3.061, 8.55)$ in the parameter region I that represents the simplest case of such heterodimensional cycles, which are all topologically the same as the one found in [19, 32]. Panels (a1) and (a2) show different three-dimensional projections of saddle periodic orbits Γ_1 and Γ_2, which have different indices. The two-dimensional unstable manifold $W^{\mathrm{u}}(\Gamma_1)$ of Γ_1 intersects the two-dimensional stable manifold $W^{\mathrm{s}}(\Gamma_2)$ of Γ_2 in the heteroclinic connection A from Γ_1 to Γ_2. This codimension-one connection is quasi-transverse and is encountered at an isolated parameter value when a single parameter is varied (in fact, we computed it by varying the parameter J for fixed parameter $s = 8.55$). In contrast, the unstable manifold $W^{\mathrm{u}}(\Gamma_2)$ and stable manifold $W^{\mathrm{s}}(\Gamma_1)$ are both three dimensional and intersect transversely in the surface B, which is a topological cylinder consisting of heteroclinic connections from Γ_2 back to Γ_1; this cylinder is structurally stable, that is, it persists under parameter perturbations. Figure 1(b) shows a sketch of this geometric object at the level of a three-dimensional diffeomorphism, which illustrates how the heterodimensional cycle arises from the quasi-transverse intersection of the invariant manifolds of two corresponding saddle fixed points γ_1 and γ_2; a similar sketch can be found in [32]. The heteroclinic orbit $(a_k)_{k\in\mathbb{Z}}$ is the intersection of the one-dimensional invariant manifolds $W^{\mathrm{u}}(\gamma_1)$ and $W^{\mathrm{s}}(\gamma_2)$ and corresponds to the connection A. The transverse intersection of the two-dimensional invariant manifolds $W^{\mathrm{u}}(\gamma_2)$ and $W^{\mathrm{s}}(\gamma_1)$ is the single curve $\widehat{B}$; it corresponds to the surface B and consists of heteroclinic orbits from γ_2 back to γ_1. We base this sketch on theoretical considerations that are supported in system (1) by careful computations of the relevant objects on suitably chosen three-dimensional Poincaré sections. We remark that sketches in the theoretical literature generally focus on the one-dimensional invariant manifolds [5, 6]. The heterodimensional cycle of the Atri model in Fig. 1 is formed by the connection A and the surface B; at the level of a diffeomorphism, it is formed equivalently by the orbit $(a_k)_{k\in\mathbb{Z}}$ and the curve $\widehat{B}$. We refer to the heterodimensional cycle in Fig. 1 as the *primary heterodimensional cycle*. The primary heterodimensional cycle is a particularly simple example since the Atri model is of the minimal dimension required for heterodimensional cycles, and the surface B is a topological cylinder.

The primary heterodimensional cycle forms a suitable starting point for our investigation into bifurcations of a heterodimensional cycle in the Atri model. We show that, when it is continued further, this primary cycle undergoes a number of transitions that change the geometric properties of the surface B. This culminates in a period-doubling bifurcation of Γ_2, beyond which the primary cycle is no longer heterodimensional due to the resulting change in the index of Γ_2. However, this is not the end of the story, and this 'period doubling' of the primary heterodimensional cycle creates new families of different heterodimensional cycles. We present these 'period-doubled heterodimensional cycles' and their geometric properties, and continue them in the system parameters J and s. We find that these new families encounter the same geometric transitions as the primary heterodimensional cycle, and further period-doubling bifurcations create yet more heterodimensional cycles, and so on. By detecting and continuing these different cycles, we uncover and present a comprehensive picture in the (J, s)-plane of how a cascade of bifurcations generates a plethora of heterodimensional cycles of different types. This demonstrates the abundance of heterodimensional cycles in the Atri model and, hence, provides a glimpse into how a robust heterodimensional cycle may manifest itself in an actual vector field.

We achieve these results by adapting and employing state-of-the-art techniques of numerical bifurcation theory. The periodic orbits involved, together with their Floquet multipliers, Floquet bundles, and bifurcations, can be found with established continuation tools; we use the continuation software AUTO [13, 14] for this purpose. We then set up a boundary value problem (BVP) that defines two orbit segments in the stable or unstable manifold of a periodic orbit via projection boundary conditions [4]. These are combined to find and then continue connecting orbits of different types; see [21, 32] for a thorough discussions of this approach. Central is the use of continuation to close a 'gap' between the endpoints of the two orbit segments; the general setup, known as *Lin's method*, provides a well-defined direction along which the *Lin gap* is measured. We implement Lin's method in AUTO by making use of its collocation-based BVP solver and pseudo-arclength continuation, which enables us to identify connecting orbits as zeroes of the Lin gap. The computed objects are rendered and visualised in three-dimensional projections and in three-dimensional local Poincaré sections; the latter is also achieved with a BVP setup by imposing that one endpoint of each orbit segment of the respective family lies in a chosen section.

Overall, our numerical investigation of explicit heterodimensional cycles contributes to the emerging bifurcation theory of heterodimensional cycles, following on from initial work by Li and Turaev [24]. The results presented here also align in spirit with more recent efforts [12] to understand how the geometric properties of a heterodimensional cycle can theoretically affect the dynamics of a system. Moreover, we showcase how state-of-the-art numerical methods are an important tool for uncovering novel types of dynamics and providing insight into the underlying geometric structure.

The paper is organised as follows. In Sec. 2, we introduce the Atri model and its basic bifurcation diagram in the (J, s)-plane with the curve **PtoP** (which stands for Periodic to Periodic), along which one finds the connection A and, in fact, the entire primary heterodimensional cycle. Section 3 then shows how the heterodimensional cycle changes as it is continued along **PtoP** towards the curve **PD** of period-doubling bifurcations. More specifically, the topological cylinder $B = W^{\mathrm{u}}(\Gamma_2) \cap W^{\mathrm{s}}(\Gamma_1)$ changes geometrically because real pairs of Floquet multipliers of Γ_1 and Γ_2 become complex conjugate, and those of Γ_2 subsequently become real again but negative. The endpoint of **PtoP** on **PD** is a global codimension-two bifurcation, and we show in Sec. 4 how it generates novel types of heterodimensional cycle, which we informally call 'period-doubled heterodimensional cycles'. We start in Sec. 4 by presenting the bifurcation structure near this special point. Section 4.1 then shows that the primary heterodimensional cycle can be continued past the curve **PD** as a codimension-one strong heteroclinic cycle between Γ_1 and Γ_2, which returns to Γ_2 along its one-dimensional strong stable manifold. When the strong heteroclinic cycle is perturbed, one finds the structurally stable situation discussed in Sec. 4.2. Nearby, new heterodimensional cycles involving the period-doubled orbit emerging at **PD** can be found, as is explained in Secs. 4.3, 4.4 and 4.5. These new heterodimensional cycles can then bifurcate as well when further period-doubling bifurcations are encountered. We explain this phenomenon of cascading heterodimensional cycles in Sec. 5 by presenting an overall bifurcation scenario that creates infinitely more period-doubled heterodimensional cycles. In Sec. 6, we draw some conclusions and point to future work. Further details of how certain heterodimensional cycles were found and computed can be found in Appendix A.

2 The Atri model and its basic bifurcation diagram

The specific model we study is the four-dimensional system of ordinary differential equations (ODEs)

$$\begin{cases} \dot{c} &= v, \\ D_c\dot{v} &= s\,v - \left(\alpha + \frac{k_f c^2}{c^2+\varphi_1^2} n\right)\left(\frac{\gamma(c_t + D_c v - s\,c)}{s} - c\right) + k_s c - \delta(J - k_p c), \\ \dot{c_t} &= \delta(J - k_p c), \\ s\,\dot{n} &= \frac{1}{\tau}\left(\frac{\varphi_2}{\varphi_2 + c} - n\right), \end{cases} \tag{1}$$

It is known as the Atri model [2, 32, 33] and describes how the calcium concentration inside a cell is related to changes in the cell's electrical charge; see [7] for a general discussion of how this and similar calcium models are derived. The Atri model incorporates two mechanisms: calcium is released from, or absorbed into, an internal calcium store called the endoplasmic reticulum; and calcium can enter or exit the cell through its membrane. The four state variables of system (1) represent: the calcium concentration c inside the main body of the cell; the voltage v of the cell; the total calcium level c_t, which also accounts for the stored calcium; and the proportion n of active chemical gates that release calcium from the endoplasmic reticulum.

α	γ	δ	J	k_f	k_p	k_s	φ_1	φ_2	D_c	s	τ
0.05	5.0	0.2	varies	20.0	20.0	20.0	2.0	1.0	25.0	varies	2.0

Table 1: Parameters of system (1).

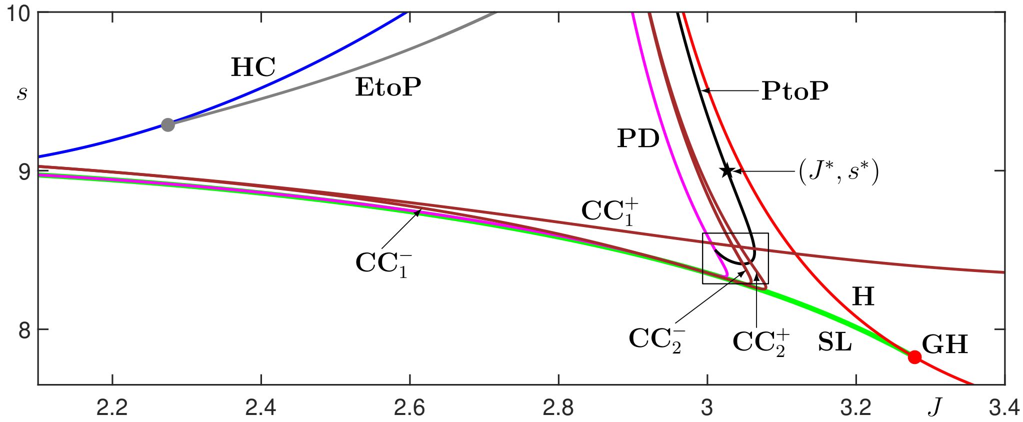

Figure 2: Bifurcation diagram in the (J, s)-plane of system (1) with curves **H** (red) of Hopf bifurcations, **SL** (green) of saddle-node bifurcations of the periodic orbits, **PD** (magenta) of period-doubling bifurcations, **HC** (blue) of homoclinic orbits, **EtoP** (gray) of codimension-one EtoP cycles, and **PtoP** (black) of the primary heterodimensional cycle with the point $(J^*, s^*) \approx (3.0266, 9.0)$ where the first heterodimensional cycle was found in [32]; also shown is the codimension-two point **GH** (red) of generalised Hopf bifurcation. Along the curves $\mathbf{CC}_1^\pm$ and $\mathbf{CC}_2^\pm$ (brown) the periodic orbit Γ_1 and Γ_2, respectively, has a positive/negative real double Floquet multiplier. The region in the black frame is enlarged in Fig. 3(a).

The physiological context of the Atri model (1) is not the focus here. Rather, our interest lies in the fact the Arti model is the first and still only example of an explicitly given, concrete four-dimensional vector field with a heterodimensional cycle [19, 32]. As in previous work, we consider J and s as the bifurcation parameters of our study and fix all other parameters at the values given in Table 1.

Our starting point is the bifurcation diagram in Fig. 2, which shows the relevant basic bifurcation curves known from previous work [19, 32]. Along the curve **H** the only equilibrium p of system (1) undergoes a Hopf bifurcation, which changes criticality at the generalised Hopf bifurcation point **GH**. From **GH** emerges the curve **SL** along which there is a saddle-node or fold bifurcation where two periodic orbits meet and disappear. In fact, the periodic orbits Γ_1 and Γ_2 in Fig. 1 meet along the curve **SL**, and they exist above **SL** and to the left of the curve **H**. The periodic orbit Γ_2 shrinks to the equilibrium p and disappears along the segment of **H** above the point **GH**. Along the curve **HC** the periodic orbit Γ_2 vanishes by becoming a codimension-one homoclinic orbit to p. We conclude that both Γ_1 and Γ_2 exist in the 'triangular' region of the (J, s)-plane that is bounded by the curves **H**, **SL** and **HC**. We remark that this so-called "CU-structure" involving the curves **H** and **HC** is found in quite a number of ODE models of calcium waves [7, 31]. Figure 2 also shows a curve **PD** of period doubling, which is tangent to the curve **SL** at a codimension-two saddle-node period-doubling point [23] near $J = 3$. Along the part of **PD** to the left of this point there is a period-doubling bifurcation of Γ_1, while to the right there is a period-doubling bifurcation of Γ_2. Note that the right part of **PD** turns sharply and then effectively runs parallel to the curve **H** at some distance. The two periodic orbits Γ_1 and Γ_2 of different index coexist in the region bounded by the curves **H**, **SL** and **PD**.

A further ingredient of the bifurcation diagram in Fig. 2 is the curve **EtoP** along which one finds a codimension-one Equilibrium-to-Periodic (EtoP) cycle between the equilibrium p and the periodic orbit Γ_1. This cycle consists of a codimension-one non-transverse connection from p to Γ_1 and a single structurally stable return connection. Since the periodic orbit Γ_2 is close to p near the curve **H**, the existence of an EtoP cycle in this region suggests that there might also be a heteroclinic PtoP cycle between Γ_1 and Γ_2. This observation was behind the initial discovery by Zhang et al. [32] of the primary heterodimensional cycle, which exists along the curve **PtoP** in Fig. 2. The heterodimensional cycle shown and studied in [19, 32] is the one at $(J^*, s^*) \approx (3.0266, 9.0)$, and the curve **PtoP** was also computed in these earlier works by continuation. Mason et al. [19] found that **PtoP** ends at a point on the curve **PD**, where the periodic orbit Γ_2 undergoes period doubling. Namely, the index of Γ_2 to the left of **PD** is no longer different from the index of Γ_1, so that there can no longer be a heterodimensional cycle between these two periodic orbits.

3 Geometrical changes to the primary PtoP cycle

At the original parameter point $(J^*, s^*) \approx (3.0266, 9.0)$, as well as at $(J, s) \approx (3.061, 8.55)$ as used in Fig. 1, the periodic orbits Γ_1 and Γ_2 have real and positive Floquet multipliers. However, the two unstable Floquet multipliers of Γ_2 are negative and real near the period-doubling bifurcation, since at **PD**, one of them is -1. This sign change necessitates the transition through two codimension-one situations where they coalesce to form a real double Floquet multiplier of Γ_2 that splits into a complex-conjugate pair, and vice versa. We also find similar changes for Γ_1, and the associated loci for Γ_1 and Γ_2 are referred to as $\mathbf{CC}_1^{\pm}$ and $\mathbf{CC}_2^{\pm}$, respectively, where the sign denotes whether the double Floquet multiplier is positive or negative.

The loci $\mathbf{CC}_1^{\pm}$ and $\mathbf{CC}_2^{\pm}$ are part of the bifurcation structure shown in Fig. 2, where they were continued as solutions of a suitably defined BVP; see [16] for the details. Each of the curves $\mathbf{CC}_2^{\pm}$ end on **SL** at a codimension-two point (not indicated), and the curve $\mathbf{CC}_1^{-}$ is actually the continuation (to the left) of $\mathbf{CC}_2^{-}$ past this point. These details are beyond our focus here. Rather, the key observation is that the curve **PtoP** crosses first $\mathbf{CC}_1^{+}$, then $\mathbf{CC}_2^{+}$ and finally $\mathbf{CC}_2^{-}$ before ending on **PD**, which all happens inside the black frame in Fig. 2.

This transition is illustrated in Fig. 3, which enlarges the region in the black frame in Fig. 2. The curves $\mathbf{CC}_1^{+}$ and $\mathbf{CC}_2^{\pm}$ divide the parameter space to the right of the curve **PD** into subregions. In each subregion, the two Floquet spectra of Γ_1 and Γ_2 are in a specific configuration depending on whether their respective multipliers are real or complex, and with positive or negative real parts as shown in the accompanying sketches. We shade the subregions visited by the curve **PtoP** and refer to them as regions I to IV. Note that region I extends beyond the shown (J, s)-range.

Figure 3(a) highlights selected points on the curve **PtoP**, chosen from each of the regions I—IV, at which we compute and present the primary heterodimensional cycle as a representative example. The numerical values of the corresponding Floquet multipliers of Γ_1 and Γ_2 are given in Table 2. The primary heterodimensional cycle we showed in Fig. 1 represents region I, where Γ_1 and Γ_2 have positive Floquet multipliers, one and two of which are unstable, respectively. This configuration of their Floquet multipliers is the reason behind the primary heterodimensional cycle in region I being called "simple" [5]: it is of minimal dimension and the structurally stable connection B is a cylinder. Note that B is tangent to the two-dimensional linear bundle of the weak stable Floquet multiplier λ_1^{s} of Γ_1 and of the weak unstable Floquet multiplier λ_2^{u} of Γ_2; see Fig. 1(b). Notice also from Table 2 that there is a considerable difference between the weak and the strong Floquet multipliers, especially of Γ_1.

At $\mathbf{CC}_1^{+}$, the periodic orbit Γ_1 has a positive real, double stable Floquet multiplier. In the adjacent region II, this double multiplier has separated into a complex-conjugate pair with positive real part. The unstable Floquet multiplier λ_1^{u} of Γ_1 is also positive real. This configuration of the spectrum of Γ_1 is retained throughout regions II to IV. At $\mathbf{CC}_2^{+}$, the periodic orbit Γ_2 has a positive real, double unstable Floquet multiplier. In region III, this double multiplier has separated into a

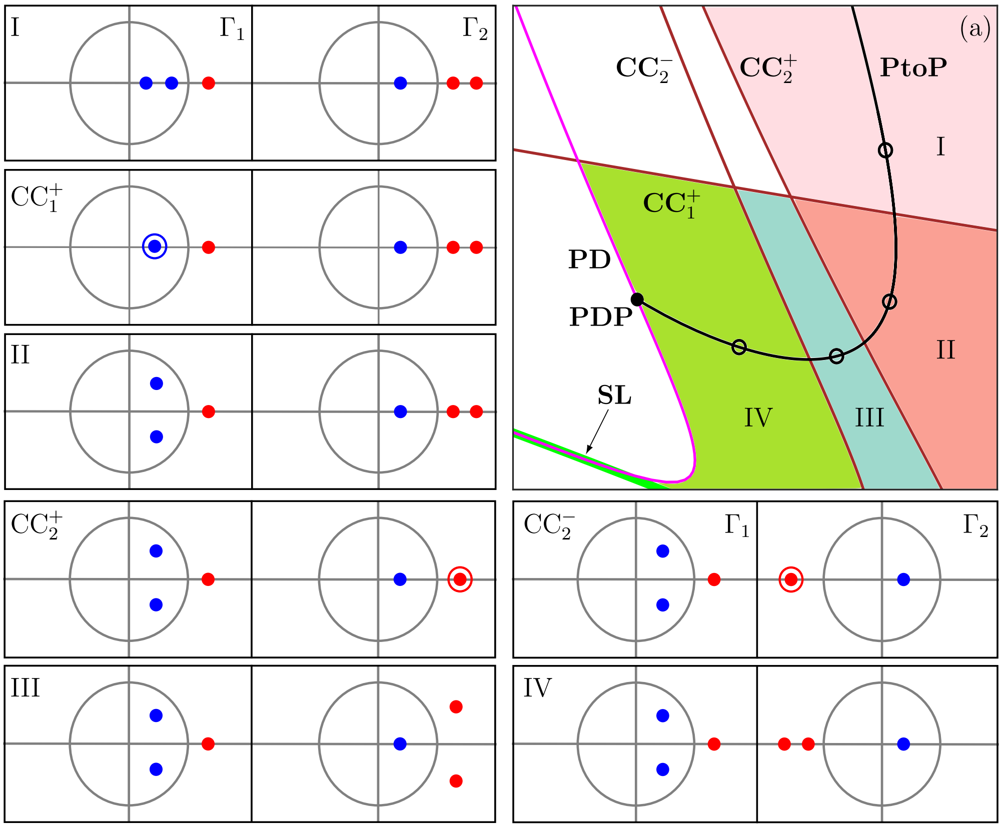

Figure 3: Transition of the Floquet spectra of both Γ_1 and Γ_2 along the curve **PtoP**. Panel (a) is an enlargement of the black frame in Fig. 2 with the regions I–IV (shaded in different colours), which are separated by the curves $\mathbf{CC}_1^+$ and $\mathbf{CC}_2^\pm$ (brown); the open circles indicate the (J, s)-parameter points for Figs. 1, 4, 6 and 8, respectively. The Floquet spectra of Γ_1 (left) and Γ_2 (right) during the transition are sketched in the complex plane in the other panels; here stable multipliers (inside the unit circle) are shown blue and unstable ones red.

	J	s	Γ_1	Γ_2
I	3.061	8.550	stable : $\begin{cases} \lambda_1^{ss} \approx 7.558 \times 10^{-2} \\ \lambda_1^{s} \approx 2.009 \times 10^{-1} \end{cases}$ unstable : $\lambda_1^{u} \approx 4.749 \times 10^{3}$	unstable : $\begin{cases} \lambda_2^{u} \approx 1.925 \times 10^{0} \\ \lambda_2^{uu} \approx 1.539 \times 10^{2} \end{cases}$ stable : $\lambda_2^{s} \approx 3.544 \times 10^{-1}$
II	3.062	8.450	stable : $\begin{cases} \lambda_1^{s} \approx (1.396 + 0.907\,i) \times 10^{-1} \\ \overline{\lambda_1^{s}} \approx (1.396 - 0.907\,i) \times 10^{-1} \end{cases}$ unstable : $\lambda_1^{u} \approx 2.279 \times 10^{3}$	unstable : $\begin{cases} \lambda_2^{u} \approx 3.438 \times 10^{0} \\ \lambda_2^{uu} \approx 6.696 \times 10^{1} \end{cases}$ stable : $\lambda_2^{s} \approx 3.718 \times 10^{-1}$
III	3.053	8.414	stable : $\begin{cases} \lambda_1^{s} \approx (1.376 + 1.348\,i) \times 10^{-1} \\ \overline{\lambda_1^{s}} \approx (1.376 - 1.348\,i) \times 10^{-1} \end{cases}$ unstable : $\lambda_1^{u} \approx 1.689 \times 10^{3}$	unstable : $\begin{cases} \lambda_2^{u} \approx (-8.214 + 14.46\,i) \times 10^{-1} \\ \overline{\lambda_2^{u}} \approx (-8.214 - 14.46\,i) \times 10^{-1} \end{cases}$ stable : $\lambda_2^{s} \approx 3.895 \times 10^{-1}$
IV	3.035	8.420	stable : $\begin{cases} \lambda_1^{s} \approx (1.280 + 1.449\,i) \times 10^{-1} \\ \overline{\lambda_1^{s}} \approx (1.280 - 1.449\,i) \times 10^{-1} \end{cases}$ unstable : $\lambda_1^{u} \approx 1.807 \times 10^{3}$	unstable : $\begin{cases} \lambda_2^{u} \approx -2.128 \times 10^{0} \\ \lambda_2^{uu} \approx -1.014 \times 10^{2} \end{cases}$ stable : $\lambda_2^{s} \approx 4.045 \times 10^{-1}$

Table 2: Floquet multipliers of Γ_1 and Γ_2 at the chosen points in regions I–IV that are marked on the curve **PtoP** in Fig. 3(a).

complex-conjugate pair that has positive real part near $\mathbf{CC}_2^+$. Moving along **PtoP** towards $\mathbf{CC}_2^-$, the two complex-conjugate unstable Floquet multipliers of Γ_2 stay outside the unit circle; however,

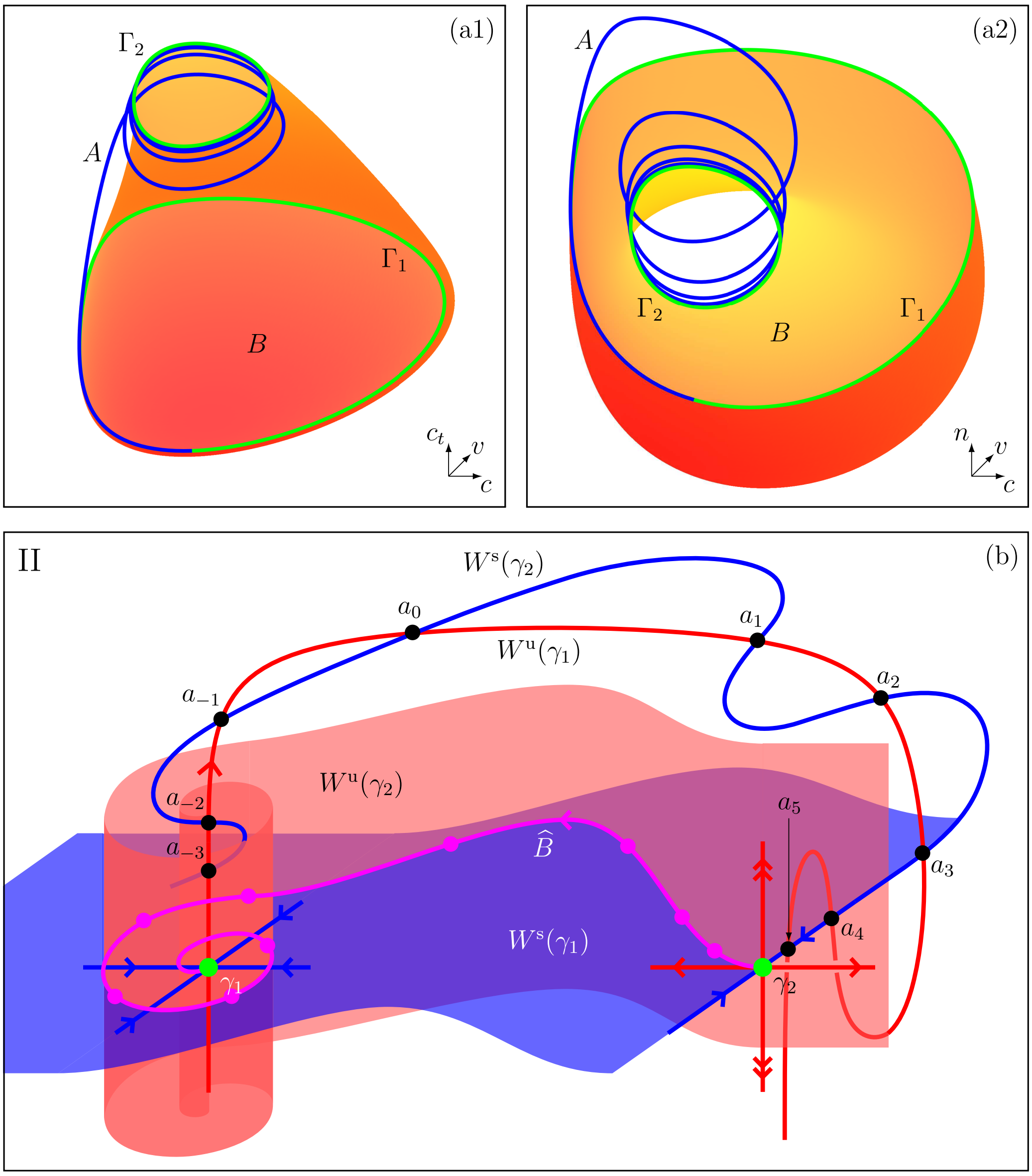

Figure 4: The primary heterodimensional cycle **PtoP** of system (1) at $(J, s) \approx (3.062, 8.45)$ in region II, illustrated as in Fig. 1.

they cross the imaginary axis, that is, their real part becomes negative. At $\mathbf{CC}_2^-$, these complex-conjugate multipliers meet at a negative real, double unstable Floquet multiplier. As **PtoP** crosses into region IV, this double multiplier of Γ_2 splits into two negative real ones, and the one closest to the unit circle approaches -1 as **PD** is approached.

3.1 The primary heterodimensional cycle in regions II, III and IV

We now show how the simple heterodimensional cycle in region I changes geometrically as the curve **PtoP** passes through regions II, III and IV. The corresponding computed representative PtoP cycles are shown in Figs. 4, 6 and 8 in the style of Fig. 1. The presented sketches at the level of a three-dimensional diffeomorphism are backed up in Figs. 5, 7 and 9, respectively, by computations of the relevant invariant objects in local Poincaré sections transverse to Γ_1 and Γ_2.

Figure 4 shows the primary heterodimensional cycle at $(J, s) \approx (3.062, 8.45)$ in region II, where

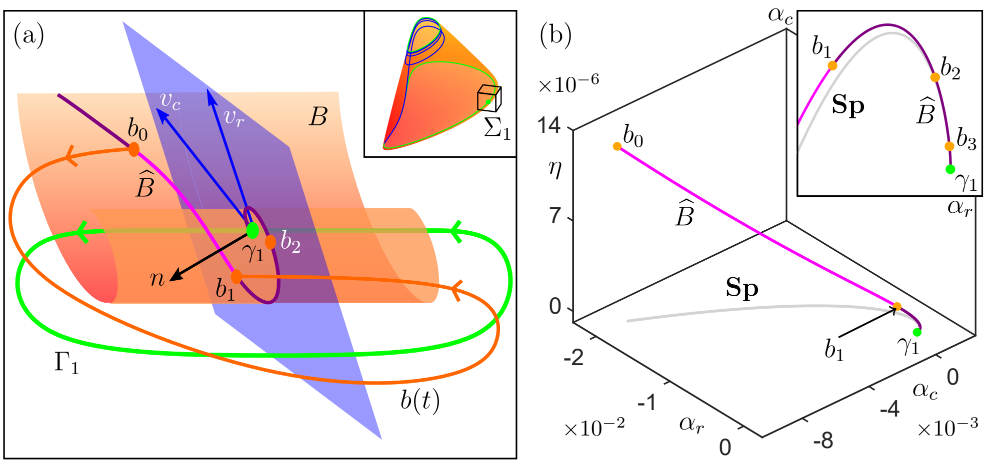

Figure 5: The computed heterodimensional cycle **PtoP** from region II in Fig. 4 shown in the three-dimensional local Poincaré section Σ_1 at the point $\gamma_1 \in \Gamma_1$ (green). Panel (a) sketches the setup, where the vectors v_r and v_c (blue arrows) are the real and the imaginary parts of a complex stable Floquet vector at γ_1, and the unit vector n (black arrow) is orthogonal to both v_r and v_c. The purple and magenta curve is the intersection $\widehat{B} = B \cap \Sigma_1$. In particular, the magenta segment of $\widehat{B}$ is a fundamental domain, whose starting point b_0 maps to its endpoint b_1 as indicated by the orbit segment $b(t)$ (orange); the inset shows the location of Σ_1 in (c, v, c_t)-space. Shown in panel (b) is a computation of $\widehat{B}$, where the axes are the coordinates α_r, α_c and η of the basis $\{v_r, v_c, n\}$ of Σ_1. The gray curve is the spiral **Sp** given by Eq. (2), and the inset shows the orthogonal projection of $\widehat{B}$ onto the (α_r, α_c)-plane.

Γ_1 and Γ_2 have the Floquet multipliers shown in Table 2. The fact that Γ_1 now has complex-conjugate stable Floquet multipliers means that trajectories in B spiral around Γ_1 as they converge to this periodic orbit in forward time. As a result, the surface B 'rolls up' around Γ_1. In the global views of panels (a1) and (a2), however, this is not discernible, owing to the fact that trajectories in B converge to Γ_1 with a large radial contraction of approximately 0.1665, while the angular rotation given by the complex part is quite weak. Nevertheless, at the level of a diffeomorphism, the situation is geometrically as sketched in Fig. 4(b), where the curve $\widehat{B} = W^{\mathrm{u}}(\gamma_2) \cap W^{\mathrm{s}}(\gamma_1)$ spirals around γ_1. Consequently, the two-dimensional unstable manifold $W^{\mathrm{u}}(\gamma_2)$ 'wraps around' the one-dimensional unstable manifold $W^{\mathrm{u}}(\gamma_1)$ because of the λ-lemma [18, 27]. Note that the situation near γ_2 is unchanged: the segment $\widehat{B}$ still approaches γ_2 along the weak unstable eigendirection, as in Fig. 1(b).

Figure 5 presents numerical evidence that, in a chosen Poincaré section Σ_1 transverse to Γ_1, the intersection set $\widehat{B} = \Sigma_1 \cap B$ indeed forms a logarithmic spiral around the point $\gamma_1 \in \Sigma_1 \cap \Gamma_1$. Panel (a) is a sketch of how the local flow near Γ_1 induces the intersection set $\widehat{B} = B \cap \Sigma_1$, and the inset illustrates the location of the local three-dimensional section Σ_1 used for the computation shown in panel (b). More specifically, the normal to Σ_1 at the chosen point $\gamma_1 = \Sigma_1 \cap \Gamma_1$ is defined as an adjoint Floquet vector at γ_1, and this implies that Σ_1 contains the Floquet vectors of Γ_1 at the point γ_1. In the sketch of panel (a), the vectors v_r and v_c are the real and the imaginary parts, respectively, of a complex stable Floquet vector at γ_1 associated with the complex stable multiplier λ_1^{s}; moreover, the unit vector n is orthogonal to both v_r and v_c, and these three vectors span Σ_1 at γ_1. Also illustrated in panel (a) is how the surface B intersects Σ_1 as the curve $\widehat{B}$: the orbit segment $b(t)$ starting at a point $b_0 \in \widehat{B}$ returns to Σ_1 under the flow at the image $b_1 \in \widehat{B}$ of the Poincaré map. Similarly, b_1 maps to $b_2 \in \widehat{B}$ and so on. Note that the highlighted segment between b_0 and b_1 is a fundamental domain of $\widehat{B}$ because any trajectory in B intersects it exactly once. Figure 5(b) shows the curve $\widehat{B}$ computed with a BVP setup as in [19]; here, the section Σ_1

is represented by the coordinates α_r, α_c and η along the vectors v_r, v_c and n, respectively, and the inset is the projection onto the (α_r, α_c)-plane. Note that the point $\gamma_1 \in \Sigma_1 \cap \Gamma_1$ is the origin $(0,0,0)$ in this representation. Also shown are points b_i for $i = 0,1,2,3$ of a single orbit that approaches γ_1 in forward time. To demonstrate that $\widehat{B}$ does indeed spiral towards γ_1, we show the associated logarithmic spiral $\mathbf{Sp}$ of the linearised Poincaré map near γ_1, given by

$$\mathbf{Sp} : \begin{cases} \begin{pmatrix} \alpha_r \\ \alpha_c \end{pmatrix} = r^k \begin{pmatrix} \cos(k\theta) & \sin(k\theta) \\ -\sin(k\theta) & \cos(k\theta) \end{pmatrix} \begin{pmatrix} \epsilon_r \\ \epsilon_c \end{pmatrix}, \\ \qquad \eta = 0, \end{cases} \tag{2}$$

where $(r, \theta) \approx (0.1665, 0.5763)$ are the polar coordinates of the complex stable Floquet multiplier λ_1^{s}, and $k \in \mathbb{Z}$ is the iteration index.

For the spiral $\mathbf{Sp}$, we choose the initial point $\varepsilon_r v_r + \varepsilon_c v_c$ as the orthogonal projection onto $E^{\mathrm{s}}(\gamma_1)$ of the point closest to γ_1 in the computed segment of $\widehat{B}$. Our computation of $\widehat{B}$ agrees quite well with $\mathbf{Sp}$. Since the same spiralling of $\widehat{B}$ occurs for any choice of $\gamma_1 \in \Gamma_1$, Fig. 5(b) constitutes numerical evidence that the surface B as a whole wraps around the periodic orbit Γ_1.

Figure 6 shows the primary PtoP cycle at $(J, s) \approx (3.053, 8.414)$ in region III, where now also the periodic orbit Γ_2 has two complex-conjugate unstable Floquet multipliers; see Table 2 for their exact values. Here, the associated change in the surface B from region II to region III is not discernible in the three-dimensional projections of panels (a1) and (a2). However, it is sketched in panel (b) at the level of a diffeomorphism, where the curve $\widehat{B}$ now also spirals towards γ_2, and the two-dimensional manifold $W^{\mathrm{s}}(\gamma_1)$ wraps around the one-dimensional manifold $W^{\mathrm{s}}(\gamma_2)$, according to the λ-lemma. Figure 7 illustrates this locally in two Poincaré sections Σ_1 transverse to Γ_1 and Σ_2 transverse to Γ_2, where we compute the intersection sets $\widehat{B} = B \cap \Sigma_1$ and $\widehat{B} = B \cap \Sigma_2$, respectively. The locations of Σ_1 and Σ_2 are shown in the inset of panel (a). As in Fig. 5, we represent each section in $(\alpha_r, \alpha_c, \eta)$-coordinates as given by the basis $\{v_r, v_c, n\}$ of the respective Poincaré section at the intersection point γ_i, and we also show the corresponding logarithmic spiral $\mathbf{Sp}$ in the (α_r, α_c)-plane. Figure 7(a) shows that $\widehat{B}$ is now spiralling slightly more near γ_1, compared to Fig. 5(b), due to the fact that the polar coordinates of λ_1^{s} are now $(r, \theta) \approx (0.1927, 0.7750)$, that is, there is less contraction and more rotation. The situation near γ_2 is shown in Fig. 7(b), where the polar coordinates of the complex unstable Floquet multiplier λ_2^{u} are $(r, \theta) \approx (14.49, 1.627)$. Hence, for each iteration of the local Poincaré map, there is very strong contraction in backward time, while the change in angle around γ_2 is marginal; nevertheless, the curves $\mathbf{Sp}$ given by Eq. (2) are still spirals, albeit very steep ones, and they are approached by $\widehat{B}$ near the respective origin of these local coordinates.

Figure 8 shows the primary PtoP cycle at $(J, s) \approx (3.035, 8.42)$ in region IV, where the two unstable Floquet multipliers of Γ_2 are real but negative. Hence, Γ_2 has a negative weak unstable Floquet multiplier λ_2^{u} close to -1 and a negative strong unstable Floquet multiplier λ_2^{uu} far from -1; see Table 2 for their values at this parameter point. Sketched in panel (b) at the level of a diffeomorphism, the two-dimensional manifold $W^{\mathrm{s}}(\gamma_1)$ still spirals around the one-dimensional manifold $W^{\mathrm{s}}(\gamma_2)$, but this spiral is now strongly 'compressed' in the strong unstable eigendirection $E^{\mathrm{uu}}(\gamma_2)$ of γ_2. A typical orbit in $\widehat{B}$ converges to γ_2 along the weak eigendirection; near γ_2, each iterate rotates by an angle approximately equal to π since both unstable Floquet multipliers of Γ_2 are negative. The spiralling of the curve $\widehat{B}$ near γ_2 implies that $\widehat{B}$ transversely intersects the one-dimensional strong unstable manifold $W^{\mathrm{uu}}(\gamma_2) \subset W^{\mathrm{u}}(\gamma_2)$ (represented in Fig. 8(b) by the strong unstable eigendirection). This intersection yields a structurally stable strong connecting orbit $(b_k^{\mathrm{uu}})_{k \in \mathbb{Z}} \subset \widehat{B}$, and some of the points b_k^{uu} are shown in the sketch together with local segments of $W^{\mathrm{uu}}(\gamma_2)$. The sequence (b_k^{uu}) corresponds to the connecting orbit $B^{\mathrm{uu}} = W^{\mathrm{uu}}(\Gamma_2) \cap W^{\mathrm{s}}(\Gamma_1) \subset B$ of the vector field, which we computed and show in panels (a1) and (a2).

Figure 9 presents numerical evidence for how the surface B in Fig. 8 intersects the three-dimensional Poincaré section Σ_2 transverse to Γ_2. In panel (a), we represent Σ_2 by the coordinates

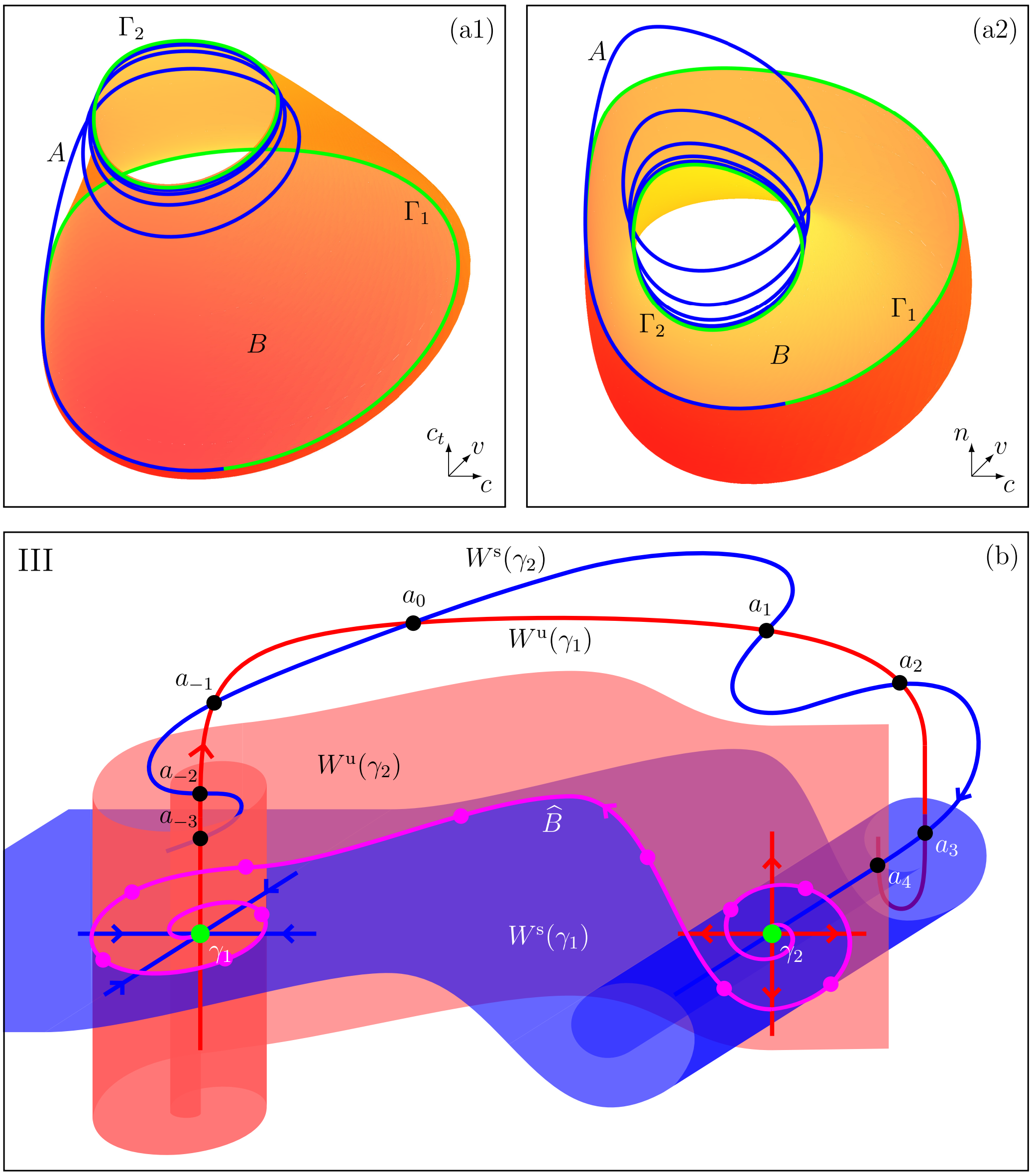

Figure 6: The primary heterodimensional cycle **PtoP** of system (1) at $(J, s) \approx (3.053, 8.414)$ in region III, illustrated as in Fig. 1.

$\alpha_{\mathrm{u}}, \alpha_{\mathrm{uu}}$ and α_{s} along the unit Floquet vectors $v^{\mathrm{u}}, v^{\mathrm{uu}}$ and v^{s}, respectively, at the chosen point $\gamma_2 \in \Sigma_2 \cap \Gamma_2$; the inset shows the location of Σ_2 in (c, v, c_t)-space. Since the strong unstable eigenvalue $\lambda_2^{\mathrm{uu}} \approx -1.014 \times 10^2$ is much larger than the weak unstable one $\lambda_2^{\mathrm{u}} \approx -2.128$, the curve $\widehat{B}$ is greatly compressed in the strong unstable direction (under backward iteration) and, hence, is a much 'flattened' spiral with sharp turning points (unlike in the idealised sketch in Fig. 8(b). In particular, the associated range of the coordinate α_{uu} is much smaller than that of α_{u}, and it turned out to be numerically unfeasible to compute $\widehat{B}$ as a single smooth curve at this resolution. However, with a suitable BVP setup, we are able to compute local segments of $\widehat{B} = B \cap \Sigma_2$ as they converge to $\gamma_1 = \Gamma_2 \cap \Sigma_2$. To illustrate the action of the Poincaré map, segments of $\widehat{B}$ are alternatingly coloured, meaning that each segment of one colour maps to a segment of the other, and vice versa. Panel (b) shows an extreme enlargement of panel (a) in projection onto the $(\alpha_{\mathrm{u}}, \alpha_{\mathrm{uu}})$-plane. Here, we see that $\widehat{B}$ strongly aligns with the weak unstable Floquet direction, and the two colours of $\widehat{B}$ approach γ_2 from opposite directions in the coordinate α_{uu}.

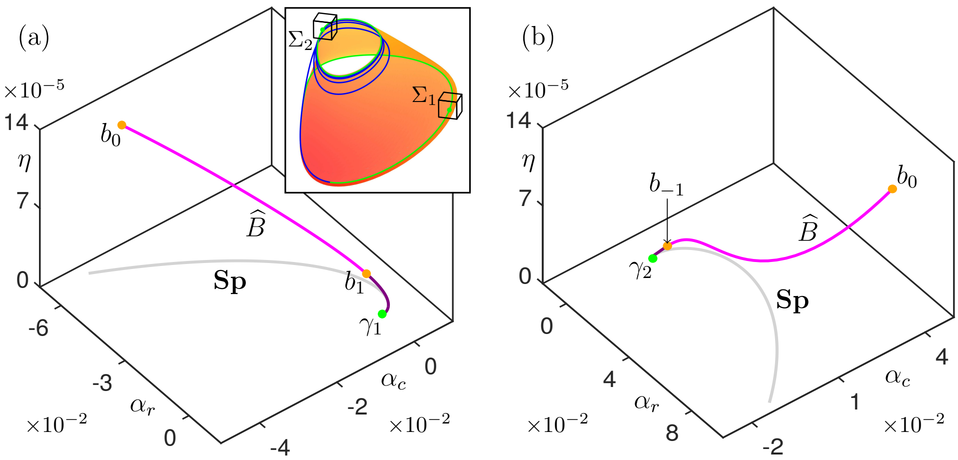

Figure 7: The computed heterodimensional cycle **PtoP** in region III from Fig. 6 at the level of the Poincaré maps on local sections Σ_1 at $\gamma_1 \in \Gamma_1$ in panel (a) and Σ_2 at $\gamma_2 \in \Gamma_2$ in panel (b). Shown is the respective curve $\widehat{B} = B \cap \Sigma_i$ in $(\alpha_r, \alpha_c, \eta)$-space with γ_i and the associated spiral **Sp** (gray) in the (α_r, α_c)-plane; the inset in panel (a) illustrates the locations of Σ_1 and Σ_2 in (c, v, c_t)-space. Compare with Fig. 5.

3.2 Strong homoclinic orbit to Γ_2 in region IV

Near the primary heterodimensional cycle in phase space there exist structurally stable homoclinic orbits to Γ_1 and Γ_2, some of which were computed in Zhang et al. [32] at the point $(3.0266, 9.0)$ in region I. Notably, those homoclinic orbits can be continued through the curves $\mathbf{CC}_1^+$, $\mathbf{CC}_2^+$ and $\mathbf{CC}_2^-$; that is, they also exist in regions II–IV. However, there are additional homoclinic orbits to Γ_1 and to Γ_2 that are generated by the spiralling nature of the surface B. More specifically, observe in Fig. 4(b) that the one-dimensional stable manifold $W^{\mathrm{s}}(\gamma_2)$ must transversely intersect the two-dimensional unstable manifold $W^{\mathrm{u}}(\gamma_2)$, because the latter rolls around $W^{\mathrm{u}}(\gamma_1)$ near γ_1; this follows from the fact that $W^{\mathrm{u}}(\gamma_1)$ intersects $W^{\mathrm{s}}(\gamma_2)$ in the codimension-one connecting orbit $(a_i)_{i\in\mathbb{Z}}$. An intersection between $W^{\mathrm{u}}(\gamma_2)$ and $W^{\mathrm{s}}(\gamma_2)$ corresponds to a robust homoclinic orbit to γ_2 that exists only below the curve $\mathbf{CC}_1^+$ in Fig. 3(a); note that this additional type of homoclinic orbit does not exist in region I, because the surface $W^{\mathrm{u}}(\gamma_2)$ approaches the curve $W^{\mathrm{u}}(\gamma_1)$ tangentially to the weak stable eigendirection of γ_1, while $W^{\mathrm{s}}(\gamma_2)$ accumulates on the one-dimensional manifold $W^{\mathrm{ss}}(\gamma_1)$; see Fig. 1(b). To the left of the curve $\mathbf{CC}_2^+$ in Fig. 3(a), the spiralling of $\widehat{B}$ towards γ_2 similarly induces robust homoclinic orbits to γ_1, since the quasi-transverse orbit $(a_i)_{i\in\mathbb{Z}}$ implies that the one-dimensional manifold $W^{\mathrm{u}}(\gamma_1)$ transversely intersects the two-dimensional manifold $W^{\mathrm{s}}(\gamma_1)$ near γ_2; see Figs. 6(b) and 8(b).

Any additional homoclinic orbits in $W^{\mathrm{u}}(\Gamma_2) \cap W^{\mathrm{s}}(\Gamma_2)$ near Γ_1 are extremely close to the primary heterodimensional cycle itself, owing to the very weak spiralling caused by the strong contraction rate on $W^{\mathrm{s}}(\Gamma_1)$ in regions II to IV. We attempted to find one numerically, but verifying that the computed homoclinic orbit is of the type generated by spiralling was not feasible; this is due to the fact that homoclinic orbits to Γ_2 in region I found in [32] already lie very close to the primary heterodimensional cycle. We are, however, able to find a new type of homoclinic orbit to Γ_2 in region IV: the codimension-one strong homoclinic orbit shown in Fig. 10. It is effectively a perturbation of the quasi-transverse connection A and the structurally stable strong connection B^{uu} from Fig. 8 that results in an intersection of the two-dimensional manifolds $W^{\mathrm{uu}}(\Gamma_2)$ and $W^{\mathrm{s}}(\Gamma_2)$ near Γ_1; in fact, the strong homoclinic orbit from Fig. 10 was computed with a BVP setup using these two connections as the starting data; see Appendix A. Panels (a1) and (a2) of Fig. 10 show the codimension-one strong homoclinic orbit **SHC** to Γ_2 at the point $(J, s) \approx (3.029, 8, 43)$ in

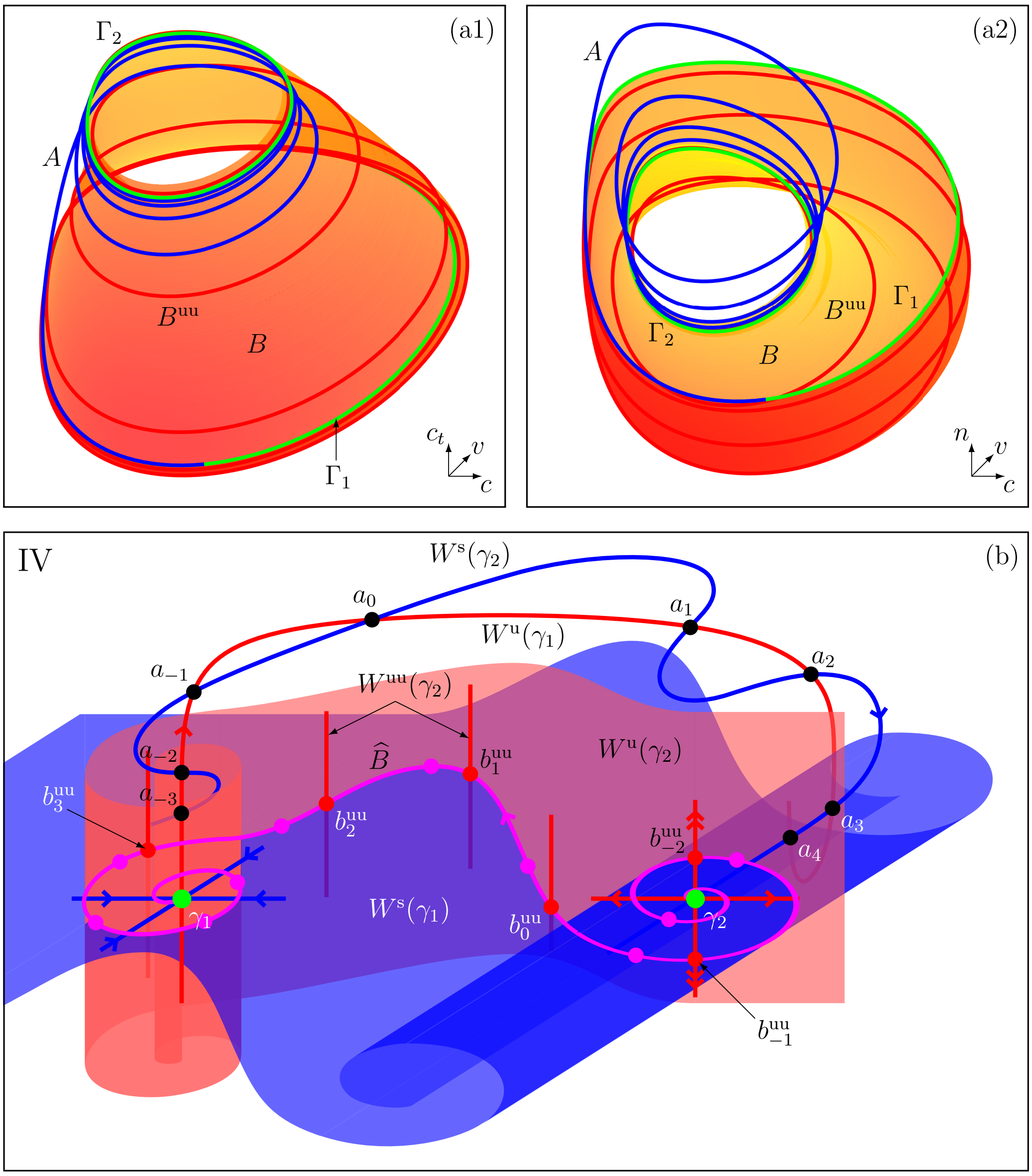

Figure 8: The primary heterodimensional cycle **PtoP** of system (1) at $(J, s) \approx (3.035, 8.42)$ in region IV, illustrated as in Fig. 1. Also shown is the strong connecting orbit $B^{\mathrm{uu}} \subset B$ (red curve) in panels (a1) and (a2), and its counterpart $(b_k^{\mathrm{uu}})_{k\in\mathbb{Z}}$ (red dots) in panel (b).

region IV, which is close to the point $(J, s) \approx (3.035, 8.42)$ of Fig. 8. The first part of the orbit **SHC** starts near Γ_2 and travels towards Γ_1 in close proximity to B^{uu}; subsequently, **SHC** makes several 'loops' around Γ_1 and then returns to Γ_2, with a trajectory that is similar to the codimension-one connection A, which does not exist after the perturbation; compare panels (a1) and (a2) of Fig. 10 with the corresponding panels of Fig. 8.

Figure 10(b1) is an idealised sketch of the situation near the fixed point γ_1. As in Fig. 8(b), which provides the global context of Fig. 10(b1), the curve $\widehat{B}$ spirals towards γ_1. The structurally stable strong connection $(b_k^{\mathrm{uu}})_{k\in\mathbb{Z}} = W^{\mathrm{uu}}(\gamma_2) \cap W^{\mathrm{s}}(\gamma_1) \subset B$ corresponds to B^{uu} and exists also near the curve **PtoP** in region IV. Its existence implies that $W^{\mathrm{uu}}(\gamma_2)$ follows $\widehat{B}$ towards γ_1 and approaches the one-dimensional manifold $W^{\mathrm{u}}(\gamma_1)$ as a consequence of the λ-lemma. Since the sketch in Fig. 10(b1) is a perturbation of the sketch in Fig. 8(b), segments of $W^{\mathrm{s}}(\gamma_2)$ lie near γ_1 and extend in a direction of the stable subspace $E^{\mathrm{s}}(\gamma_1)$. These segments (of which two are shown)

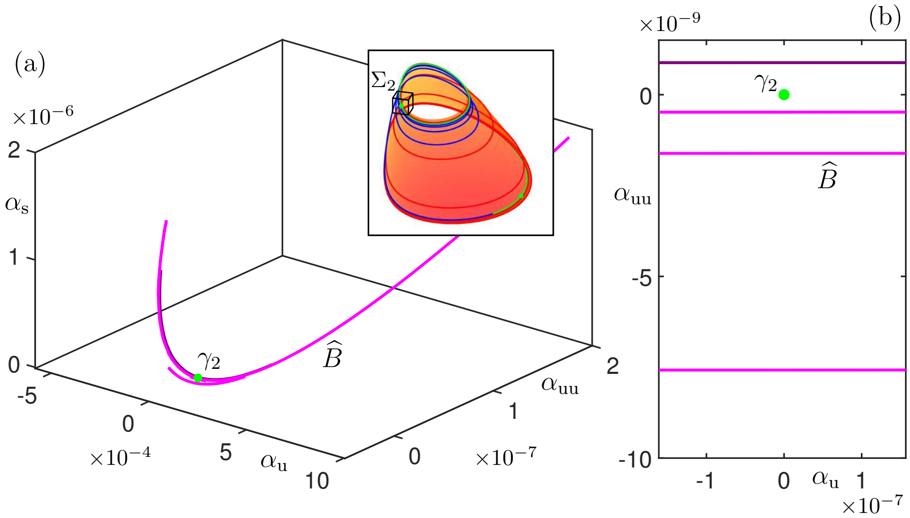

Figure 9: The computed heterodimensional cycle **PtoP** in region IV from Fig. 8 at the level of the Poincaré map on a local section Σ_2 at $\gamma_2 \in \Gamma_2$. Panel (a) shows computed segments of $\widehat{B} = B \cap \Sigma_2$ with γ_2 in $(\alpha_{\rm u}, \alpha_{\rm uu}, \alpha_{\rm s})$-space of the coordinates of the eigenbasis $\{v^{\rm u}, v^{\rm uu}, v^{\rm s}\}$ at γ_2, and panel (b) is an extreme enlargement of a projection onto the $(\alpha_{\rm u}, \alpha_{\rm uu})$-plane. Segments of $\widehat{B}$ of the same colour (magenta or purple) map to one another under the second iterate of the Poincaré map, and the inset in panel (a) illustrates the location of Σ_2 in (c, v, c_t)-space.

quasi-transversely intersect $W^{\rm uu}(\gamma_2)$ to form the codimension-one strong homoclinic orbit $(q_k)_{k\in\mathbb{Z}}$, which corresponds to the curve **SHC** in panels (a1) and (a2) of Fig. 10. Panel (b2) shows the 'top view' of panel (b1), namely its projection onto $E^{\rm s}(\gamma_1)$ along the unstable eigendirection $E^{\rm u}(\gamma_1)$; here, the points q_k and $b_k^{\rm uu}$ coincide due to local curve segments of $W^{\rm uu}(\gamma_2)$ being idealised as vertical lines.

4 Period-doubling of the primary heterodimensional cycle

We now focus on the region to the left of the period-doubling curve **PD**: here, Γ_1 and Γ_2 coexist with a third periodic orbit Γ_3 that is the 'period-doubled orbit' which emerges from the period-doubling bifurcation **PD** of Γ_2. Panel (a) of Fig. 11 shows this (J, s)-region with the relevant computed loci, and panel (b) is a corresponding topological sketch. The periodic orbit Γ_3 has positive Floquet multipliers and (unstable) index two just to the left of **PD**. Its two unstable Floquet multipliers are a complex-conjugate pair between the curves $\mathbf{CC}_3^+$ and $\mathbf{CC}_3^-$; these two curves lie very close together in panel (a), and they are shown separated in the sketch in panel (b). To the left of $\mathbf{CC}_3^-$, they are real and negative, and Γ_3 then has a period-doubling bifurcation along the curve $\overline{\mathbf{PD}}$. Continuing on from Sec. 3, we label and colour these (J, s)-regions as follows: region V between **PD** and $\mathbf{CC}_3^+$, region VI between $\mathbf{CC}_3^+$ and $\mathbf{CC}_3^-$, and region VII between $\mathbf{CC}_3^-$ and $\overline{\mathbf{PD}}$. Figure 11 also shows the locus $\mathbf{PtoP}^{\rm ss}$ of the strong heteroclinic cycle between Γ_1 and Γ_2, which is effectively the continuation of the primary heterodimensional cycle from the codimension-two endpoint **PDP** of the curve **PtoP**. However, the heteroclinic cycle along the curve $\mathbf{PtoP}^{\rm ss}$ is not heterodimensional since both Γ_1 and Γ_2 have index one; it will be presented and discussed in Sec. 4.1. The Floquet spectra of Γ_1, Γ_2 and Γ_3 in region V are shown in the bottom row of Fig. 11. Observe that both Γ_1 and Γ_2 have index one and Γ_3 has index two, so that there is the possibility of new types of heterodimensional cycles involving Γ_3. We proceed by showing that these, indeed, exist and are 'mediated' by the strong heteroclinic cycle in region V.

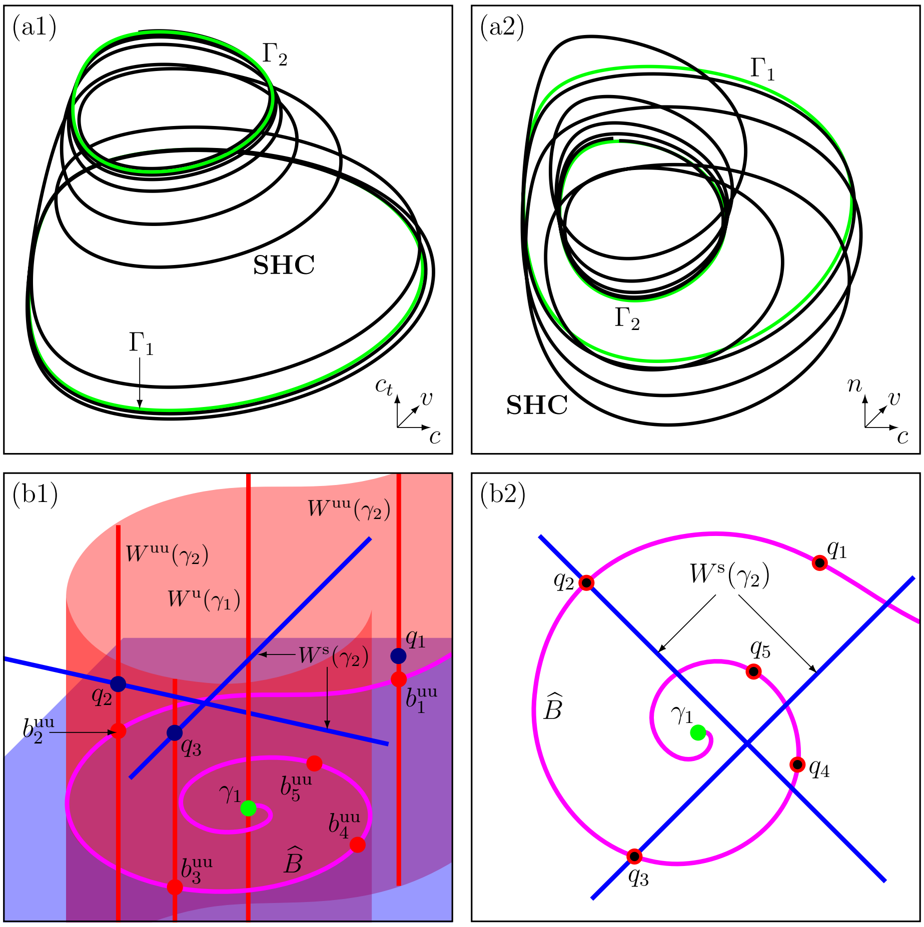

Figure 10: Strong homoclinic orbit **SHC** to Γ_2 of system (1) at $(J, s) \approx (3.029, 8, 43)$ in region IV. Panels (a1) and (a2) show **SHC** (black) with Γ_2 and Γ_2 (green) in projection onto (c, v, c_t)-space and (c, v, n)-space. Panel (b1) is a sketch of a representative diffeomorphism near γ_1, which illustrates how $W^{uu}(\gamma_2)$ intersects $W^{s}(\gamma_2)$ (blue) along the corresponding codimension-one strong homoclinic orbit $(q_k)_{k\in\mathbb{Z}}$ (black dots) to γ_2; see Fig. 8(b) for the global context. Also shown is the strong connecting orbit $(b_k^{uu})_{k\in\mathbb{Z}}$ (red dots) that corresponds to $B^{uu} = W^{uu}(\Gamma_2) \cap W^{s}(\Gamma_1)$. Panel (b2) shows the projection of panel (b1) onto $E^{s}(\gamma_1)$ in the direction of $E^{u}(\gamma_1)$.

4.1 The strong heteroclinic cycle PtoP^{ss}

Figure 12 shows the strong heteroclinic cycle **PtoP**^{ss} between the two index-one periodic orbits Γ_1 and Γ_2 at the point $(J, s) \approx (3.0158, 8.452)$ on the curve **PtoP**^{ss} in region V. The Floquet multipliers of Γ_1, Γ_2 and Γ_3 at this parameter point are given in Table 3. Note that the stable manifold $W^{s}(\Gamma_2)$ is of dimension three in region V, while the two-dimensional unstable manifold $W^{u}(\Gamma_2)$ is the natural continuation of the strong unstable manifold $W^{uu}(\Gamma_2)$ in region IV. The two projections in panels (a) and (b) show the two constituent connections between Γ_1 and Γ_2. Firstly, there is the single codimension-one strong connecting orbit $A = W^{u}(\Gamma_1) \cap W^{ss}(\Gamma_2)$; we refer to it again as A, because it the natural extension of the quasi-transverse connection $A = W^{u}(\Gamma_1) \cap W^{s}(\Gamma_2)$ in region IV. Secondly, there is the single structurally stable return orbit $B^{uu} = W^{u}(\Gamma_2) \cap W^{s}(\Gamma_1)$; in a slight abuse of notation, we refer to it as B^{uu} because it is the continuation of the single strong connecting orbit $B^{uu} = W^{uu}(\Gamma_2) \cap W^{s}(\Gamma_1)$ in region IV. Also shown are the period-doubled orbit Γ_3 and the surface $D = W^{u}(\Gamma_3) \cap W^{s}(\Gamma_1)$ of connecting orbits from Γ_3 to Γ_1. Note that the connecting orbit B^{uu} lies in the closure of D; together, they are the natural

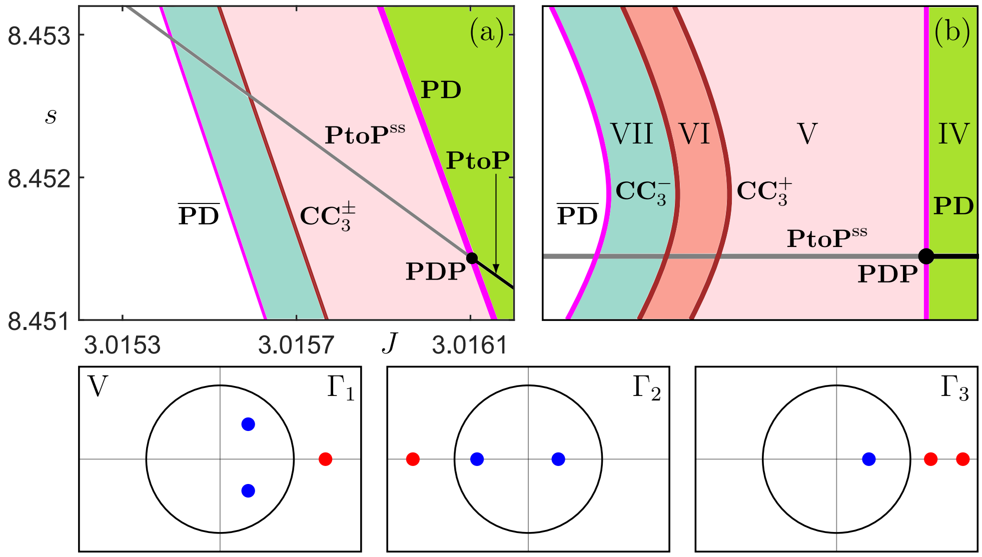

Figure 11: Bifurcation loci in the region $[3.0153, 3.0161] \times [8.451, 8.453]$ of the (J, s)-plane of system (1), showing the curves **PD** and $\overline{\textbf{PD}}$ (magenta) of period-doubling of Γ_2 and Γ_3, respectively, the curve $\textbf{PtoP}^{\rm ss}$ (gray) of the codimension-one strong heteroclinic cycle between Γ_1 and Γ_2, and the curves $\textbf{CC}_3^{\pm}$ (brown) of real double unstable Floquet multipliers of Γ_3. Also shown is the codimension-two point **PDP** at $(J, s) \approx (3.016, 8.451)$ on **PD**. Panel (a) shows the curves as computed, and panel (b) is a corresponding topological sketch that introduces regions V–VII bounded by **PD**, $\textbf{CC}_3^{\pm}$ and $\overline{\textbf{PD}}$. The bottom row shows the Floquet spectra of Γ_1, Γ_2 and Γ_3 in region V. Compare with Figs. 3(a) and 18.

continuation of the surface $B = W^{\rm u}(\Gamma_2) \cap W^{\rm s}(\Gamma_1)$ in region IV.

Γ_1		Γ_2		Γ_3	
stable :	$\lambda_1^{\rm s} \approx (1.175 + 1.245\, i) \times 10^{-1}$ $\overline{\lambda_1^{\rm s}} \approx (1.175 - 1.245\, i) \times 10^{-1}$	stable :	$\lambda_2^{\rm ss} \approx 4.094 \times 10^{-1}$ $\lambda_2^{\rm s} \approx -9.911 \times 10^{-1}$	unstable :	$\lambda_3^{\rm u} \approx 1.231 \times 10^{0}$ $\lambda_3^{\rm uu} \approx 1.860 \times 10^{4}$
unstable :	$\lambda_1^{\rm u} \approx 2.571 \times 10^{3}$	unstable :	$\lambda_2^{\rm u} \approx -2.451 \times 10^{2}$	stable :	$\lambda_3^{\rm s} \approx 4.116 \times 10^{-1}$

Table 3: Floquet multipliers of Γ_1, Γ_2 and Γ_3 at the parameter point $(J, s) \approx (3.0158, 8.452)$ of Fig. 12 on the curve $\textbf{PtoP}^{\rm ss}$ in region V.

The overall geometry of the relevant objects in region V is further illustrated in Fig. 12(b) at the level of a three-dimensional diffeomorphism; compare with Fig. 1(b). The heteroclinic cycle between the corresponding fixed points γ_1 and γ_2 consists of the strong connecting orbit $(a_k)_{k\in\mathbb{Z}}$, which is the quasi-transverse intersection of the one-dimensional manifolds $W^{\rm u}(\gamma_1)$ and $W^{\rm ss}(\gamma_2)$, and the structurally stable connecting orbit $(b_k^{\rm uu})_{k\in\mathbb{Z}} = W^{\rm u}(\gamma_2) \cap W^{\rm s}(\gamma_1)$. Also shown in Fig. 12(b) are the points γ_3^- and γ_3^+ of the period-two orbit $\boldsymbol{\gamma}_3 = (\gamma_3^-, \gamma_3^+)$, which correspond to Γ_3 and are fixed points of the second iterate of the diffeomorphism. The one-dimensional manifold $W^{\rm u}(\gamma_2)$ has two branches $W^{\rm u}_-(\gamma_2)$ and $W^{\rm u}_+(\gamma_2)$ that are each invariant under the second iterate, because the unstable Floquet multiplier $\lambda_2^{\rm u}$ is negative; moreover, $W^{\rm u}(\gamma_2)$ lies in the closure of the two-dimensional manifold $W^{\rm u}(\boldsymbol{\gamma}_3)$. Consequently, the connecting orbit $(b_k^{\rm uu})_{k\in\mathbb{Z}}$ lies in the closure of the intersection set $\widehat{D} = W^{\rm u}(\boldsymbol{\gamma}_3) \cap W^{\rm s}(\gamma_1)$ and, together, they form a single smooth curve, as sketched. The λ-lemma implies that $W^{\rm u}(\boldsymbol{\gamma}_3)$ accumulates on $W^{\rm u}(\gamma_1)$. The two-dimensional manifold $W^{\rm s}(\gamma_2)$ is locally a strip bounded by the one-dimensional manifolds $W^{\rm s}(\gamma_3^-)$ and $W^{\rm s}(\gamma_3^+)$, and it extends towards γ_1; here, $W^{\rm s}(\gamma_2)$ accumulates on the two-dimensional manifold $W^{\rm s}(\gamma_1)$, because the strong stable manifold $W^{\rm ss}(\gamma_2) \subset W^{\rm s}(\gamma_2)$ quasi-transversely intersects the one-dimensional manifold $W^{\rm u}(\gamma_1)$.

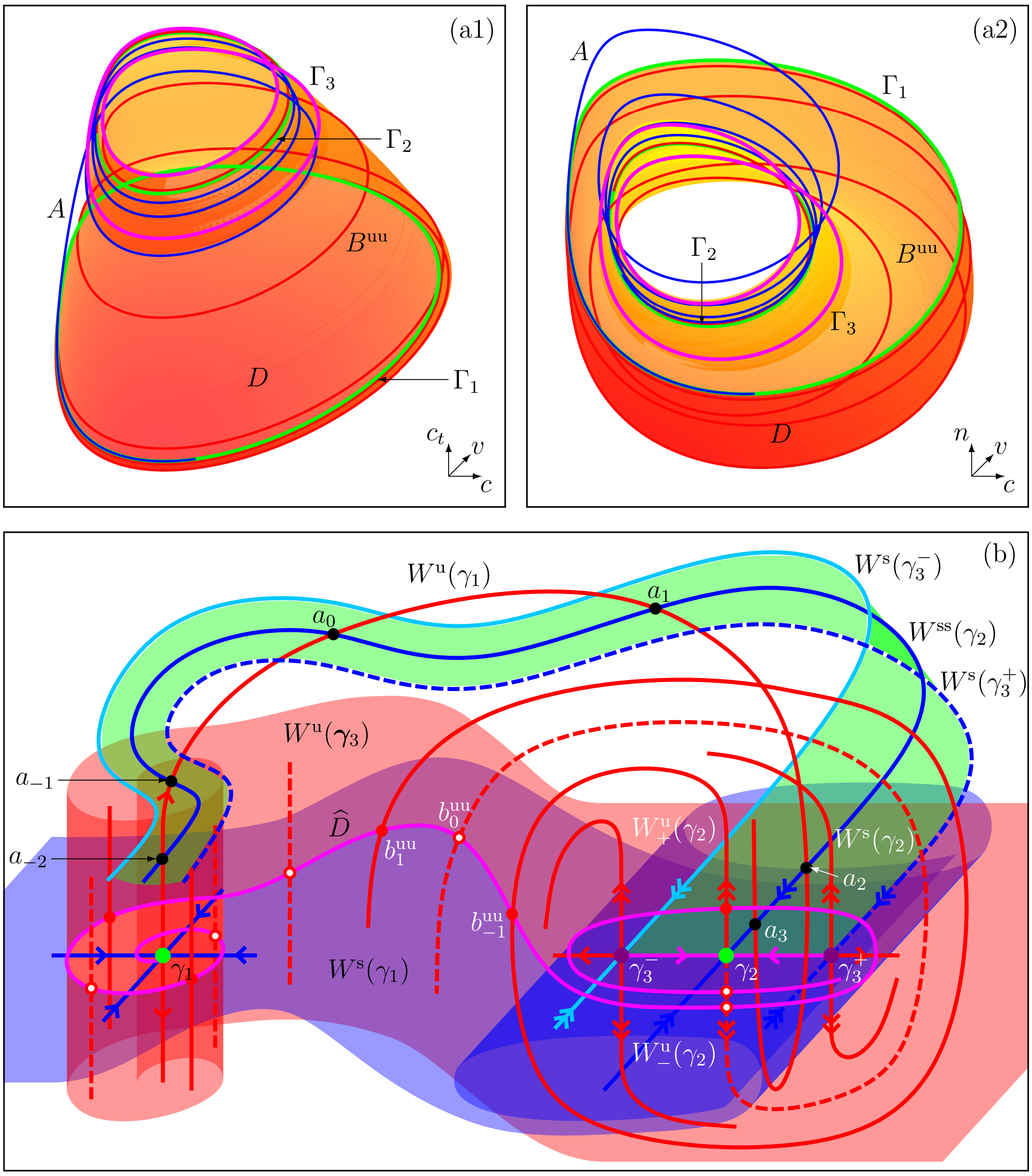

Figure 12: The codimension-one strong heteroclinic cycle $\mathbf{PtoP}^{\mathrm{ss}}$ of system (1) at $(J, s) \approx (3.0158, 8.452)$ in region V , illustrated in the style of Fig. 1. Shown in panels (a1) and (a2) are Γ_1 and Γ_2 (green), Γ_3 (purple), the strong connection $A = W^{\mathrm{u}}(\Gamma_1) \cap W^{\mathrm{ss}}(\Gamma_2)$ (blue), the return connection $B^{\mathrm{uu}} = W^{\mathrm{u}}(\Gamma_2) \cap W^{\mathrm{s}}(\Gamma_1)$, and the surface $D = W^{\mathrm{u}}(\Gamma_3) \cap W^{\mathrm{s}}(\Gamma_1)$ (orange). The sketch at the level of a diffeomorphism shows the corresponding objects γ_1, γ_2 (green dots), the period-two orbit $\boldsymbol{\gamma}_3 = (\gamma_3^-, \gamma_3^+)$ (purple dots), the connecting orbits $(a_k)_{k\in\mathbb{Z}} = W^{\mathrm{u}}(\gamma_1) \cap W^{\mathrm{ss}}(\gamma_2)$ (black dots) and $(b_k^{\mathrm{uu}})_{k\in\mathbb{Z}} = W^{\mathrm{u}}(\gamma_2) \cap W^{\mathrm{s}}(\gamma_1)$ (red dots), the curve $\widehat{D} = W^{\mathrm{u}}(\boldsymbol{\gamma}_3) \cap W^{\mathrm{s}}(\gamma_1)$ (magenta), and the two-dimensional stable manifold $W^{\mathrm{s}}(\gamma_2)$ (green strip), which is bounded by $W^{\mathrm{s}}(\gamma_3^-)$ (cyan curve) and $W^{\mathrm{s}}(\gamma_3^+)$ (dashed blue curve).

Figure 13 provides numerical evidence that the strong heteroclinic cycle along $\mathbf{PtoP}^{\mathrm{ss}}$ is, indeed, as sketched in Fig. 12(b); more specifically, it shows the relevant computed objects in two local Poincaré sections, namely, Σ_1 at $\gamma_1 \in \Gamma_1$ and Σ_2 at $\gamma_2 \in \Gamma_2$. Figure 13(a) shows the locations of Σ_1 and Σ_2 in projection onto (c, v, c_t)-space, and panels (b) and (c) are local phase portraits on Σ_2 and on Σ_1, respectively. Panel (b) shows the situation in Σ_2, which is represented by the coordinates $\alpha^{\mathrm{s}}, \alpha^{\mathrm{ss}}$ and α^{u} along the respective real Floquet vectors γ_2. The strong stable

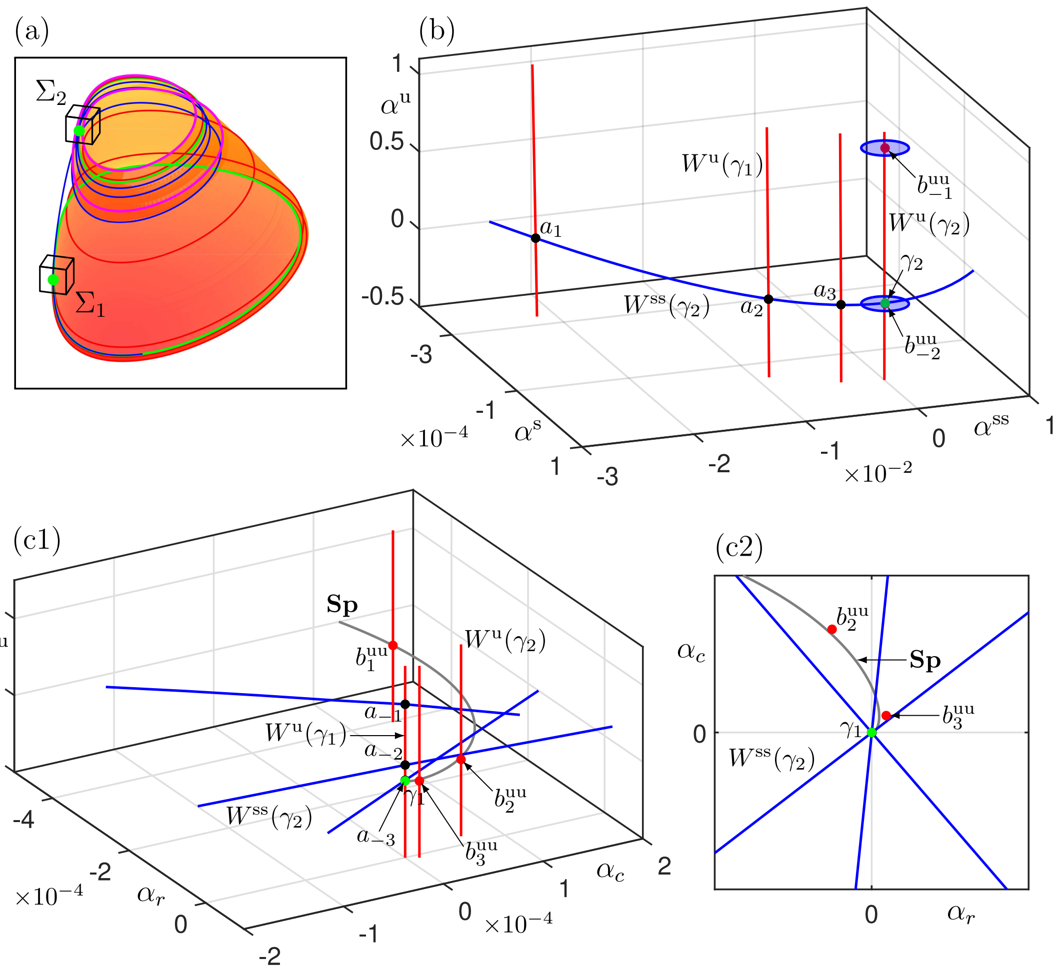

Figure 13: The computed strong heteroclinic cycle $\mathbf{PtoP}^{\mathrm{ss}}$ from Fig. 12 shown in Poincaré sections Σ_1 at $\gamma_1 \in \Gamma_1$ and Σ_2 at $\gamma_2 \in \Gamma_2$ as indicated in panel (a). Panel (b) shows the phase portrait in local $(\alpha^{\mathrm{ss}}, \alpha^{\mathrm{s}}, \alpha^{\mathrm{u}})$-coordinates near γ_2 (green dot) with the connecting orbits (a_k) (black dots) on $W^{\mathrm{ss}}(\gamma_2)$ (blue) and local segments of $W^{\mathrm{u}}(\gamma_1)$ (red), and (b^{uu}_k) (red dots) on $W^{\mathrm{u}}(\gamma_2)$ (red) with local tangent disks of $W^{\mathrm{s}}(\gamma_1)$ (blue). Panel (c1) shows the phase portrait in local $(\alpha_r, \alpha_c, \alpha^{\mathrm{u}})$-coordinates near γ_1 (green dot) with (a_k) (black dots) on $W^{\mathrm{u}}(\gamma_1)$ (red) with local segments of $W^{\mathrm{ss}}(\gamma_2)$ (blue), and (b^{uu}_k) (red dots) on local segments of $W^{\mathrm{u}}(\gamma_2)$ (red) and near the spiral **Sp** (gray). The α^{u}-coordinate has been rescaled so that the points b_{-1} in panel (b) and a_{-1} in panel (c1) are at $\alpha^{\mathrm{u}} = 1$; panel (c2) is the orthogonal projection of panel (c1) onto the (α_r, α_c)-plane.

manifold $W^{\mathrm{ss}}(\gamma_2) = W^{\mathrm{ss}}(\Gamma_2) \cap \Sigma_2$ is a curve that contains the shown points a_1, a_2 and a_3 of the quasi-transverse connecting orbit; the computed local segments of $W^{\mathrm{u}}(\gamma_1)$ through these points are aligned with, and can be seen to accumulate on $W^{\mathrm{u}}(\gamma_2)$ as (a_k) approaches γ_2. The points b^{uu}_{-1} and b^{uu}_{-2} of the structurally stable connecting orbit lie on the one-dimensional manifold $W^{\mathrm{u}}(\gamma_2)$. To enhance visibility, the coordinate α^{u} has been scaled here so that the point b^{uu}_{-1} is given by $\alpha^{\mathrm{u}} = 1$. We verified that b^{uu}_{-2}, which is very close to γ_2, lies below γ_2; this implies that b^{uu}_{-1} and b^{uu}_{-2} belong to opposite branches of $W^{\mathrm{u}}(\gamma_2)$, as required by the negative sign of λ^{u}_2. The blue disks are approximations of the tangent plane of $W^{\mathrm{s}}(\gamma_1)$ at b^{uu}_{-1} and at b^{uu}_{-2}; the arrows along the outer circle indicate that the Poincaré map is orientation-reversing on the tangent disk at b^{uu}_{-2}.

Figure 13(c1) shows the relevant computed objects in Σ_1, which are represented by coordinates α_r, α_c and α^{u}, as in Fig. 5(b). Figure 13(c2) shows the orthogonal projection of panel (c1) onto the

(α_r, α_c)-plane. In panel (c1), the points a_{-1}, a_{-2} and a_{-3} of the quasi-transverse connecting orbit lie on $W^{\mathrm{u}}(\gamma_1)$; moreover, because of the complex-conjugate stable Floquet multipliers, local segments of $W^{\mathrm{ss}}(\gamma_2)$ through the points a_{-k} are rotated under the inverse of the Poincaré map around $W^{\mathrm{u}}(\gamma_1)$, as is further illustrated in panel (c2). The points $b_1^{\mathrm{uu}}, b_2^{\mathrm{uu}}, b_3^{\mathrm{uu}} \in \Sigma_1$ of the structurally stable connecting orbit B^{uu} lie on the two-dimensional manifold $W^{\mathrm{s}}(\gamma_1)$ (not shown). However, these points practically lie in $E^{\mathrm{s}}(\gamma_1)$, that is, the (α_r, α_c)-plane. Also shown is the logarithmic spiral $\mathbf{Sp}$ through the (α_r, α_c)-component of b_1^{uu}, and we observe in panel (c2) that, indeed, b_2^{uu} and b_3^{uu} lie close to $\mathbf{Sp}$ in projection. Also shown in panel (c1) are local segments of $W^{\mathrm{u}}(\gamma_2)$ through these points, which align with and accumulate on $W^{\mathrm{u}}(\gamma_1)$ as b_k^{uu} converges to γ_1.

4.2 Nearby structurally stable heteroclinic cycle between Γ_1 and Γ_2

Any typical or generic small perturbation of the strong heteroclinic cycle from Fig. 12 breaks the codimension-one strong connection A. Such a perturbation results in a structurally stable heteroclinic cycle between the periodic orbits Γ_1 and Γ_2 of the same index one. For example, Fig. 14 shows the cycle obtained by changing the parameter J, from its value in Fig. 12 by only 10^{-4}. The structurally stable connection B^{uu} remains unaffected, and the difference is that $W^{\mathrm{u}}(\Gamma_1)$ still intersects $W^{\mathrm{s}}(\Gamma_2)$, but it no longer does so along $W^{\mathrm{ss}}(\Gamma_2)$; hence, the single connecting orbit $\widetilde{A} = W^{\mathrm{u}}(\Gamma_1) \cap W^{\mathrm{s}}(\Gamma_2)$ in panels (a1) and (a2) of Fig. 14 is now structurally stable as well. At the scale of these projections, the difference between $\widetilde{A}$ and A is not noticeable; however, in panel (b), the sketch at the level of a diffeomorphism illustrates that $W^{\mathrm{u}}(\Gamma_1)$ now spirals around $W^{\mathrm{ss}}(\Gamma_2)$; the corresponding structurally stable orbit $(\tilde{a}_k)_{k\in\mathbb{Z}}$ is the transverse intersection of the one-dimensional manifold $W^{\mathrm{u}}(\gamma_1)$ and the two-dimensional manifold $W^{\mathrm{s}}(\gamma_2)\backslash W^{\mathrm{ss}}(\gamma_2)$. Locally near γ_2, the λ-lemma still forces $W^{\mathrm{u}}(\gamma_1)$ to accumulate on $W^{\mathrm{u}}(\gamma_2)$, but the connecting orbit $(\tilde{a}_k)_{k\in\mathbb{Z}}$ approaches γ_2 along its weak stable eigendirection under forward iteration.

Figure 15 confirms the sketch in Fig. 14(b) by showing the relevant computed objects in two local Poincaré sections Σ_1 at γ_1 and Σ_2 at γ_2, as indicated in (c, v, c_t)-space in Fig. 15(a). Comparison with Fig. 13 shows that the nature of the structurally stable connecting orbit (b_k^{uu}) remains unchanged near both γ_1 and γ_2. However, Fig. 15(a) confirms that the connecting orbit $(\tilde{a}_k)$ does not approach γ_2 along $W^{\mathrm{ss}}(\gamma_2)$. Indeed, the computed points $\tilde{a}_1$, $\tilde{a}_2$, $\tilde{a}_3$ and $\tilde{a}_4$ in $(\alpha^{\mathrm{s}}, \alpha^{\mathrm{ss}}, \alpha^{\mathrm{u}})$-space lie alternatingly on either side of $W^{\mathrm{ss}}(\gamma_2)$; hence, they approach γ_2 along the weak stable Floquet direction at γ_2, which is represented by the α^{s}-coordinate. Note that the local segments of $W^{\mathrm{u}}(\gamma_1)$ still align with and accumulate on $W^{\mathrm{u}}(\gamma_2)$. Figure 15(c1) shows the situation near γ_1 in $(\alpha_r, \alpha_c, \alpha^{\mathrm{u}})$-space representing Σ_1. Indeed, the computed points b_1, b_2 and b_3 effectively follow the logarithmic spiral $\mathbf{Sp}$ in the (α_r, α_c)-plane. Unfortunately, the computed points $\tilde{a}_{-1}$, $\tilde{a}_{-2}$ and $\tilde{a}_{-3}$ are indistinguishable at the scale of panel (c1), because the unstable Floquet multiplier of Γ_1 is still of order 10^3. However, they can be seen to converge to γ_1 along $W^{\mathrm{u}}(\gamma_1)$ in the much enlarged projection onto the $(\alpha_c, \alpha^{\mathrm{u}})$-plane shown in panel (c2). Figure 15(c3) shows the orthogonal projection of panel (c1) onto the (α_r, α_c)-plane. New here are the segments $S_{-1}, S_{-2}, S_{-3} \subset W^{\mathrm{ss}}(\Gamma_2) \cap \Sigma_1$, which lie outside the limited α^{u}-range shown in panel (c1). As these segments rotate counterclockwise towards γ_1 under backward iteration, they no longer intersect $W^{\mathrm{u}}(\gamma_1)$; compare with Fig. 13(c2).

4.3 The heterodimensional cycle $\mathbf{PP}_1^3$

Suitable perturbations of the structurally stable heteroclinic cycle shown in Fig. 14(b) will move the points of the connecting orbit $(\tilde{a}_k)$ closer to the boundary curves $W^{\mathrm{s}}(\gamma_3^-)$ and $W^{\mathrm{s}}(\gamma_3^+)$ of the two-dimensional manifold $W^{\mathrm{s}}(\gamma_2)$. This implies that $(\tilde{a}_k)$ becomes a codimension-one connecting orbit between γ_1 and the period-two orbit $\boldsymbol{\gamma}_3$ if and when it reaches these boundary curves. Figure 16 shows the heterodimensional cycle $\mathbf{PP}_1^3$ between Γ_1 and the period-doubled orbit Γ_3 at $(J, s) \approx (3.026, 8.341)$ in region V. It comprises the codimension-one connection $C = W^{\mathrm{u}}(\Gamma_1) \cap W^{\mathrm{s}}(\Gamma_3)$

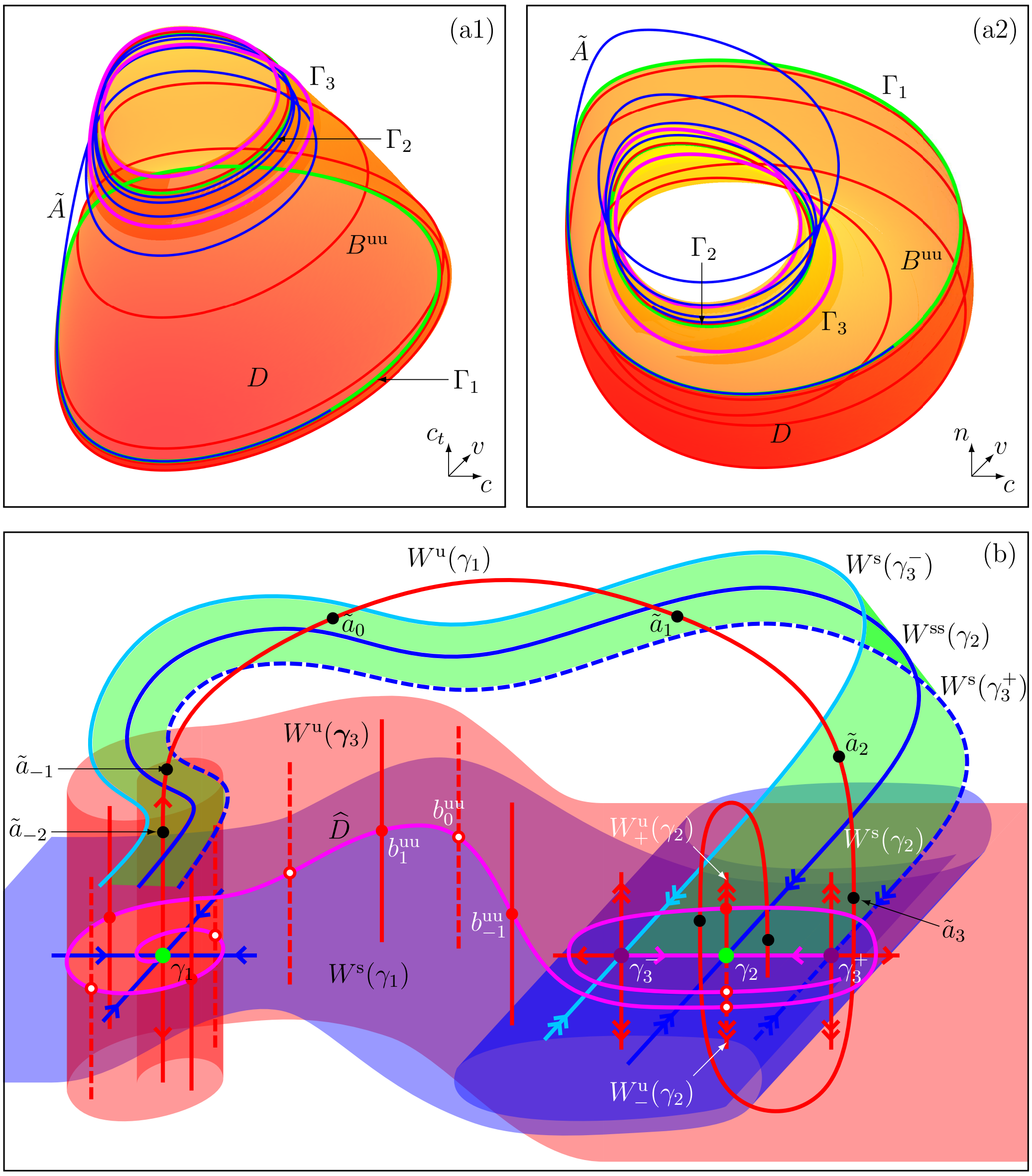

Figure 14: A structurally stable heteroclinic cycle between Γ_1 and Γ_2 of system (1) in region V, illustrated as in Fig. 12; here, $(J, s) \approx (3.0159, 8.452)$. Note the structurally stable connection $\tilde{A} = W^{\mathrm{u}}(\Gamma_1) \cap W^{\mathrm{s}}(\Gamma_2)$ from Γ_1 to Γ_2 in panels (a1) and (a2), which corresponds to the connecting orbit $(\tilde{a}_k)_{k\in\mathbb{Z}}$ in the sketch in panel (b).

and the structurally stable return surface $D = W^{\mathrm{u}}(\Gamma_3) \cap W^{\mathrm{s}}(\Gamma_1)$, shown in panels (a1) and (a2). At the level of a diffeomorphism, the corresponding heterodimensional cycle is formed by the codimension-one connecting orbit $(c_k)_{k\in\mathbb{Z}} = W^{\mathrm{u}}(\gamma_1) \cap W^{\mathrm{s}}(\boldsymbol{\gamma}_3)$ and the structurally stable curve $\widehat{D} = W^{\mathrm{u}}(\Gamma_3) \cap W^{\mathrm{s}}(\Gamma_1)$; compare with Figs. 13 and 15.

Figure 17 presents the computed invariant objects of $\mathbf{PP}_1^3$ in two Poincaré sections Σ_1 and Σ_2, illustrated in panel (a). Panel (b) shows, in local $(\alpha^{\mathrm{s}}, \alpha^{\mathrm{ss}}, \alpha^{\mathrm{u}})$-coordinates of Σ_2, the period-two orbit $\boldsymbol{\gamma}_3 = (\gamma_3^-, \gamma_3^+)$ on both sides of γ_2 and the computed intersection points c_1, c_2, c_3, c_4 and c_5 of C with Σ_2; these points lie on $W^{\mathrm{s}}(\gamma_3^-)$ for even indices and on $W^{\mathrm{s}}(\gamma_3^+)$ for odd indices. Note that the local segments of $W^{\mathrm{u}}(\gamma_1)$ through these points align with and accumulate on $W^{\mathrm{u}}(\gamma_3^-)$ and $W^{\mathrm{u}}(\gamma_3^+)$. Panel (c1) shows phase portraits in Σ_2 in local $(\alpha_r, \alpha_c, \alpha^{\mathrm{u}})$-coordinates; here, the coordinate α^{u} is scaled so that c_0 lies at $\alpha^{\mathrm{u}} = 1$. The computed points c_0, c_{-1} and c_{-2} are seen

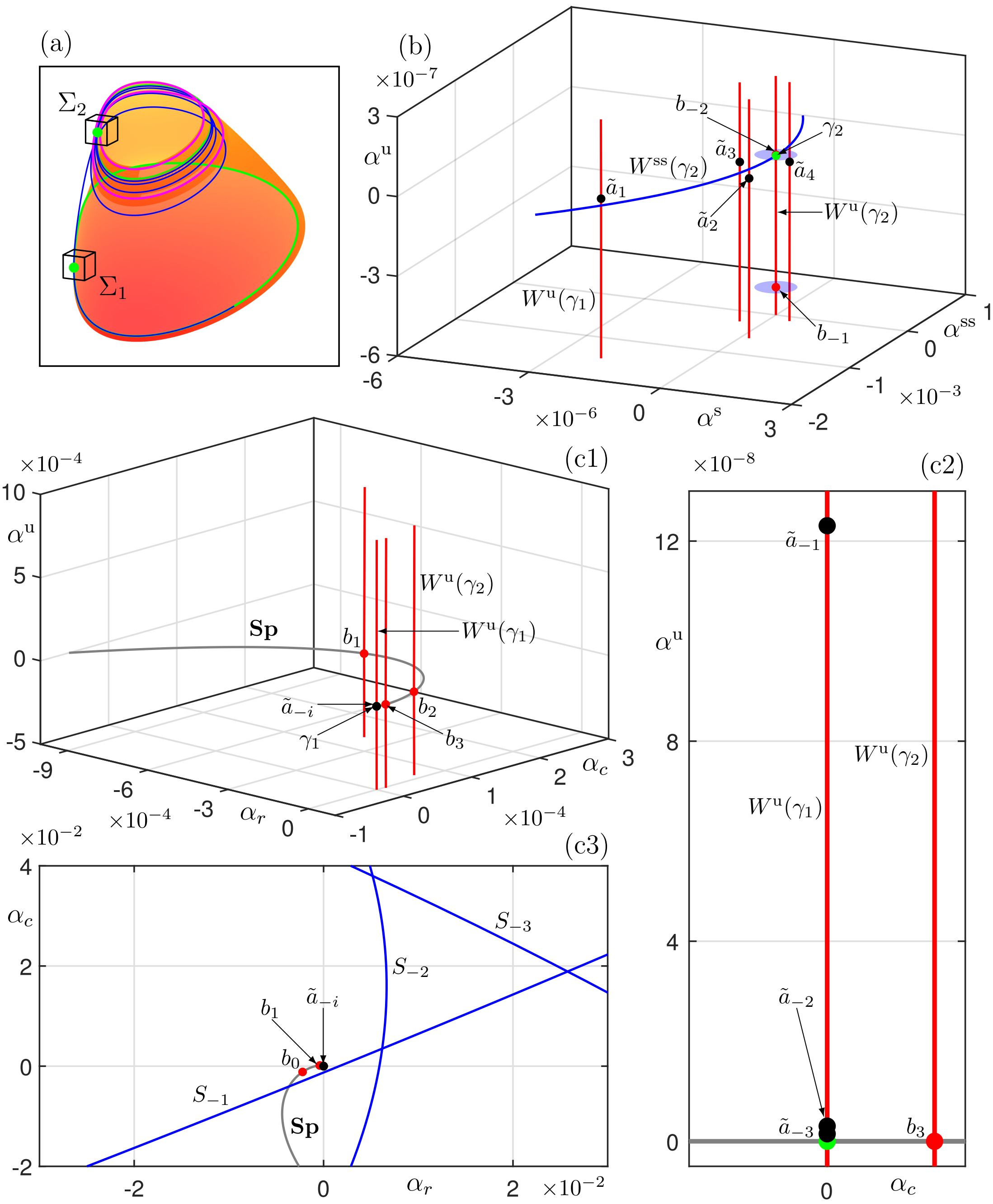

Figure 15: The computed structurally stable heteroclinic cycle from Fig. 14 at the level of the Poincaré maps on local sections Σ_1 at $\gamma_1 \in \Gamma_1$ and Σ_2 at $\gamma_2 \in \Gamma_2$ that are shown in panel (a). The phase portrait near γ_2 is shown in local $(\alpha^{\rm ss}, \alpha^{\rm s}, \alpha^{\rm u})$-coordinates in panel (b), and near γ_1 in local $(\alpha_r, \alpha_c, \alpha^{\rm u})$-coordinates in panels (c1)–(c3). The orthogonal projection of panel (c1) onto the (α_r, α_c)-plane in panel (c2) shows the curves S_{-1}, S_{-2} and S_{-3} (blue), which are local segments of $W^{\rm ss}(\Gamma_2) \cap \Sigma_2$ that exist beyond the $\alpha^{\rm u}$-range of panel (c1). Panel (c3) is a much enlarged orthogonal projection onto the $(\alpha_c, \alpha^{\rm u})$-plane showing how $\tilde{a}_{-1}$, $\tilde{a}_{-2}$ and $\tilde{a}_{-3}$ (black dots) approach γ_1 (green dot). Compare with Fig. 13.

to approach γ_1 along $W^{\rm u}(\gamma_1)$ under backward iteration, while the alternating local segments of $W^{\rm u}(\gamma_3^-)$ and $W^{\rm u}(\gamma_3^+)$ rotate predominantly by the action on their (α_r, α_c)-components; see also the enlargement in panel (c2). Indeed, Fig. 17 confirms the sketch in Fig. 16(b) and shows that

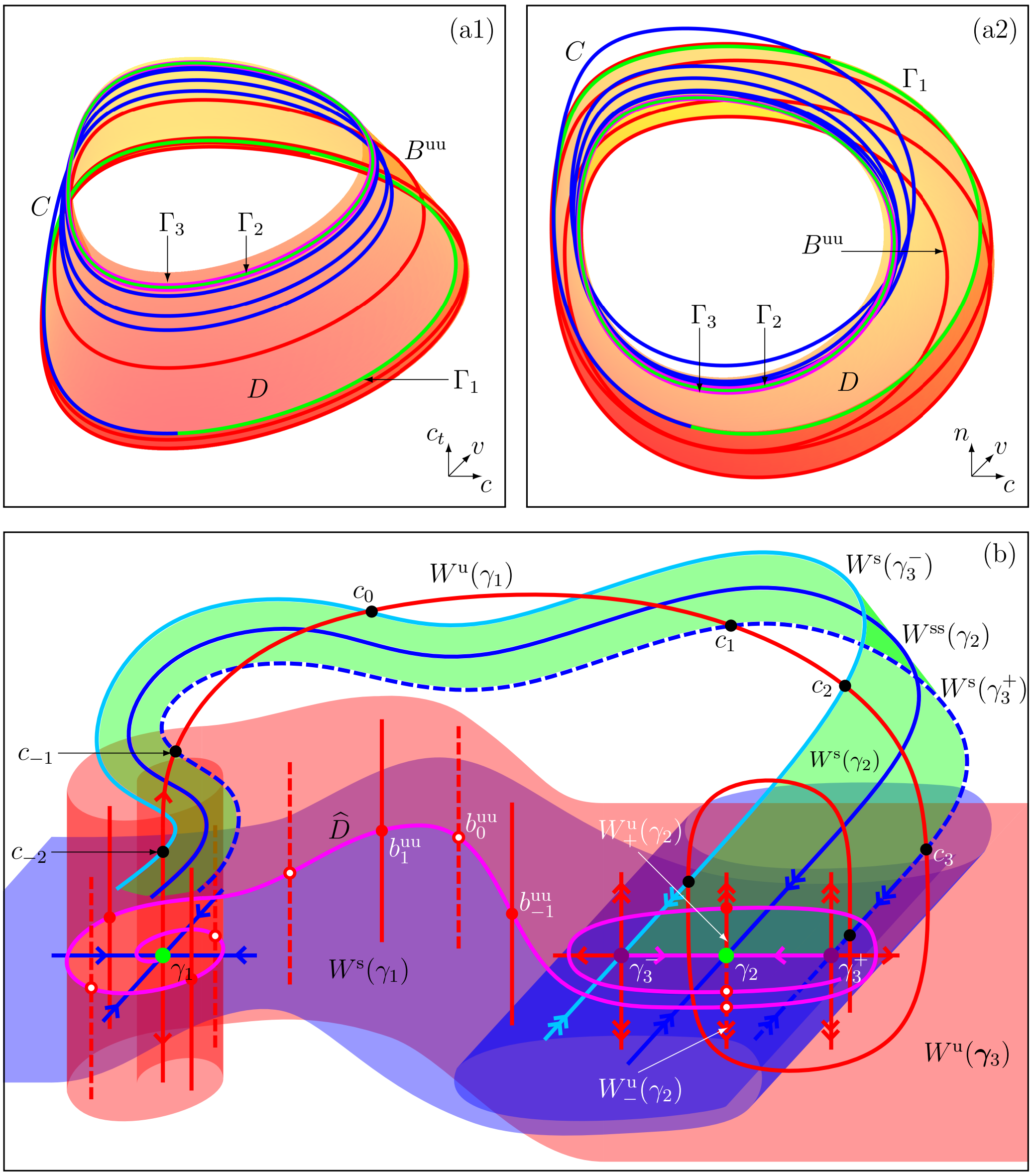

Figure 16: The heterodimensional cycle $\mathbf{PP}_1^3$ of system (1) between Γ_1 (green) and the period-doubled orbit Γ_3 (purple) at $(J, s) \approx (3.026, 8.341)$ in region V, illustrated as in Fig. 12. Shown are the codimension-one connection $C = W^{\mathrm{u}}(\Gamma_1) \cap W^{\mathrm{s}}(\Gamma_3)$ (blue) and the structurally stable surface $D = W^{\mathrm{u}}(\Gamma_3) \cap W^{\mathrm{s}}(\Gamma_1)$ (orange) of return connections in panels (a1) and (a2), which correspond to the connecting orbit $(c_k)_{k \in \mathbb{Z}}$ (black) from γ_1 (green) to $\gamma_3^{\pm}$ (purple) and the curve $\widehat{D}$ (magenta) in the sketch in panel (b).

the connecting orbit (c_k) is the quasi-transverse intersection $W^{\mathrm{u}}(\gamma_1) \cap W^{\mathrm{s}}(\boldsymbol{\gamma}_3)$ resulting from a continuation of $(\tilde{a}_k)$ from Fig. 14(b). Our findings suggest that the locus of the heterodimensional cycle $\mathbf{PP}_1^3$ is a curve that emanates from the codimension-two point **PPD** on the period-doubling curve **PD**, where the curve **PtoP** ends and the curve $\mathbf{PtoP}^{\mathrm{ss}}$ emerges; this will be confirmed and illustrated in Sec. 4.5.

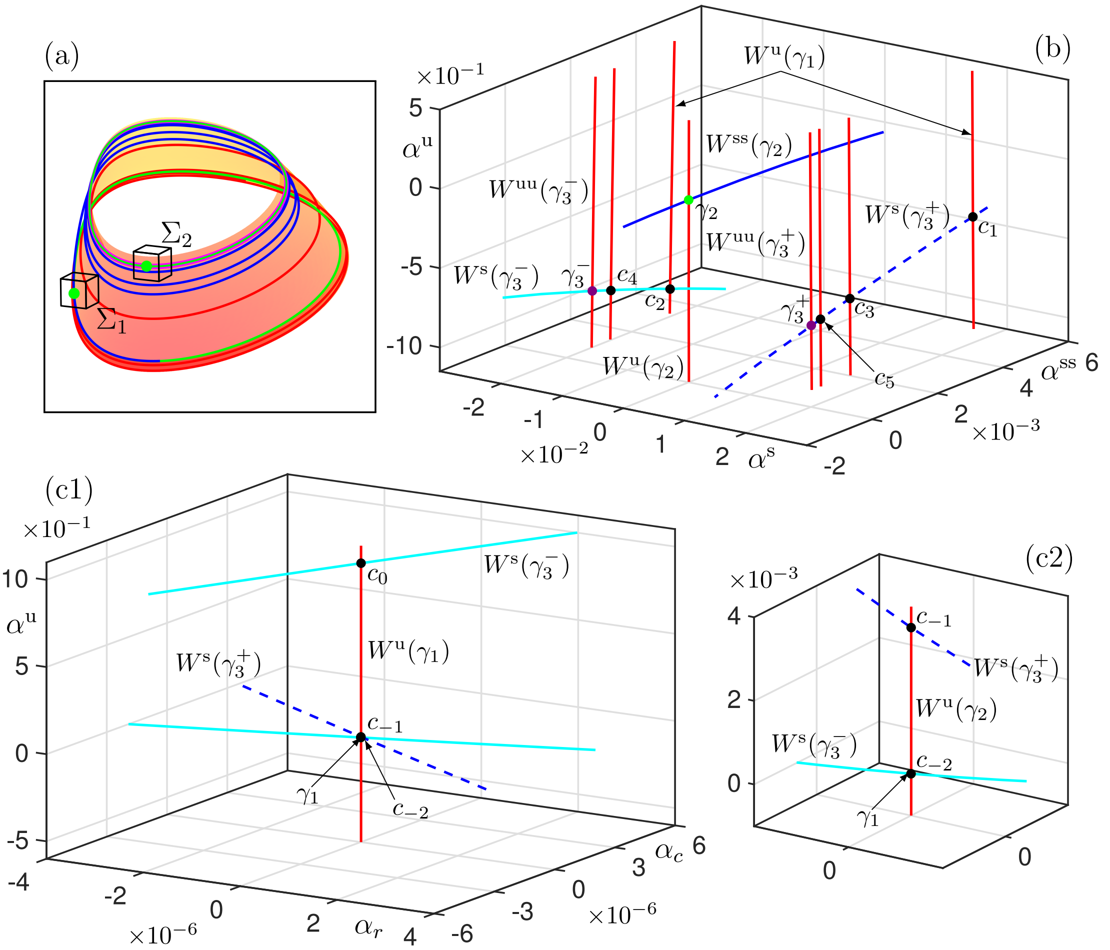

Figure 17: The computed heterodimensional cycle $\mathbf{PP}_1^3$ from Fig. 16 at the level of the Poincaré maps on local sections Σ_1 at $\gamma_1 \in \Gamma_1$ and Σ_2 at $\gamma_2 \in \Gamma_2$, shown in the style of Fig. 13; here, panel (c2) is an enlargement of panel (c1) near γ_1.

4.4 The locus SHC and heterodimensional cycles $\mathbf{PP}_2^3$ and $\overline{\mathbf{PP}}_2^3$

To identify and explain the geometrical properties of heterodimensional cycles between the periodic orbits Γ_2 and Γ_3, which meet at the curve **PD**, we find it convenient to consider perturbations of the codimension-one strong homoclinic orbit **SHC** from Fig. 10. Its locus can be continued, which yields the curve shown in Fig. 18 in the (J, s)-plane from Fig. 3(a). Note that **SHC** emerges from a point on the curve $\mathbf{CC}_2^-$ in region IV and crosses the curve **PD** at the codimension-two point **PDHC**; near this point and to the left of **PD**, the curve **SHC** lies very close to the curves **PtoP** and $\mathbf{PtoP}^{\mathrm{ss}}$, respectively.

In region IV, the strong homoclinic orbit to Γ_2 of **SHC** involves the strong unstable manifold $W^{\mathrm{uu}}(\Gamma_2)$; this is the type of strong homoclinic orbit illustrated in Fig. 10. However, in regions V–VII, the Floquet spectrum of Γ_2 is as shown in Fig. 11, that is, $W^{\mathrm{u}}(\Gamma_2)$ is now two dimensional and $W^{\mathrm{s}}(\Gamma_2)$ has dimension three. Hence, the strong homoclinic orbit involves a return along the two-dimensional strong stable manifold $W^{\mathrm{ss}}(\Gamma_2)$, which is the natural continuation of $W^{\mathrm{s}}(\Gamma_2)$ from region IV. At the level of a diffeomorphism, the one-dimensional manifold $W^{\mathrm{ss}}(\gamma_2)$ lies in the interior of the two-dimensional manifold $W^{\mathrm{s}}(\gamma_2)$, which is a strip bounded by the one-dimensional manifolds $W^{\mathrm{ss}}(\gamma_3^{\pm})$; see Fig. 14(b). Akin to what we have seen for the strong heterodimensional cycle in Secs. 4.1–4.3, near the curve **PD**, the strong heteroclinic cycle $(q_k)_{k\in\mathbb{Z}} = W^{\mathrm{u}}(\gamma_2) \cap W^{\mathrm{ss}}(\gamma_2)$

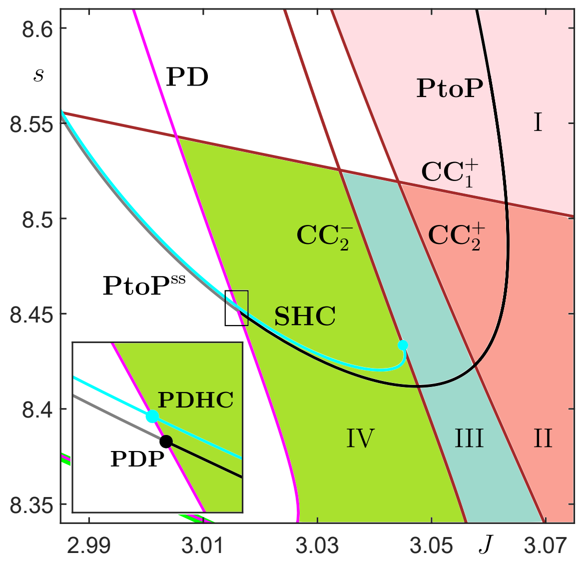

Figure 18: Bifurcation diagram from Fig. 3(a) with the locus **SHC** (cyan curve) of codimension-one strong homoclinic orbits to Γ_2, which starts on the curve $\mathbf{CC}_2^-$ and crosses the curve **PD** at the codimension-two bifurcation point **PDHC** (cyan). Also shown is the locus $\mathbf{PtoP}^{\mathrm{ss}}$ (gray curve) form Fig. 11, and the inset is an enlargement of the black frame near the points **PDHC** and **PDP**.

first perturbs to a structurally stable homoclinic orbit given by $W^{\mathrm{u}}(\gamma_2) \cap W^{\mathrm{s}}(\gamma_2) \setminus W^{\mathrm{ss}}(\gamma_2)$, which exists until the one-dimensional manifold $W^{\mathrm{u}}(\gamma_2)$ reaches the boundary $W^{\mathrm{ss}}(\gamma_3^{\pm})$ of the strip.

For such a specific perturbation, there exists a heterodimensional cycle between Γ_2 and its period-doubled counterpart Γ_3; it is shown in Fig. 19 for the point $(J, s) \approx (3.026, 8.35)$ in region V. The projections in panels (a1) and (a2) illustrate that the periodic orbits Γ_2 and Γ_3 are very close to each other at this parameter point. The codimension-one connecting orbit $E = W^{\mathrm{u}}(\Gamma_2) \cap W^{\mathrm{s}}(\Gamma_3)$ makes a large excursion very close to Γ_1, and the structurally stable return surface $F = W^{\mathrm{u}}(\Gamma_3) \cap W^{\mathrm{s}}(\Gamma_2)$ is a Möbius strip bounded by Γ_3; see also the inset in panel (a1). The sketch in Fig. 19(b) shows the situation at the level of a diffeomorphism: the two branches $W^{\mathrm{u}}_-(\gamma_2)$ and $W^{\mathrm{u}}_+(\gamma_2)$ of $W^{\mathrm{u}}(\gamma_2)$ quasi-transversely intersect $W^{\mathrm{s}}(\gamma_3^-)$ and $W^{\mathrm{s}}(\gamma_3^+)$, respectively, along the connecting orbit $(e_k)_{k\in\mathbb{Z}}$, which includes points e_0, e_1 and e_2 that lie near γ_1. Consequently, the curves $W^{\mathrm{s}}(\gamma_3^{\pm})$ pass near γ_1 but then return to a neighbourhood of γ_2, where further iterates of e_2 accumulate on γ_2; this behaviour of $W^{\mathrm{s}}(\gamma_3^{\pm})$ is illustrated in panel (b) by local segments, which are shown to accumulate on $W^{\mathrm{ss}}(\gamma_2)$. The curve $\widehat{F}$, corresponding to the surface F, is the transverse intersection of the two-dimensional manifolds $W^{\mathrm{u}}(\gamma_3)$ and $W^{\mathrm{s}}(\gamma_2)$. We de-emphasise the one-dimensional manifolds $W^{\mathrm{u}}(\gamma_1)$ and $W^{\mathrm{ss}}(\gamma_2)$ in Fig. 19(b) to avoid confusion, but note that $W^{\mathrm{u}}(\gamma_1)$ still intersects $W^{\mathrm{s}}(\gamma_2)$ transversely, as in Fig. 14(b).

Figure 20 presents the numerical evidence for Fig. 19 by showing the relevant computed objects in sections Σ_1 and Σ_2 illustrated in panel (a); here, Σ_2 is chosen at $\gamma_2 \in \Gamma_2$ as before, and Σ_1 is a section at $\gamma_1 \in \Gamma_1$ that allows us to illustrate the excursion of $\mathbf{PP}_2^3$ to this periodic orbit. Panel (b) shows the time series of the state variable c_t for the connection E; here, time $\tilde{t} = t/T$ has been rescaled by the total integration time T of the computed orbit segment. This time series illustrates how $\mathbf{PP}_2^3$ first oscillates near Γ_2, then transitions to a few oscillations near Γ_1, and finally settles into oscillations near the period-doubled orbit Γ_3; the final part is further illustrated by the enlargement in the inset, where the period-two nature of the oscillations is apparent.

Panels (c1) and (c2) of Fig. 20 are local phase portraits near γ_2 and the period-two points $\gamma_3^{\pm}$ showing computed points of the connecting orbit $(e_k)_{k\in\mathbb{Z}}$. The points e_{-2} and e_{-1} on $W^{\mathrm{u}}(\gamma_2)$ lie below and above γ_2, respectively, and the local segments of $W^{\mathrm{s}}(\gamma_3^-)$ through them align with

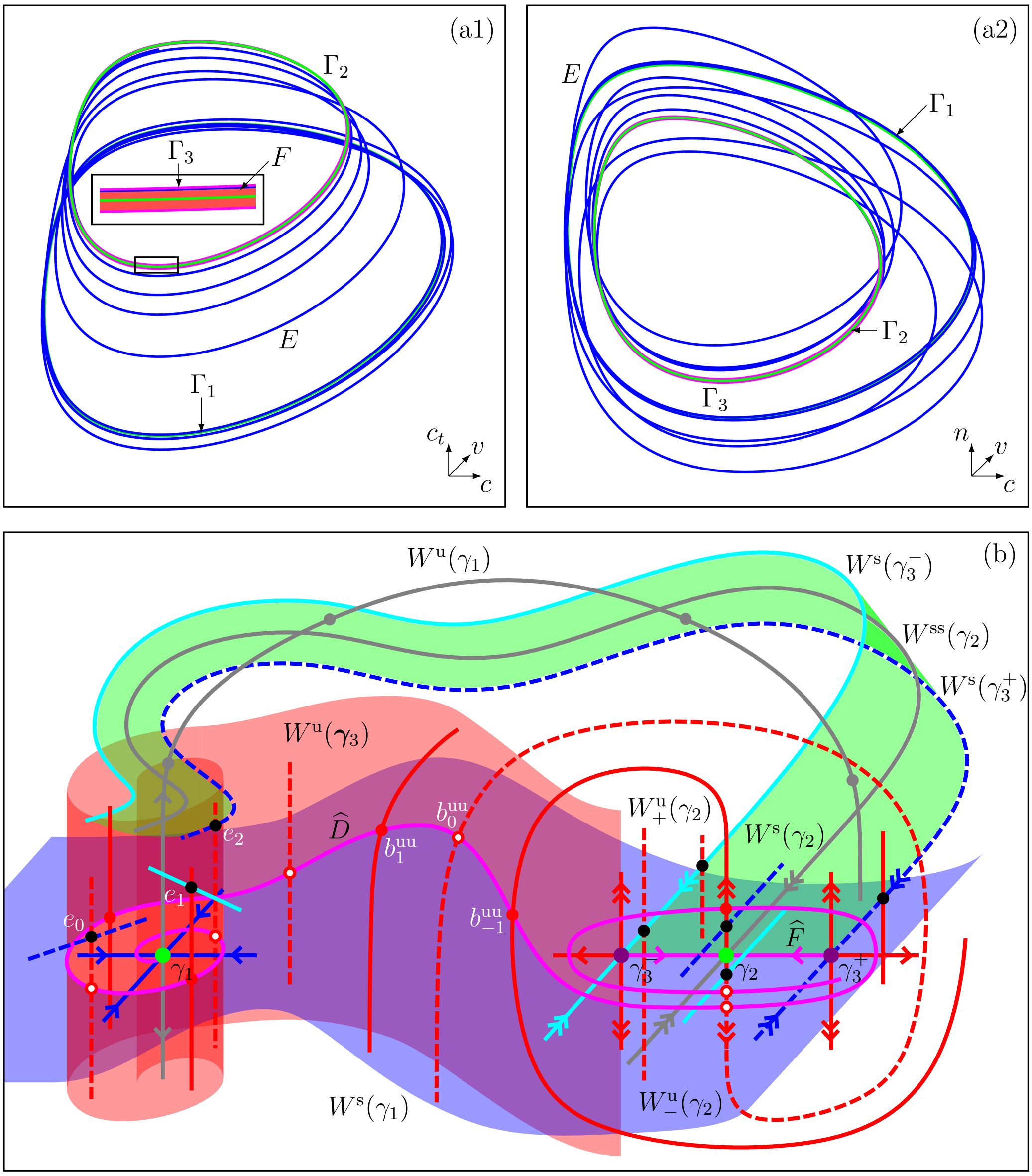

Figure 19: The heterodimensional cycle $\mathbf{PP}_2^3$ of system (1) at $(J, s) \approx (3.026, 8.35)$ in region V, illustrated as in Fig. 12. It consists of the codimension-one connection $E = W^{\mathrm{u}}(\Gamma_2) \cap W^{\mathrm{s}}(\Gamma_3)$ (blue) and the structurally stable surface $F = W^{\mathrm{u}}(\Gamma_3) \cap W^{\mathrm{s}}(\Gamma_2)$ (orange) of return connections in panels (a1) and (a2), which correspond to the connecting orbit $(e_k)_{k \in \mathbb{Z}}$ and the curve $\widehat{F}$ in the sketch in panel (b). The inset in panel (a1) is an enlargement of the black frame. To avoid confusion, the curves $W^{\mathrm{u}}(\gamma_1)$ and $W^{\mathrm{ss}}(\gamma_2)$ are shown in gray in panel (b). Compare with Fig. 12.

$W^{\mathrm{ss}}(\gamma_2^-)$. After an excursion near γ_1, the connecting orbit (e_k) re-enters the shown part of the $(\alpha^{\mathrm{ss}}, \alpha^{\mathrm{s}}, \alpha^{\mathrm{u}})$-space in panel (c1), where the computed points e_4 and e_6 lie on $W^{\mathrm{s}}(\gamma_3^-)$ and e_5 and e_7 lie on $W^{\mathrm{s}}(\gamma_3^+)$. Note that the shown segments of $W^{\mathrm{uu}}(\gamma_2)$ align with $W^{\mathrm{uu}}(\gamma_3^-)$ and $W^{\mathrm{u}}(\gamma_3^+)$. In panel (c2), the orthogonal projection of panel (c1) onto the $(\alpha^{\mathrm{s}}, \alpha^{\mathrm{ss}})$-plane shows how the segments $S_{-3}, S_{-2}, S_{-1} \subset W^{\mathrm{s}}(\gamma_3^{\pm})$ through the points e_{-3}, e_{-2} and e_{-1} 'flip' with respect to the α^{ss}-axis under the Poincaré map.

Panels (d1) and (d2) of Fig. 20 show the computed points e_0, e_1, e_2 and e_3 of the connecting orbit(e_k) near γ_1 in the $(\alpha_r, \alpha_c, \alpha^{\mathrm{u}})$-space of Σ_1. They closely follow the spiral $\mathbf{Sp} \subset E^{\mathrm{s}}(\gamma_1)$ (chosen to contain the (α_r, α_c)-coordinates of e_3) almost to γ_1, but (e_k) does not reach this fixed

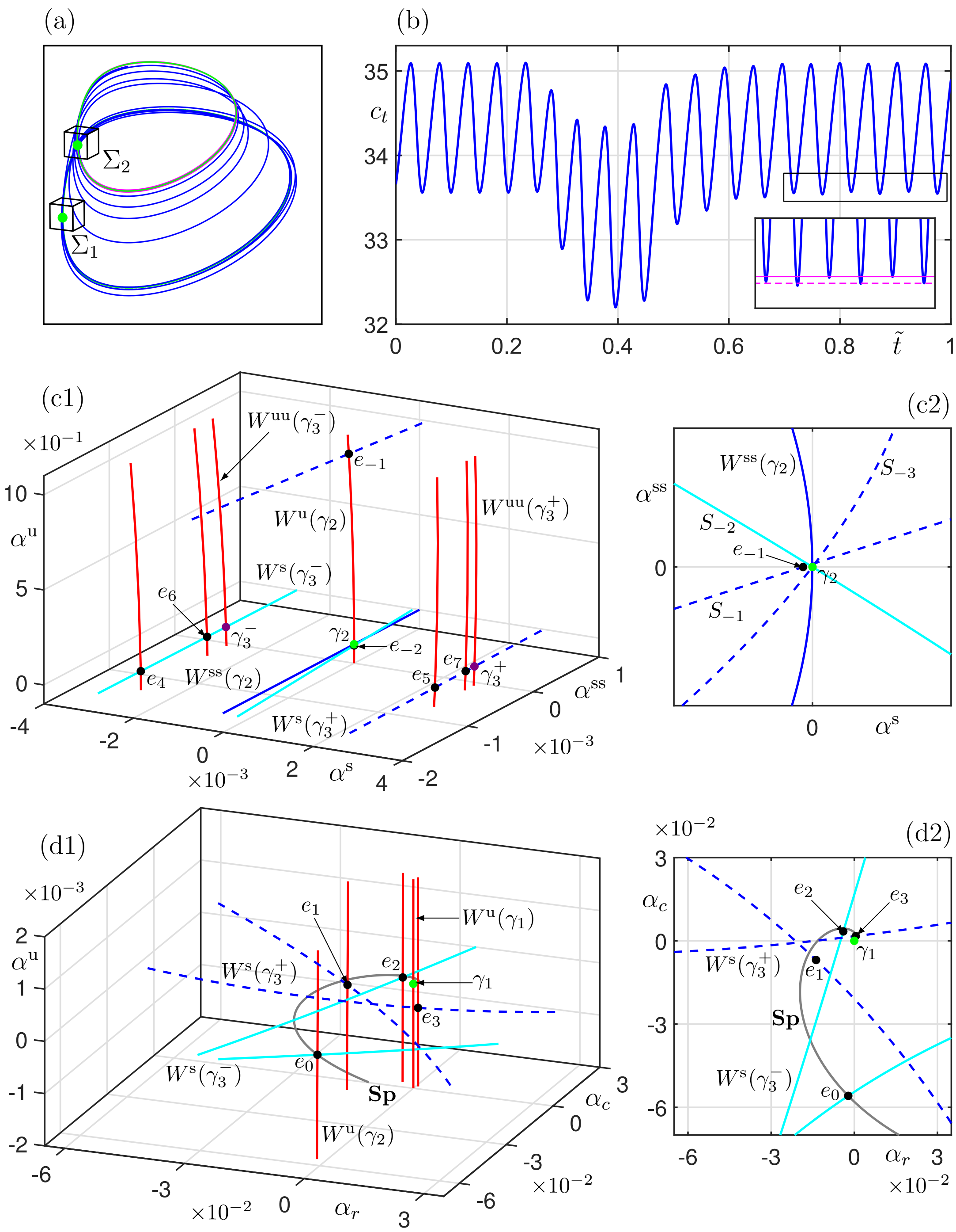

Figure 20: The computed heterodimensional cycle $\mathbf{PP}_2^3$ from Fig. 19. Panel (a) shows it in (c, v, c_t)-space with an indication of local sections Σ_1 at $\gamma_1 \in \Gamma_1$ and Σ_2 at $\gamma_2 \in \Gamma_2$, and panel (b) is the scaled c_t-time trace of the connecting orbit E, where the inset enlarges the black frame. A phase portrait of the Poincaré map is shown in local $(\alpha^{\mathrm{ss}}, \alpha^{\mathrm{s}}, \alpha^{\mathrm{u}})$-coordinates of Σ_2 in panel (c1) and (c2), and in local $(\alpha_r, \alpha_c, \alpha^{\mathrm{u}})$-coordinates of Σ_1 in panels (d1)–(d3).

point. Nevertheless, the shown local segments of $W^{\mathrm{u}}(\gamma_2)$ still align with $W^{\mathrm{u}}(\gamma_1)$. The situated illustrated in panel (d1) is confirmation that the connection E shown in Fig. 19 is, indeed, a suitable perturbation of the strong homoclinic orbit **SHC** shown in Fig. 10. In panel (d2), the orthogonal projection of panel (d1) onto the (α_r, α_c)-plane illustrates the clockwise rotation of the

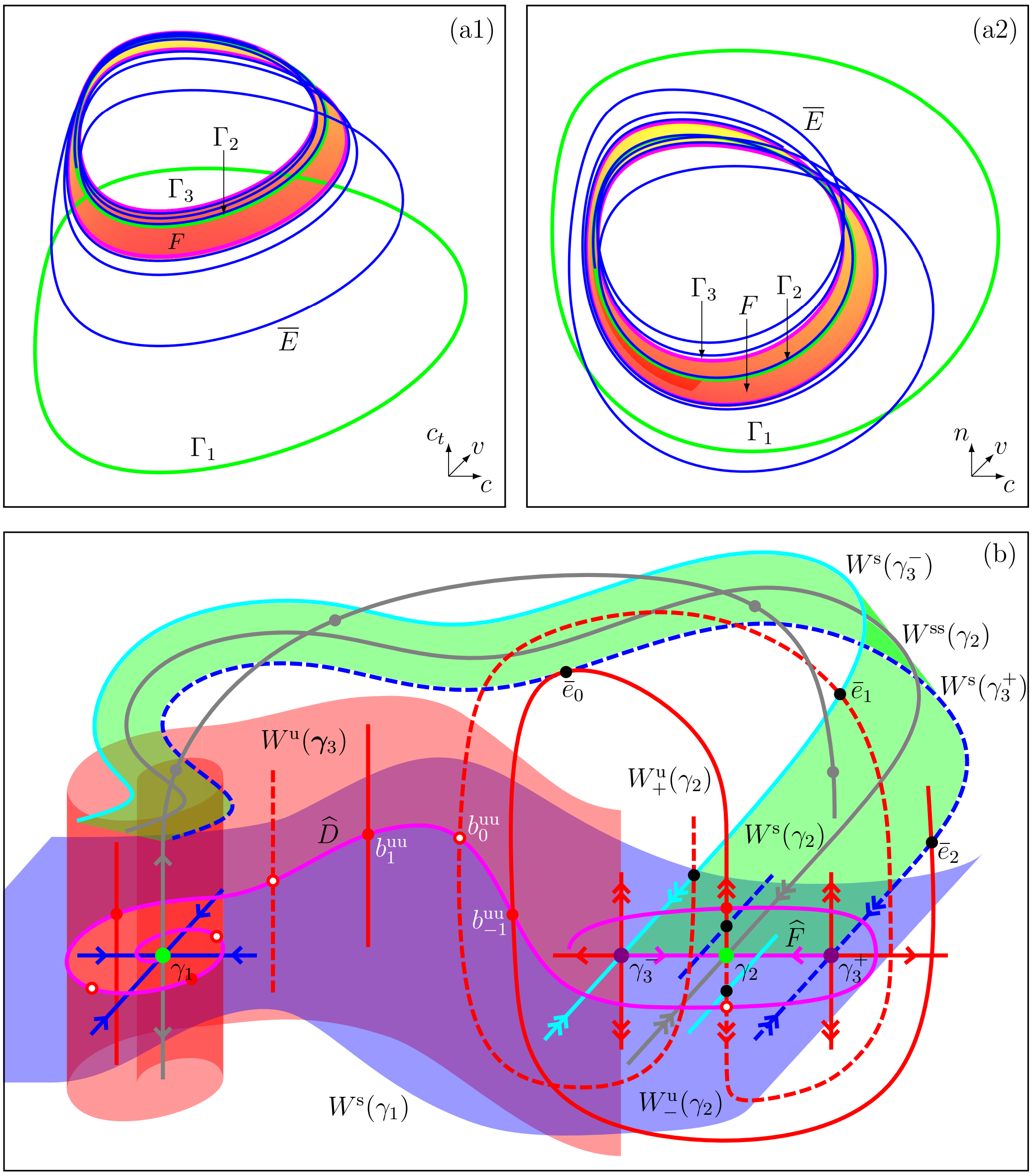

Figure 21: The heterodimensional cycle $\overline{\mathbf{PP}}_2^3$ of system (1) at $(J,s) \approx (3.021, 8.4)$ in region V, illustrated as in Fig. 12. It consists of the codimension-one connection $\overline{E} = W^{\rm u}(\Gamma_2) \cap W^{\rm s}(\Gamma_3)$ (blue) and the structurally stable return surface F (orange) from Fig. 19 in panels (a1) and (a2), which correspond to the connecting orbit $(\bar{e}_k)_{k\in\mathbb{Z}}$ and the curve $\widehat{F}$ in the sketch in panel (b). Compare with Fig. 19.

local segments of $W^{\rm s}(\gamma_3^{\pm})$ under the Poincaré map.

In region V, we also discovered a different heterodimensional cycle between Γ_2 and Γ_3, namely, one with a codimension-one connecting orbit that does not come close to Γ_1. We refer to it as $\overline{\mathbf{PP}}_2^3$, and it is shown for the point $(J,s) \approx (3.021, 8.4)$ in Fig. 21. The surface F of structurally stable connecting orbits in panels (a1) and (a2) is actually the continuation of the Möbius strip bounded by Γ_3 from Fig. 19. Observe that the codimension-one connecting orbit $\overline{E}$ from Γ_2 to Γ_3 does not visit a neighbourhood of Γ_1. Figure 21(b) emphasises the more local nature of $\overline{\mathbf{PP}}_2^3$ at the level of a diffeomorphism and, here, the codimension-one connecting orbit $(\bar{e}_k) = W^{\rm u}(\gamma_2) \cap W^{\rm s}(\gamma_3^{\pm})$ stays well away from γ_1. Otherwise, this sketch is as that in Fig. 19(b) for $\mathbf{PP}_2^3$.

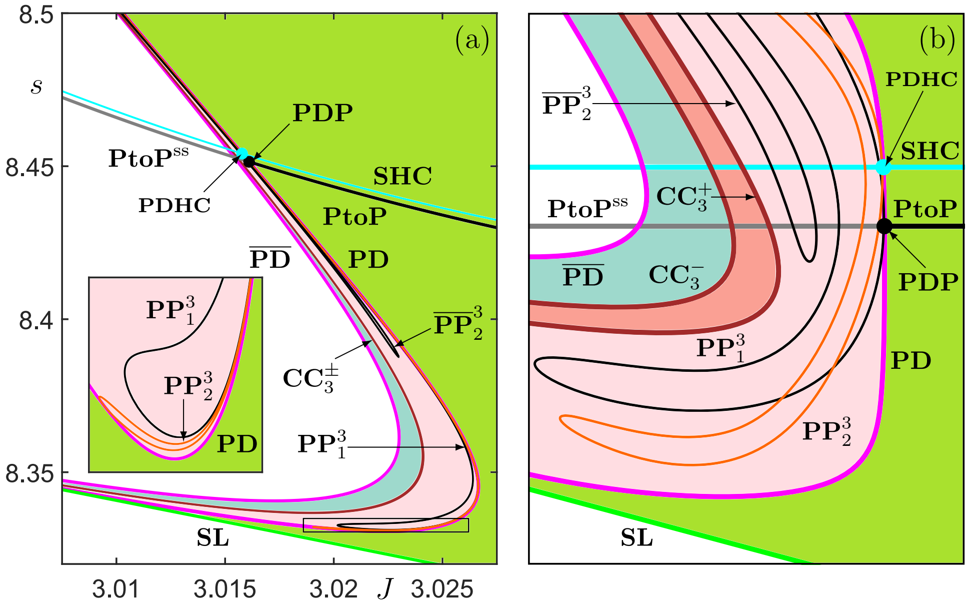

Figure 22: The bifurcation loci and subregions from Figs. 11 and 18 shown over a larger range of the (J, s)-plane with the loci $\mathbf{PP}_1^3$ (black), $\mathbf{PP}_2^3$ (orange) and $\overline{\mathbf{PP}}_2^3$ (black). The inset in panel (a) enlarges the black frame, and panel (b) is a topological sketch of panel (a).

4.5 Loci of heterodimensional cycles involving Γ_3

The loci of the heterodimensional cycles $\mathbf{PP}_1^3, \mathbf{PP}_2^3$ and $\overline{\mathbf{PP}}_2^3$ can be found as curves in the (J, s)-plane by continuation of their respective codimension-one connections, starting from the parameter points used for $\mathbf{PP}_1^3$ in Fig. 17, $\mathbf{PP}_2^3$ in Fig. 16, and $\overline{\mathbf{PP}}_2^3$ in Fig. 21, respectively. Figure 22 shows the resulting curves together with the bifurcation loci and Floquet regions from Figs. 11 and 18. Here, panel (a) of Fig. 22 presents the computed curves in a larger region of the (J, s)-plane, and panel (b) is a topological sketch that clarifies their relative positions.

As we already mentioned, the curve $\mathbf{PP}_1^3$ is tangent to the curve **PD** at the codimension-two point **PDP**, at which the curve **PtoP** joins the curve **PtoP**$^{\mathrm{ss}}$. When this codimension-two point is approached along $\mathbf{PP}_1^3$, the codimension-one connection C from Fig. 16 becomes, precisely at **PDP**, the codimension-one connection A of **PtoP** and **PtoP**$^{\mathrm{ss}}$ from Figs. 8 and 12, respectively. When continued from **PDP** in the direction of increasing s, the curve $\mathbf{PP}_1^3$ closely follows **PD** and leaves the shown part of the (J, s)-plane in Fig. 22. When continued from **PDP** in the opposite direction, the curve $\mathbf{PP}_1^3$ initially again closely follows **PD**, but then turns around, crosses the curve **PtoP**$^{\mathrm{ss}}$ and finally, follows the other branch of $\mathbf{PP}_1^3$, as it leaves the shown (J, s)-region; see also the inset in Fig. 22(a).

Similarly, the curve $\mathbf{PP}_2^3$ is tangent to **PD** at the codimension-two point **PDHC**, at which the curve **SHC** meets **PD**. When this codimension-two point is approached along $\mathbf{PP}_2^3$, the codimension-one connection E from Fig. 19 becomes the strong homoclinic orbit **SHC** from Fig. 10 precisely at **PDHC**. When continued from **PDHC** in either direction, the curve $\mathbf{PP}_2^3$ also leaves the shown region of the (J, s)-plane in Fig. 22 in the direction of increasing s. Similar to the curve $\mathbf{PP}_1^3$, the curve $\mathbf{PP}_2^3$ sharply turns around in the region enlarged in the inset and subsequently crosses the curve **PtoP**$^{\mathrm{ss}}$. The curve $\overline{\mathbf{PP}}_2^3$, on the other hand, does not bifurcate from a locus of strong homoclinic orbits. Instead, it enters the shown (J, s)-region from the top in the direction of decreasing s, crosses the curve **PtoP**$^{\mathrm{ss}}$, turns around, crosses **PtoP**$^{\mathrm{ss}}$ again, and then leaves the shown region of the (J, s)-plane in the direction of increasing s.

Further support for the sketch in Fig. 22(b) is provided in Fig. 23, where we show the computed

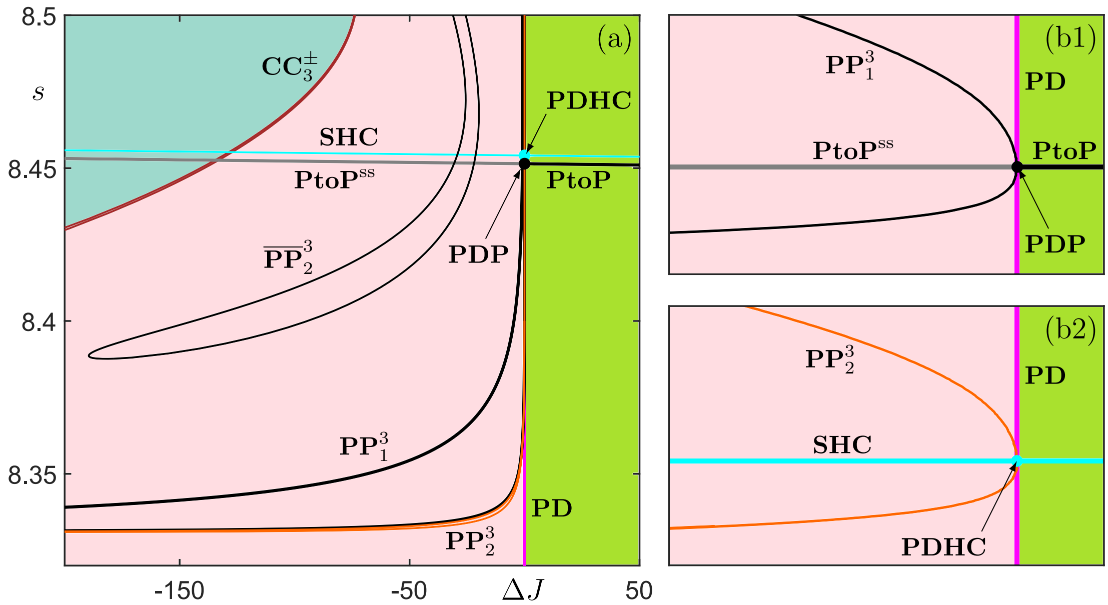

Figure 23: Bifurcation loci from Fig. 22, shown near **PDP** and **PDHC** in terms of the rescaled coordinate ΔJ, which measures the difference in the J-coordinate from the curve **PD**. Panels (b1) and (b2) are extreme enlargements of panel (a) near the codimension-two bifurcation points **PDP** and **PDHC**, respectively.

loci relative to the curve **PD**. More specifically, for any given parameter point (J, s), we define

$$\Delta J = \beta(J - J_{\mathbf{PD}}(s)),$$

where $J_{\mathbf{PD}}(s)$ is the rightmost point on **PD** (which exists for s above the s-minimum of **PD**); hence, the vertical line at $\Delta J = 0$ in Fig. 23 corresponds to **PD**. In panel (a), the scaling factor β is set to 2.797×10^6; even for this considerable enlargement, the curves $\mathbf{PP}_1^3$ and $\mathbf{PP}_2^3$ are still very close to **PD** for $s \in [8.37, 8.5]$. However, further enlargements in Fig. 23(b1) and (b2), respectively, demonstrate that $\mathbf{PP}_1^3$ has a quadratic tangency with **PD** at **PDP**, and that $\mathbf{PP}_2^3$ has a quadratic tangency with **PD** at **PDHC**. In Fig. 22(b), notice that the curves $\mathbf{PP}_1^3$ and $\mathbf{PP}_2^3$ cross each other a number of times, while the curve $\overline{\mathbf{PP}}_2^3$ neither intersects $\mathbf{PP}_1^3$ nor $\mathbf{PP}_2^3$.

5 Cascading heterodimensional cycles

The three curves $\mathbf{PP}_1^3$, $\mathbf{PP}_2^3$ and $\overline{\mathbf{PP}}_2^3$ shown in Figs. 22(a) and 23(a) all remain inside region V of the shown (J, s)-region. In fact, $\mathbf{PP}_1^3$ and $\mathbf{PP}_2^3$ stay close to the curve **PD** for even greater values of s. However, the curve $\overline{\mathbf{PP}}_2^3$ moves from region V through region VI to region VII and ends at two different points on the curve $\overline{\mathbf{PD}}$ shown in Fig. 22. Recall that the two positive unstable Floquet multipliers of Γ_3 in region V become a complex-conjugate pair in region VI, and then real but negative in region VII. Since this transition only affects the structurally stable surface F, shown in panels (a1) and (a2) of Fig. 21, the curve $\overline{\mathbf{PP}}_2^3$ can end on the period-doubling locus $\overline{\mathbf{PD}}$ of Γ_3.

We found that, near $\overline{\mathbf{PD}}$, the heterodimensional cycle $\overline{\mathbf{PP}}_2^3$ undergoes the same transition discussed in Sec. 3 for the primary heterodimensional cycle **PtoP**. This is illustrated in Fig. 24. Panel (a1) is an overall view of the (J, s)-region $[2.91, 3.1] \times [8.3, 9.5]$ showing the curve $\overline{\mathbf{PP}}_2^3$ in relation to the relevant bifurcation curves from Figs. 2 and 22. The two endpoints of $\overline{\mathbf{PP}}_2^3$ on $\overline{\mathbf{PD}}$ are inside the frame, which is enlarged in Fig. 24(a2). As is the case for the curve **PtoP** of primary

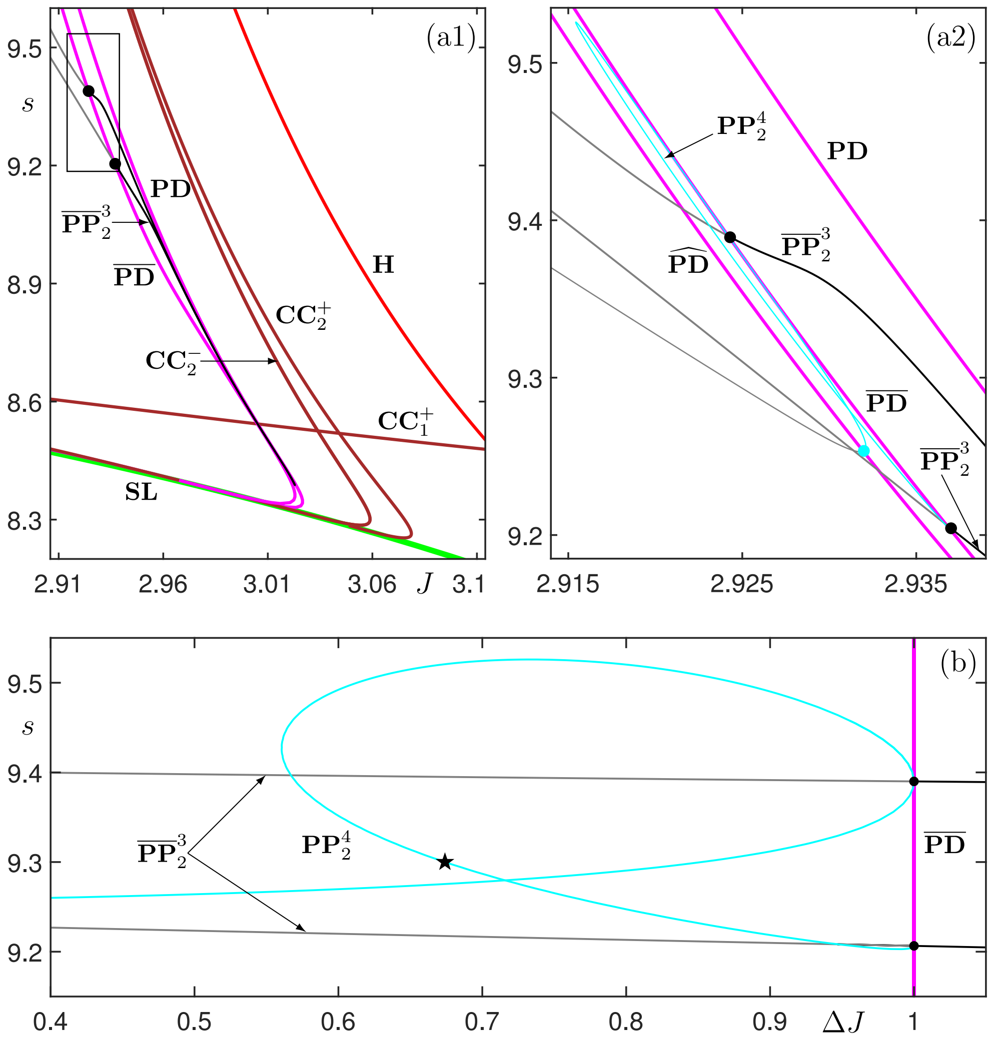

Figure 24: Bifurcation diagram in the (J, s)-plane of system (1) with the bifurcation curves from Fig. 2 with $\overline{\mathbf{PD}}$, $\widehat{\mathbf{PD}}$ (magenta), $\overline{\mathbf{PP}}_2^3$ (black, and grey when a strong heteroclinic cycle past $\overline{\mathbf{PD}}$) and $\mathbf{PP}_2^4$ (cyan). Panel (a1) shows a large (J, s)-region, and panel (a2) enlarges the black frame. Panel (b) shows the region between $\overline{\mathbf{PD}}$ and $\widehat{\mathbf{PD}}$ in terms of the rescaled parameter ΔJ where $\overline{\mathbf{PD}}$ lies at $\Delta J = 1$ and $\widehat{\mathbf{PD}}$ at $\Delta J = 0$ (not shown); the black star at $(J, s) \approx (2.929, 9.3)$ is the parameter point of Fig. 25.

heteroclinic cycles, the curve $\overline{\mathbf{PP}}_2^3$ can be continued past $\overline{\mathbf{PD}}$ as a strong heteroclinic cycle between Γ_2 and Γ_3 along the two gray segments (not labelled). More specifically, the codimension-one connection $\overline{E}$ of $\overline{\mathbf{PP}}_2^3$ persists as the codimension-one strong connection $W^{\mathrm{u}}(\Gamma_2) \cap W^{\mathrm{ss}}(\Gamma_3)$.

5.1 The heterodimensional cycle $\mathbf{PP}_2^4$

Figure 24(a2) also shows the locus $\overline{\mathbf{PP}}_2^4$ of the primary heterodimensional cycle between Γ_2 and the periodic orbit Γ_4 that emanates from $\overline{\mathbf{PD}}$. The curve $\mathbf{PP}_2^4$ meets $\overline{\mathbf{PD}}$ in a tangent fashion at both of the codimension-two points on $\overline{\mathbf{PP}}_2^3$. Moreover, $\mathbf{PP}_2^4$ ends on the period-doubling locus $\widehat{\mathbf{PD}}$ of Γ_4, beyond which it can also be continued as a strong heteroclinic cycle between Γ_2 and Γ_4. Figure 24(b) shows the region to the left of $\overline{\mathbf{PD}}$ near the two crossing points of $\overline{\mathbf{PP}}_2^3$. Here, we plot $\mathbf{PP}_2^4$ in terms of its relative J-distance ΔJ from $\overline{\mathbf{PD}}$ and $\widehat{\mathbf{PD}}$, which is scaled so that these

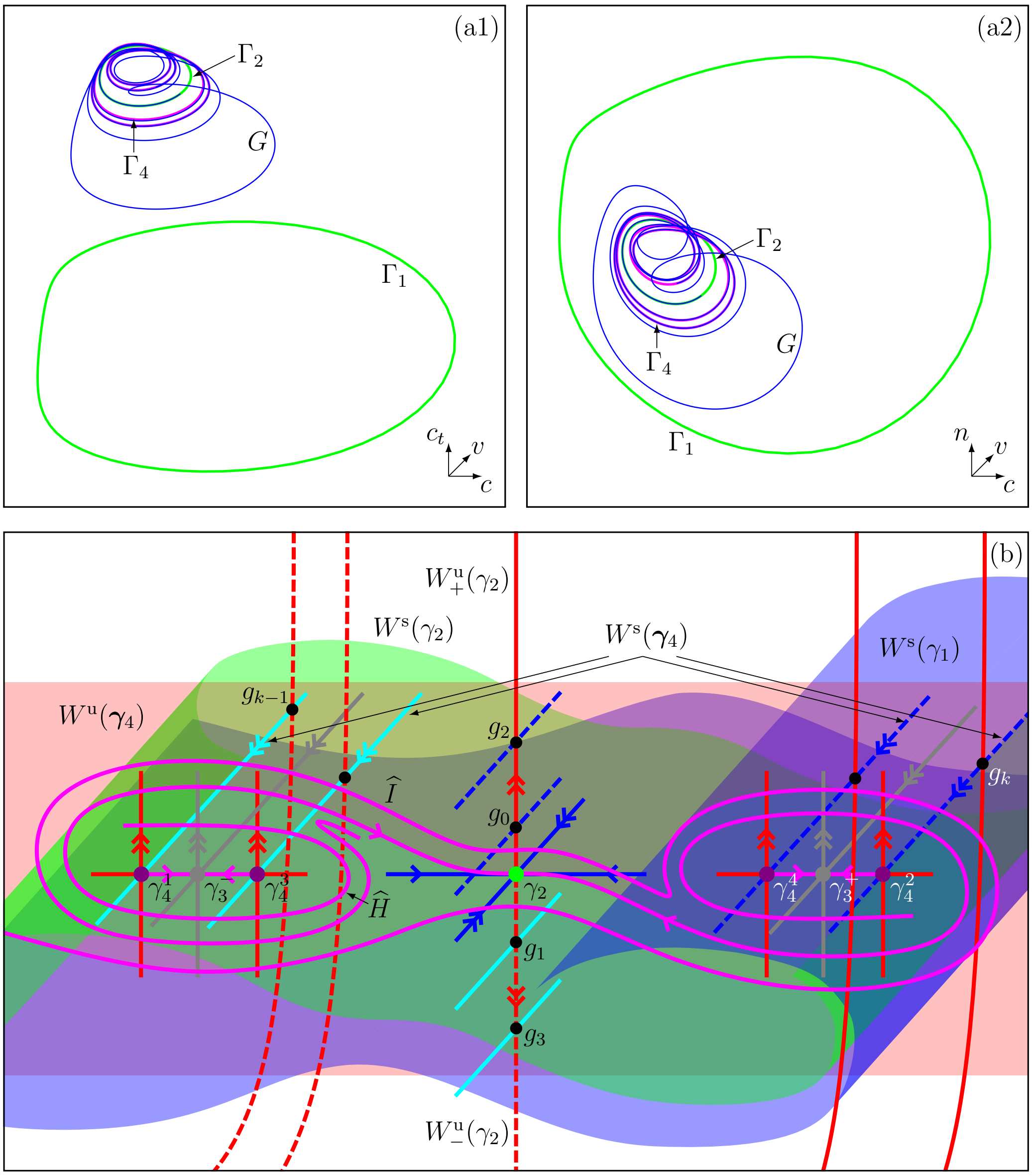

Figure 25: The heterodimensional cycle $\mathbf{PP}_2^4$ of system (1) at $(J, s) \approx (2.929, 9.3)$. It consists of the codimension-one connection $G = W^{\mathrm{u}}(\Gamma_2) \cap W^{\mathrm{s}}(\Gamma_4)$ (blue) and the structurally stable return surface $H = W^{\mathrm{u}}(\Gamma_4) \cap W^{\mathrm{s}}(\Gamma_2)$ (not shown) in panels (a1) and (a2), which correspond to the connecting orbit $(g_k)_{k\in\mathbb{Z}}$ and the curve $\widehat{H}$ in the sketch near $\boldsymbol{\gamma}_4 = (\gamma_4^1, \gamma_4^2, \gamma_4^3, \gamma_4^4)$ (purple dots) in panel (b). Compare with Fig. 21.

two curves are at $\Delta J = 1$ and $\Delta J = 0$, respectively. The shown segment of $\mathbf{PP}_2^4$ was continued from the lower crossing point in the direction of decreasing s. It starts tangentially to $\overline{\mathbf{PD}}$, makes a single loop that is also tangent to $\overline{\mathbf{PD}}$ at the upper crossing point, leaves the shown $(\Delta J, s)$-region in the direction of decreasing J, and finally ends on $\widehat{\mathbf{PD}}$; see also panel (a2). We remark that the curves $\mathbf{PD}$, $\overline{\mathbf{PD}}$ and $\widehat{\mathbf{PD}}$ are part of a period-doubling cascade. Hence, Fig. 24 suggests that there could exist an associated cascade of heterodimensional cycles involving $\mathbf{PP}_2^3$, $\mathbf{PP}_2^4$ and so on.

Figure 25 shows the heterodimensional cycle $\mathbf{PP}_2^4$ at the point $(J, s) \approx (2.929, 9.3)$, which is indicated by the black star in Fig. 24(b); the Floquet multipliers of Γ_2 and Γ_4 at this parameter point are given in Table 4. The two projections in panels (a1) and (a2) show the codimension-one connection G, which is the quasi-transverse intersection of the two-dimensional manifolds $W^{\mathrm{u}}(\Gamma_2)$

Γ_2		Γ_4	
stable :	$\begin{cases} \lambda_2^{ss} \approx \ \ 3.401 \times 10^{-1} \\ \lambda_2^{s} \approx -6.899 \times 10^{-1} \end{cases}$	unstable :	$\begin{cases} \lambda_4^{u} \approx 2.482 \times 10^{0} \\ \lambda_4^{uu} \approx 1.672 \times 10^{13} \end{cases}$
unstable :	$\lambda_2^{u} \approx -4.367 \times 10^{3}$	stable :	$\lambda_4^{s} \approx 2.110 \times 10^{-2}$

Table 4: Floquet multipliers of Γ_2 and Γ_4 at parameter point $(J, s) \approx (2.929, 9.3)$ of Fig. 25 on the curve $\mathbf{PP}_2^4$.

and $W^s(\Gamma_4)$. Notably, G becomes the codimension-one connection $\overline{E}$ from Fig. 21 when a crossing point of $\overline{\mathbf{PP}}_2^3$ and $\overline{\mathbf{PD}}$ is approached along $\mathbf{PP}_2^4$; note that both G and $\overline{E}$ have a single global excursion that does not come close to Γ_1.

The structurally stable return surface $H = W^u(\Gamma_4) \cap W^s(\Gamma_2)$ is a narrow Möbius strip that accumulates on the single codimension-zero connection $W^u(\Gamma_3) \cap W^s(\Gamma_2)$. This particular surface is not shown in panels (a1) and (a2) of Fig. 25, but its counterpart $\widehat{H}$ at the level of a diffeomorphism is included in the sketch in panel (b) that shows a neighbourhood of the period-four orbit $\boldsymbol{\gamma}_4 = (\gamma_4^1, \gamma_4^2, \gamma_4^3, \gamma_4^4)$ representing Γ_4. The outer curve $\widehat{I}$ is the transverse intersection of the two-dimensional manifolds $W^u(\boldsymbol{\gamma}_4)$ and $W^s(\gamma_1)$; note that the overall global picture including γ_1 is still as shown in Fig. 21(b). As $\mathbf{PP}_2^4$ approaches one of the crossing points of $\overline{\mathbf{PP}}_2^3$ with the curve $\overline{\mathbf{PD}}$, the intersection curves $\widehat{H}$ and $\widehat{I}$ converge to the curves $\widehat{F} = W^u(\boldsymbol{\gamma}_3) \cap W^s(\gamma_2)$ and $\widehat{D} = W^u(\boldsymbol{\gamma}_3) \cap W^s(\gamma_1)$, respectively; see Fig. 21(b). Also shown in Fig. 25(b) is the codimension-one connecting orbit $(g_k)_{k\in\mathbb{Z}}$ corresponding to G, which similarly converges to the connecting orbit $(\bar{e}_k)$ from γ_2 to γ_3; see again Fig. 21(b).

5.2 Accumulation of the heterodimensional cycle $\mathbf{PP}_2^4$ onto Γ_e

The heterodimensional cycle $\mathbf{PP}_2^4$ can also be continued in the direction of increasing s from the lower crossing point of $\overline{\mathbf{PP}}_2^3$ in Fig. 24(b). The resulting curve $\mathbf{PP}_2^4$ is shown in Fig. 26(a), and it has many more loops that each have an additional tangency point with $\overline{\mathbf{PD}}$; moreover, this new segment of $\mathbf{PP}_2^4$ appears to accumulate on other curves, and we now explain why.

Figure 26(b1) shows the scaled c_t-time trace of a computed orbit segment of G from Fig. 25 at the parameter point $(\Delta J, s) \approx (0.674, 9.3)$ on the first loop of the curve $\mathbf{PP}_2^4$. It features a single large 'peak' throughout its excursion away from a neighbourhood of Γ_2 and Γ_4. Figure 26(b2) shows the c_t-time trace of G at the point $(\Delta J, s) \approx (0.702, 9.3)$, which lies on the second loop of $\mathbf{PP}_2^4$; it features two large peaks. The c_t-time trace of G in panel (b3) has six large peaks, and it is for G at the point $(\Delta J, s) \approx (0.926, 9.3)$ on the sixth loop of $\mathbf{PP}_2^4$. The large peaks are, in fact, excursions to an additional periodic orbit, which we denote Γ_e, because it is 'external' in the sense that it is not associated with bifurcations of any periodic orbit we considered so far. Figure 26(c) shows Γ_e together with the connection G from Γ_2 to Γ_4 that corresponds to the c_t time trace shown in panel (b3).

The external periodic orbit Γ_e was found from the data of G by imposing periodic boundary conditions on a segment of approximately one period; it has index one at $(J, s) \approx (2.926, 9.35)$ with Floquet multipliers

$$\lambda_e^{ss} \approx -5.955 \times 10^{-3}, \quad \lambda_e^{s} \approx 5.525 \times 10^{-1}, \quad \lambda_e^{u} \approx -1.499 \times 10^{8}.$$

Hence, the connection G approaches Γ_e near its three-dimensional stable manifold $W^s(\Gamma_e)$, makes a number of loops around it, and then leaves along the two-dimensional unstable manifold $W^u(\Gamma_e)$. Completing a loop of the curve $\mathbf{PP}_2^4$ in Fig. 26(a) corresponds to G making another loop near Γ_e. In other words, G winds more and more around Γ_e along $\mathbf{PP}_2^4$. In the limit of infinitely many windings around Γ_e, the connection G becomes two separate connections: the codimension-one connection G_e from Γ_e to Γ_4 in the quasi-transverse intersection $W^u(\Gamma_e) \cap W^s(\Gamma_4)$, and the

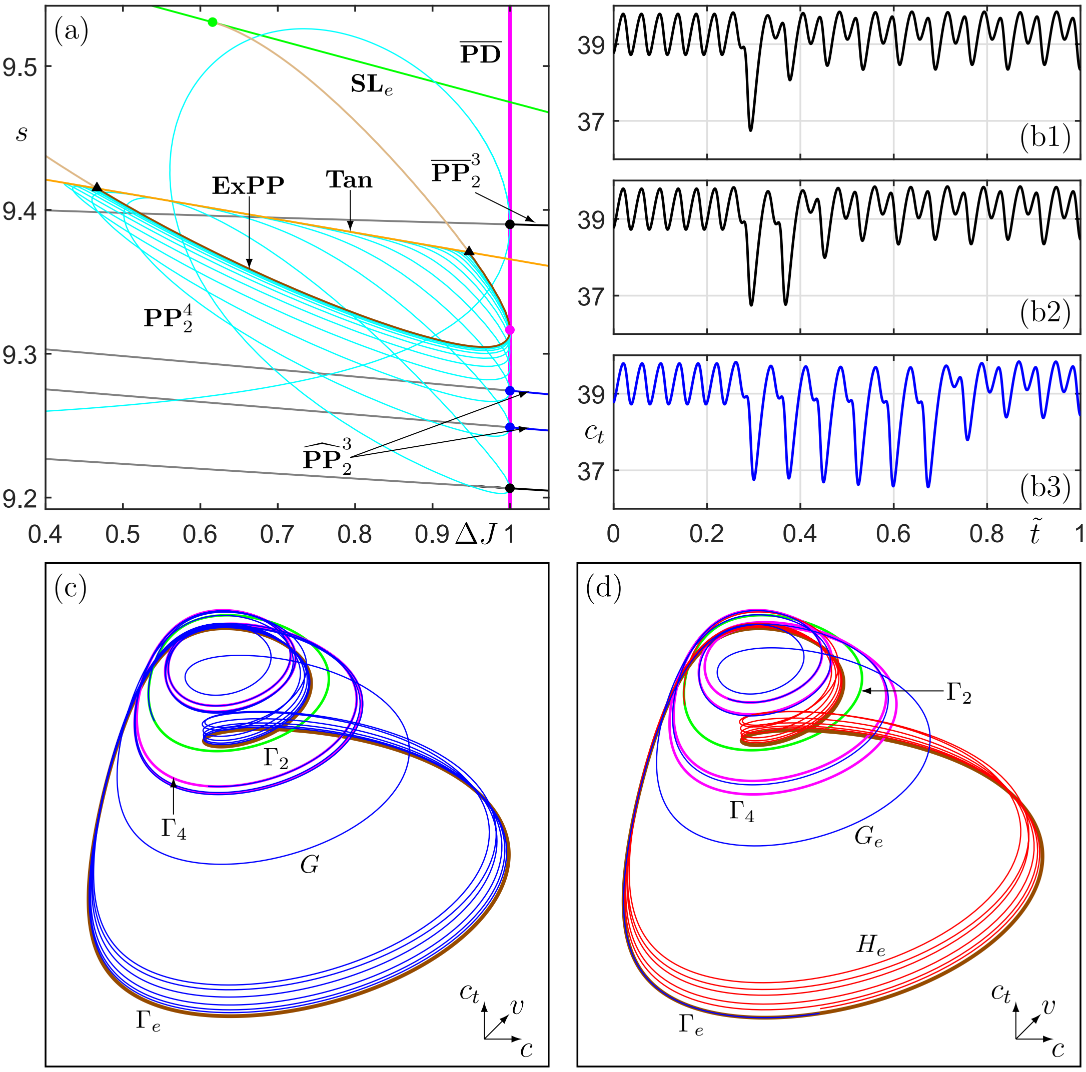

Figure 26: Accumulation of the curve $\mathbf{PP}_2^4$ and the corresponding heterodimensional cycle. Panel (a) shows the rescaled bifurcation diagram from Fig. 24(b) with many more loops of $\mathbf{PP}_2^4$ (cyan), and additionally: the curve $\mathbf{SL}_e$ (green) of saddle-node bifurcations of Γ_e; the locus **Tan** (orange), along which H_e is a codimension-one tangential connection; and the locus **ExPP** (brown curve) of the extended PtoP cycle involving Γ_e; and the locus $\widehat{\mathbf{PP}}_2^3$ of a further heterodimensional cycle between Γ_2 and Γ_3. Panels (b1)–(b3) show the scaled c_t-time traces of the computed connecting orbit G, specifically, on the first loop of $\mathbf{PP}_2^4$ at $(\Delta J, s) \approx (0.674, 9.3)$ as in Fig. 25, the second loop at $(\Delta J, s) \approx (0.702, 9.3)$, and the sixth loop at $(\Delta J, s) \approx (0.926, 9.3)$, respectively; panel (c) shows the connecting orbit G on the sixth loop with Γ_e. Panel (d) shows the codimension-one connection $G_e = W^{\rm u}(\Gamma_e) \cap W^{\rm s}(\Gamma_4)$ (blue) and the structurally stable connecting orbit $H_e = W^{\rm u}(\Gamma_2) \cap W^{\rm s}(\Gamma_e)$ (red) at $(J, s) = (2.926, 9.35)$; with the surface $H = W^{\rm u}(\Gamma_4) \cap W^{\rm s}(\Gamma_2)$ (not shown) they form the extended PtoP cycle **ExPP** between Γ_2, Γ_4 and Γ_e.

structurally stable connection H_e from Γ_2 to Γ_e in the transverse intersection $W^{\rm u}(\Gamma_2) \cap W^{\rm s}(\Gamma_e)$. These two new connections can be found with a suitable BVP setup initialised with the respective computed segments of G; they are shown in Fig. 26(d) at $(J, s) \approx (2.926, 9.35)$. Together with the surface $H = W^{\rm u}(\Gamma_4) \cap W^{\rm s}(\Gamma_2)$ (not shown), they form a PtoP cycle from Γ_2 to Γ_e to Γ_4 and back to Γ_2, which is heterodimensional since Γ_2 and Γ_e have index one and Γ_4 has index two. We refer to this PtoP cycle as the 'extended' heterodimensional cycle **ExPP**, and it exists along the curve segment shown in Fig. 26(a). More specifically, it is the part of the locus of the codimension-one connection G_e that lies in the region where the structurally stable connecting orbit H_e also exists. The latter disappears at a tangency between $W^{\mathrm{u}}(\Gamma_2)$ and $W^{\mathrm{s}}(\Gamma_e)$; we computed this tangency and continued its locus **Tan**, which is also shown in Fig. 26(a). The connection H_e does not exist in the region above **Tan** since $W^{\mathrm{u}}(\Gamma_2)$ and $W^{\mathrm{s}}(\Gamma_e)$ are disjoint there. However, the curve along which G_e exists does extend above **Tan**, and it has an endpoint on the locus $\mathbf{SL}_e$ at which Γ_e disappears in a saddle-node bifurcation.

Observe in Fig. 26(a) that the curve $\mathbf{PP}_2^4$ accumulates on the curve segment **ExPP**, and this accumulation is explained by the windings of G around the external periodic orbit Γ_e. This phenomenon is akin to the windings of a homoclinic orbit to an equilibrium around an 'external' periodic orbit found and analysed in [21]: the limit of this process is an Equilibrium-to-Periodic (EtoP) cycle, and the associated curve of homoclinic orbits was also found to accumulate on a curve segment of such EtoP cycles, bounded by tangency loci of the structurally stable EtoP connection. Here, we find a more complicated instance of the same general phenomenon: a connecting orbit accumulating on an external saddle object and subsequently forming a complicated global heteroclinic structure. In our case, a codimension-one PtoP connection accumulates on the saddle periodic orbit Γ_e to form the extended PtoP cycle **ExPP** shown in Fig. 26(d). Notably, the curve **ExPP** in Fig. 26(a) appears to be tangent to $\overline{\mathbf{PD}}$ at the accumulation point of the tangency points of $\mathbf{PP}_2^4$ with $\overline{\mathbf{PD}}$.

The tangency points of $\mathbf{PP}_2^4$ come in pairs that each correspond to a 'full loop' of $\mathbf{PP}_2^4$, and each such pair is also a pair of crossing points of a unique locus of heterodimensional cycles between Γ_2 and Γ_3. One such curve, labeled $\widehat{\mathbf{PP}}_2^3$, is shown in panel (a); it is actually a single smooth curve that ends on $\overline{\mathbf{PD}}$ at two tangency points of $\mathbf{PP}_2^4$. It can be extended as a locus of strong heteroclinic cycles to the left of $\overline{\mathbf{PD}}$. Therefore, we conclude that there exists an infinite sequence of further curves of heterodimensional cycles between Γ_2 and Γ_3; each such curve has a codimension-one connection with additional loops around Γ_e. In particular, note that the global excursion of the heterodimensional cycle $\overline{\mathbf{PP}}_2^3$ from Fig. 21 should perhaps be identified as a first loop near Γ_e rather than Γ_1.

5.3 Overall picture of cascading heterodimensional cycles

Our results in the last section show that heterodimensional cycles involving periodic orbits arising from successive period-doubling bifurcations may interact with an external periodic orbit to generate infinite families of additional and more complicated heterodimensional cycles. By way of a summary, Fig. 27 provides a conceptual overall picture in the form of a sequence of directed graphs. Each node is a periodic orbit of a specified index, and the directed edges represent connections from one periodic orbit to another. We indicate the nature of the connections symbolically in the style introduced in [17] to represent different types of EtoP or PtoP connections:

- $\longrightarrow$ represents a codimension-one connection;
- $\longrightarrow$ represents a single codimension-zero connection; and
- $\Longrightarrow$ represents a structurally stable surface of codimension-zero connections.

This representation is similar in spirit to the graph presented in [3] to illustrate how EtoP and PtoP connections in a four-dimensional Hamiltonian system can be combined to generate new and more complicated homoclinic orbits. Heterodimensional cycles between two specific periodic orbits are closed loops between two nodes of different indices; they are heterodimensional if the cycles involve a codimension-one connection and a structurally stable return surface.

Figure 27(a) depicts the situation in between the period-doubling loci **PD** and $\overline{\mathbf{PD}}$ with Γ_2, Γ_3 and an external periodic orbit Γ_e; note again that Γ_2 and Γ_e have index one, while Γ_3 has index

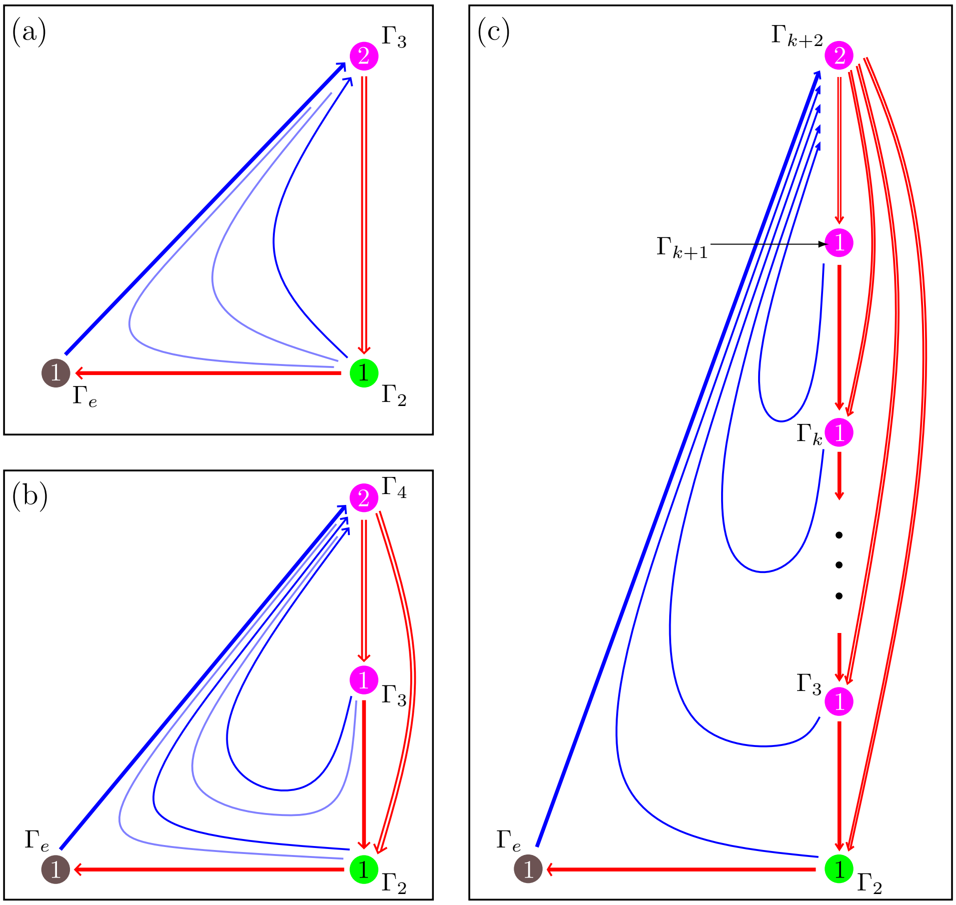

Figure 27: Directed graphs that represent how heterodimensional cycles from Γ_2 to periodic orbits Γ_k arising from successive period-doublings interact with an external periodic orbit Γ_e. Each node represents a periodic orbit, and the number is its index; blue edges represent quasi-transverse connecting orbits, red edges structurally stable isolated connecting orbits, and red double edges surfaces of structurally stable connecting orbits. Panels (a) and (b) illustrates heterodimensional cycles before and after the period-doubling bifurcation $\overline{\mathbf{PD}}$ of Γ_3, respectively; and panel (c) represents the situation after the kth period-doubling bifurcation in the cascade.

two. The outer closed path

$$\Gamma_2 \longrightarrow \Gamma_e \longrightarrow \Gamma_3 \Longrightarrow \Gamma_2$$

is the extended PtoP cycle. The inner closed path $\Gamma_2 \longrightarrow \Gamma_3 \Longrightarrow \Gamma_2$ is the basic heterodimensional cycle between Γ_2 and Γ_3, which is $\overline{\mathbf{PP}}_2^3$ from Fig. 21. The lighter edges that bypass Γ_e represent additional codimension-one connections that are part of heterodimensional cycles between Γ_2 and Γ_3 with an increasing number of loops around Γ_e. These additional heterodimensional cycles form the infinite sequence discussed in Sec. 5.2, and the heterodimensional cycle $\widehat{\mathbf{PP}}_2^4$ is a specific example.

The situation just after the period-doubling bifurcation $\overline{\mathbf{PD}}$, when the new period-doubled orbit Γ_4 exists, is represented by the graph in Fig. 27(b). Here, the outer closed path

$$\Gamma_2 \longrightarrow \Gamma_e \longrightarrow \Gamma_4 \Longrightarrow \Gamma_2$$

is the extended heterodimensional cycle **ExPP** from Fig. 26(d). More precisely, its connections H_e and G_e are $\Gamma_2 \longrightarrow \Gamma_e$ and $\Gamma_e \longrightarrow \Gamma_4$, respectively, and the surface $H = W^{\mathrm{u}}(\Gamma_4) \cap W^{\mathrm{s}}(\Gamma_2)$ (not shown) is $\Gamma_4 \Longrightarrow \Gamma_2$. The closed path $\Gamma_2 \longrightarrow \Gamma_4 \Longrightarrow \Gamma_2$ is the basic heterodimensional cycle $\mathbf{PP}_2^4$

between Γ_2 and Γ_4 from Fig. 25. The lighter edges bypassing Γ_e again represent the codimension-one connections of additional heterodimensional cycles along the curve $\mathbf{PP}_2^4$, each of which lies on a full loop of $\mathbf{PP}_2^4$ as illustrated in Fig. 26.

The graph in Fig. 27(b) also shows the closed path $\Gamma_3 \longrightarrow \Gamma_4 \Longrightarrow \Gamma_3$, which represents a basic heterodimensional cycle between Γ_3 and Γ_4. Our results from Sec. 4.4 for the heterodimensional cycle $\mathbf{PP}_2^3$ suggest that this basic heterodimensional cycle arises from a strong homoclinic orbit to Γ_3 that exists near $\overline{\mathbf{PP}}_2^3$. Such a strong homoclinic orbit features a single global excursion near Γ_e; however, the fact that there exist additional heterodimensional cycles such as $\widehat{\mathbf{PP}}_2^3$ with more loops around Γ_e strongly suggests the existence of corresponding strong homoclinic orbits. This situation is further complicated by the fact that each such heterodimensional cycle gives rise to a strong homoclinic orbit with an arbitrary number of loops around Γ_2. In turn, these homoclinic orbits winding around both Γ_2 and Γ_e give rise to additional codimension-one connections from Γ_3 to Γ_4 that also wind around both Γ_2 and Γ_e. Such codimension-one connections, represented by the lighter edge bypassing Γ_2 and Γ_e in Fig. 27(b), are part of the corresponding heterodimensional cycles between Γ_3 and Γ_4. Their limit is the extended heterodimensional cycle represented by

$$\Gamma_3 \longrightarrow \Gamma_2 \longrightarrow \Gamma_e \longrightarrow \Gamma_4 \Longrightarrow \Gamma_3.$$

We expect that all of these additional (extended) heterodimensional cycles exist in the (J, s)-plane of system (1). However, computing them and their loci is beyond the scope of this paper. Instead, this is illustrated conceptually in Fig. 27(c) by the graph of connections after the k-th period-doubling bifurcation. We believe that it captures the essence of a 'cascade' of heterodimensional cycles due to period doubling. More specifically, our overall conjecture is that all the connections and intermediate families of (extended) heterodimensional cycles exist for any k; indeed, this is supported by the extensive computations of the global objects already presented. Note here that the 'top' periodic orbit Γ_{k+2} is the only periodic orbit of index two in this period-doubling tower; hence, it must be part of any possible heterodimensional cycle. We note also that the external periodic orbit Γ_e is not necessarily unique, and interaction of a heterodimensional cycle with other external periodic orbits leads to further accumulations of heterodimensional cycles. Previous work in [32] showed that infinitely many periodic orbits exist near the primary heterodimensional cycle **PtoP** that are each a candidate for the role of Γ_e. In turn, every additional heterodimensional cycle is expected to generate infinitely many more nearby families of periodic orbits. Hence, we conjecture that the 'true picture' of the complexity in phase space involves infinitely many external periodic orbits; this overall structure can be imagined in a three-dimensional representation as infinitely many copies of the directed graph from Fig. 27(c) surrounding the 'spine' formed by the period-doubling orbits Γ_2 to Γ_{k+2}. At the limit of the period-doubling cascade, one finds a parameter region with extremely rich recurrent and nonhyperbolic dynamics. In particular, the periodic orbit Γ_2 is now part of a hyperbolic set that may well play the role of a blender.

6 Conclusions and outlook

We showed how the primary heterodimensional cycle of the Atri model (1) changes geometrically along its locus **PtoP** in the (J, s)-plane, which ends on the curve **PD** of period-doubling bifurcation of one constituent periodic orbit. Past **PD**, the curve **PtoP** can be continued as a strong heteroclinic cycle. From the endpoint of **PtoP** on **PD** also emerges a heterodimensional cycle involving the period-two periodic orbit. Moreover, we showed that a crossing of **PD** by a locus of strong homoclinic orbits is the starting point of a new curve of 'period-doubled heterodimensional cycles', namely, those between the periodic orbit of the homoclinic orbit and its own period-doubled counterpart. In fact, we found evidence of infinitely many families of such period-doubled heterodimensional cycles. Their loci in the (J, s)-plane end at the next period-doubling curve of a whole cascade, and the process keeps repeating in this way. We represented the overall phenomenon of cascading heterodimensional cycles by a sequence of directed graphs, which encodes how different types of heterodimensional cycles arise due to repeated period doubling. This includes extended heterodimensional cycles that connect more than two periodic orbits.

These results have been obtained by a careful investigation of system (1) performed with advanced numerical tools by first formulating desired heteroclinic connections as orbit segments satisfying a suitably defined boundary value problem. This approach allowed us to compute a heteroclinic orbit as the intersection set of the relevant stable and unstable manifolds and also their loci of existence by further continuation in two system parameters. In this way, we investigated how heterodimensional cycles change geometrically and bifurcate to generate a menagerie of new global structures. These include new types of heterodimensional cycles, which we illustrated in the phase space of system (1), as well as at the level of a three-dimensional diffeomorphism with supporting numerical evidence of the geometric properties of global manifolds in suitable Poincaré sections.

While our investigation concerned the specific example of the Atri model (1), the numerical evidence we collected, in combination with arguments from the theory of dynamical systems, shows that we are dealing with generic phenomena. Hence, our work constitutes a contribution to the emerging bifurcation theory of heterodimensional cycles: the transitions and bifurcations we found must be expected to occur in vector fields of dimension four and, hence, equivalently in diffeomorphisms of dimension three.

We propose the following directions for further research. Firstly, in ongoing work, we are investigating other bifurcations of a heterodimensional cycle or a related global object in the Atri model (1). For example, a locus of heterodimensional cycles can also end on a curve of saddle-node bifurcations of a constituent periodic orbit. Moreover, initial investigations show that such saddle-node curves may feature infinitely many branches, along which different pairs of periodic orbits are created; these branches are separated by cusp bifurcations and accumulate in the (J, s)-plane in an intriguing way. These results will be discussed in a forthcoming publication. Secondly, it will be interesting to find heterodimensional cycles in other vector-field models and also in diffeomorphisms; a number of candidate systems are presently under investigation. Finally, the bifurcation diagrams we presented are a contribution to the emerging bifurcation theory of heterodimensional cycles. It will be interesting to study the different bifurcations and new types of heterodimensional cycles we found here from a theoretical perspective. The codimension-two bifurcations of a heterodimensional cycle and of a strong homoclinic orbit at period doubling are specific examples. It will be a considerable challenge to determine the respective unfoldings and prove their completeness.

Acknowledgements

We thank Andy Hammerlindl and Katsutoshi Shinohara for helpful discussions. This research was supported by Royal Society Te Apārangi Marsden Fund grants #16-UOA-286 and #22-UOA-204.

Appendix A. Finding connecting orbits numerically

We provide a brief and high-level overview of how connecting orbits between saddle periodic orbits of a vector field can be found and continued numerically. First of all, standard continuation packages, such as AUTO [13, 14], COCO [8, 9] and MatCont [10, 11], readily compute equilibria, periodic orbits and their bifurcations, and continue them in the appropriate number of system parameters. Hence, the periodic orbits involved in the connection of interest are taken as known; more specifically, they are given as solutions of a boundary value problem (BVP) with periodic boundary conditions.

Lin's method Relevant parts of stable and unstable manifolds, as well as connecting orbits of different kinds, can also be formulated and then found numerically as solutions of suitably defined BVPs; this general approach has been shown to be efficient and reliable and is well established by now [15, 22]. A particularly useful numerical tool for finding connecting orbits is Lin's method [21, 32]: in the present context, two orbit segments, one on an unstable manifold and the other on a stable manifold, are required to end in a user-specified section, where they define the so-called Lin gap. Closing the Lin gap by an appropriate continuation run then gives the desired connecting orbit. In practice, we require the respective opposite endpoints to lie close to the corresponding periodic orbits on a stable or unstable Floquet vector; this requirement is known as projection boundary conditions [4]. Lin's method was introduced and implemented in [21] as a reliable numerical method for finding connecting orbits involving periodic orbits; different Equilibrium-to-Periodic (EtoP) connections and a structually stable PtoP connection were computed as examples, but no example of a Periodic-to-Periodic (PtoP) connection of codimension one was known at the time. The first such example was found and computed with Lin's method in the four-dimensional Atri model (1) in [32]. The precise formulation of the overall multi-segment BVP for the two periodic orbits, their stable and unstable Floquet bundles, and the orbit segments required for Lin's method can be found in [32]; see also [21] for a detailed and general explanation of Lin's method. Once a connecting orbit of interest has been found in this way, the two orbit segments can be continued together in system parameters while keeping the Lin gap closed; alternatively, they can be concatenated to form a single orbit segment that represents the connecting orbit as a solution of a simplified BVP with the same projection boundary conditions.

We use the methodology from [32] to implement and solve the appropriate BVPs within the package AUTO [13, 14] by making use of its collocation-based BVP solver and pseudo-arclength continuation. The examples of the primary heterodimensional cycle in regions I–IV, the associated curve **PtoP**, as well as the strong heteroclinic cycle along the curve $\mathbf{PtoP}^{\mathrm{ss}}$ were computed in this way. More specifically, Lin's method is implemented separately to find the codimension-one connection and the connecting orbits forming the structurally stable return surface.

Finding additional global objects Connecting orbits can be continued in system parameters as a means to detect new types of global objects. We used this strategy in a number of ways. Firstly, we perturbed away from the codimension-one strong heteroclinic cycle $\mathbf{PtoP}^{\mathrm{ss}}$ in region V to obtain a structurally stable heteroclinic cycle between Γ_1 and Γ_2. When continued in a single system parameter, the relevant connection appears to accumulate on the period-doubled periodic orbit Γ_3. This observation indicates that, at some limiting parameter value, the same connection becomes a codimension-one connection involving Γ_3, which inspired our method to compute the heterodimensional cycle $\mathbf{PP}_1^3$ between Γ_1 and Γ_3 shown in Sec. 4.3. We first redefined the BVP for the primary heterodimensional cycle in region IV in terms of double the period of Γ_2. Since this period-doubled version of Γ_2 is identical to Γ_3 at the period-doubling bifurcation **PD**, the aforementioned observation infers that a new family of heterodimensional cycles between Γ_1 and Γ_3 'branches off' from the curve **PtoP** at its codimension-two endpoint **PDP** on the curve **PD**. Specifically, one continues the codimension-one connection A from Γ_1 to Γ_2 as a solution of this 'period-doubled BVP' in the system parameters J and s towards **PD**; the software AUTO detects a branching point of this continuation at **PDP**, and we then use the branch-switching functionality of AUTO to switch to the curve $\mathbf{PP}_1^3$ and compute its associated period-doubled cycle. Similarly, we found the extended heterodimensional cycle **ExPP** in Sec. 5.2 by continuing the codimension-one connection G; more specifically, the new periodic orbit Γ_e was first found by using a suitable segment of G as the initial data. Subsequently, the trajectory data of G was separated into two segments to find the two new connections to and from Γ_e. Another example is the continuation of the structurally stable connecting orbit H_e; it disappears at a codimension-one tangency between $W^{\mathrm{u}}(\Gamma_2)$ and $W^{\mathrm{s}}(\Gamma_e)$, yielding the corresponding curve **Tan** in Sec. 5.2.

Computed orbit segments representing a given PtoP cycle can also be used to find nearby structurally stable global objects, in particular, homoclinic orbits to one of the two constituent periodic orbits. These can then be continued in a single system parameter until a global codimension-one bifurcation is detected; specifically, we found the strong homoclinic orbit **SHC** in Sec. 3.2 in this way. The reverse is also possible: the data of a homoclinic orbit that comes close to another saddle periodic orbit can be separated into two segments, which are then used as initial guesses for individual BVP formulations to find the corresponding new global connections.

Local intersection sets of global objects To support the sketches at the level of a diffeomorphism, we compute relevant intersection sets with local three-dimensional Poincaré sections. Each such section is 'pinned' at a selected point γ of a periodic orbit Γ and defined as being normal to the adjoint vector (left eigenvector) associated with the trivial Floquet multiplier $\mu = 1$. This choice is very convenient because it ensures that the section is spanned by the stable and unstable (generalised) Floquet vectors at γ. The local intersection sets of connecting orbits are then computed by detecting when points of the respective (family of) orbit segments lie in the chosen section. For codimension-one connections, local segments of the relevant one-dimensional invariant manifolds can be computed by requiring one endpoint to remain in the section; we refer to [19] for more details.

References

[1] Abraham R, Smale S. Nongenericity of Ω-stability. In: Chern S-S, Smale S, editors. *Global Analysis (Proc. Sympos. Pure Math., Berkeley, Calif., 1968)*, volume XIV, Providence, RI: American Mathematical Society; 1970, p. 5–8. (Also published in *The Collected Papers of Stephen Smale*, volume 2, Singapore: World Scientific; 2000, p. 735–738.)

[2] Atri A, Amundson J, Clapham D, Sneyd J. A single-pool model for intracellular calcium oscillations and waves in the Xenopus laevis oocyte. *Biophysical Journal* **65**(4): 1727–1739, 1993. https://doi.org/10.1016/S0006-3495(93)81191-3.

[3] Bandara R, Giraldo A, Broderick NGR, Krauskopf B. Generalized and multi-oscillation solitons in the nonlinear Schrödinger equation with quartic dispersion. *Chaos* **33**(7): 073154, 2023. https://doi.org/10.1063/5.0152562.

[4] Beyn W-J . The numerical computation of connecting orbits in dynamical systems. *IMA Journal of Numerical Analysis* **10**(3): 379–405, 1990. https://doi.org/10.1093/imanum/10.3.379.

[5] C Bonatti and LJ Díaz. Robust heterodimensional cycles and C^1-generic dynamics. *Journal of the Institute of Mathematics of Jussieu* **7**(3): 469–525, 2008. https://doi.org/10.1017/S1474748008000030.

[6] Christian Bonatti, Lorenzo J. Díaz, and S. Kiriki. Stabilization of heterodimensional cycles. *Nonlinearity* **25**(4): 931–960, 2012. https://doi.org/10.1088/0951-7715/25/4/931.

[7] Champneys AR, Kirk V, Knobloch E, Oldeman BE, Sneyd J. When Shil'nikov meets Hopf in excitable systems. *SIAM Journal on Applied Dynamical Systems* **6**(4): 663–693, 2007. https://doi.org/10.1137/070682654.

[8] Dankowicz H, Schilder F. Recipes for continuation. Philadelphia: Society for Industrial and Applied Mathematics; 2013.

[9] Dankowicz H, Schilder F. Continuation Core and Toolboxes (COCO) Toolboxes for parameter continuation and bifurcation analysis. available from `https://sourceforge.net/projects/cocotools/`, 2023

[10] Dhooge A, Govaerts W, Kuznetsov YuA. MatCont: A MATLAB package for numerical bifurcation analysis of ODEs. *ACM Transactions on Mathematical Software* **29**(2): 141–164, 2003. Available from `http://sourceforge.net/projects/matcont`

[11] Dhooge A, Govaerts W, Kuznetsov YuA, Meijer HGE, Sautois B. New features of the software MatCont for bifurcation analysis of dynamical systems. *Mathematical and Computer Modelling of Dynamical Systems* **14**(2): 147–175, 2008. `https://doi.org/10.1080/13873950701742754`.

[12] Díaz LJ, Pérez S. Nontransverse heterodimensional cycles: Stabilisation and robust tangencies. *Transactions of the American Mathematical Society* **376**(2): 891–944, 2023. `https://doi.org/10.1090/tran/8694`.

[13] Doedel EJ. AUTO: A program for the automatic bifurcation analysis of autonomous systems. *Congressus Numerantium* **30**: 265–284, 1981.

[14] Doedel EJ, Oldeman BE. AUTO-07P: Continuation and Bifurcation Software for Ordinary Differential Equations. With major contributions from Champneys AR, Dercole F, Fairgrieve TF, Kuznetsov YuA, Paffenroth RC, Sandstede B, Wang XJ, Zhang CH, 2007. Available from `http://cmvl.cs.concordia.ca/auto`.

[15] Doedel EJ. Lecture notes on numerical analysis of nonlinear equations. In Krauskopf B, Osinga HM, Galán-Vioque J, editors. *Numerical Continuation Methods for Dynamical Systems: Path following and boundary value problems*, Dordrecht:Springer-Verlag; 2007, p. 1–50.

[16] Giraldo A, Krauskopf B, Osinga HM. Saddle invariant objects and their global manifolds in a neighborhood of a homoclinic flip bifurcation of case B. *SIAM Journal on Applied Dynamical Systems* **16**(1): 640 – 686, 2017. `https://doi.org/10.1137/16M1097419`.

[17] Giraldo A, Broderick NGR, Krauskopf B. Chaotic switching in driven-dissipative Bose-Hubbard dimers: When a flip bifurcation meets a T-point in $\mathbb{R}^4$. *Discrete and Continuous Dynamical Systems – Series B* **27**(7): 4023 – 4075, 2022. `https://doi.org/10.3934/dcdsb.2021217`.

[18] Guckenheimer J, Holmes P. *Nonlinear Oscillations, Dynamical Systems, and Bifurcations of Vector Fields*. Applied Mathematical Sciences, volume 42. New York: Springer-Verlag; 2013.

[19] Hammerlindl A, Krauskopf B, Mason G, Osinga HM. Determining the global manifold structure of a continuous-time heterodimensional cycle. *Journal of Computational Dynamics* **9**(3): 393–419, 2022. `http://dx.doi.org/10.3934/jcd.2022008`.

[20] Hirsch MW, Smale S. *Differential Equations, Dynamical Systems, and Linear Algebra*. Pure and Applied Mathematics, volume 60. New York: Academic Press; 1974.

[21] Krauskopf B, Rieß T. A Lin's method approach to finding and continuing heteroclinic connections involving periodic orbits. *Nonlinearity* **21**(8): 1655–1690, 2008. `https://doi.org/10.1088/0951-7715/21/8/001`.

[22] Krauskopf B, Osinga HM, Galán-Vioque J. *Numerical Continuation Methods for Dynamical Systems: Path following and boundary value problems*. Understanding Complex Systems. Dordrecht: Springer-Verlag; 2007.

[23] Kuznetsov YuA. *Elements of Applied Bifurcation Theory*. Applied Mathematical Sciences, volume 112. 3rd ed. New York: Springer-Verlag; 2004.

[24] Li D, Turaev D. Persistence of heterodimensional cycles. *Inventiones mathematicae* **236**(3): 1413–1504, 2024. https://doi.org/10.1007/s00222-024-01255-3.

[25] Moreira CG. There are no C^1-stable intersections of regular Cantor sets. *Acta Mathematica* **206**(2): 311–323, 2011. https://doi.org/10.1007/s11511-011-0064-0.

[26] Newhouse SE. Diffeomorphisms with infinitely many sinks. *Topology* **13**(1): 9–18, 1974. https://doi.org/10.1016/0040-9383(74)90034-2.

[27] Palis J. On Morse-Smale dynamical systems. *Topology* **8**(4): 385–404, 1969. https://doi.org/10.1016/0040-9383(69)90024-X.

[28] Palis J, Smale S. Structural stability theorems. In: Chern S-S, Smale S, editors. *Global Analysis (Proc. Sympos. Pure Math., Berkeley, Calif., 1968)*, volume XIV, Providence, RI: American Mathematical Society; 1970, p. 223–231. (Also published in *The Collected Papers of Stephen Smale*, volume 2, Singapore: World Scientific; 2000, p. 739–747.)

[29] Robbin JW. A structural stability theorem. *Annals of Mathematics* **94**(3): 447–493, 1971. https://doi.org/10.2307/1970766.

[30] Smale S. Differentiable dynamical systems. *Bulletin of the American Mathematical Society* 73(6): 747–817, 1967. https://doi.org/10.1090/S0002-9904-1967-11798-1.

[31] Tsai J-C, Zhang W, Kirk V, Sneyd J. Traveling waves in a simplified model of Calcium dynamics. *SIAM Journal on Applied Dynamical Systems* **11**(4): 1149–1199, 2012. https://doi.org/10.1137/120867949.

[32] Zhang W, Krauskopf B, Kirk V. How to find a codimension-one heteroclinic cycle between two periodic orbits. *Discrete and Continuous Dynamical Systems – Series A* **32**(8): 2825–2851, 2012. https://doi.org/10.3934/dcds.2012.32.2825.

[33] Zhang W-B. *Discrete Dynamical Systems, Bifurcations and Chaos in Economics*. Mathematics in Science and Engineering, volume 204. Amsterdam, North Holland: Elsevier; 2006.